9-11-2018

Engineering Metal-Ligand Interface for Selective Electrochemical Carbon Dioxide Reduction

Yuxin Fang
Louisiana State University and Agricultural and Mechanical College, yfang16@lsu.edu

ENGINEERING METAL-LIGAND INTERFACE FOR SELECTIVE ELECTROCHEMICAL CO_2 REDUCTION

A Dissertation

Submitted to the Graduate Faculty of the
Louisiana State University
and Agriculture and Mechanical College
in partial fulfillment of the
requirements for the degree of
Doctor of Philosophy

in

The Gordon A. and Mary Cain Department of Chemical Engineering

by
Yuxin Fang
B.S., University of Missouri
December 2018

Be brave like a knight in shining armor

Honor, Courtesy, Devotion, Bravery

Always

ACKNOWLEDGEMENT

First and foremost, I want to express my sincere gratitude to my advisor, Professor John C. Flake for successful completion of my dissertation. His patience, encouragement, trust, and guidance with immense knowledge were the most important sources of support for me to complete my graduate study. He has taught me, consciously whether or not, how to be a cool scientist and engineer. I cannot imagine having a better advisor and mentor. I am honored to be his student.

Besides my advisor, I would like to thank the rest of my thesis committee: Professor Christopher G. Arges, Professor James J. Spivey, Professor Ye Xu, and Professor David M. Koppelman, for their insightful comments and encouragement, but also for the challenging question which inspire me for new ideas in my future research.

I would like to send my heartfelt appreciation to Prof. Xu for all the insightful discussions in completing our joint research, Prof. Robin L. McClarley for the best lessons in electrochemistry, Dr. Thomas Weldeghiorghis for his selfless sharing of knowledge in NMR, Dr. Dongmei Cao for her guidance in material characterization at the Shared Instrument Facility, Dr. Evan Andrews for being the only lab colleague who helped me in the starting stage of my research, and Ben Peterson for daily scientific discussions and contribution to the English part of my dissertation.

I also want to thank all the people who collaborated and helped me in my research and graduate school life, including Dr. Zhenyu Zhang, Dr. Zhenyu Diao and

Dr. Hangwen Guo from Department of Physics, and Dr. Zi Wang, Swarom Kanitkar, Joe M. Bell, Nick S. Lombardo and Darla T. Dao from Department of Chemical Engineering.

Last but not the least, I would like to thank my parents for their love and trust; my friends: Jielin Yu, Chuanlin Zhao and Yao Wu. Special thank goes to Yi Feng, for her ever-presence since we met at 12.

TABLE OF CONTENTS

LIST OF TABLES

LIST OF FIGURES

LIST OF ABBREVIATIONS

Abbreviation	Meaning
2-MPA	2-Mercaptanproponic Acid
2-PET	2-Phenylethanethiol
4-PEM	4-pyridiniumethyl Mercaptan
Ace	3-acetamidopropyl) trimethoxysilane
AFM	Atomic Force Microscopy
Ami	3-aminopropyltrimethoxysilane
Asym str	Asymmetric stretching
ATR	Attenuated Total Reflection
CO2RR	CO_2 Reduction Reaction
CV	Cyclic Voltammetry
CYS	Cysteamine
DFT	Density Function Theory
DRIFT	Diffuse Reflectance Infrared Fourier Transform
FE	Faradayic Efficiency
FID	Flame Ignition Detector
FT-IR	Fourier Transform Infrared Spectroscopy
HER	Hydrogen Evolution Reaction
MCT	Mercury Cadmium Telluride
NMR	Nuclear Magnetic Resonance

NP	Nanoparticle
PCET	Proton Coupled Electron Transfer
Pyr	2-(2-pyridylethyl) trimethoxysilane
RHE	Reversible Hydrogen Electrode
Sym str	Symmetric stretching
TCD	Thermal Conductivity Detector
TEM	Transmission Electron Microscopy

ABSTRACT

Unsustainable exploitation of fossil fuel and its massive greenhouse gas emission necessitates the development in alternative energy sources. Chemical fuels (CH_3OH or C_2H_5OH) outperform other choices, such as batteries for their high energy densities, which is key to portability. Electrochemical reduction of CO_2 is capable of producing a wide range of valuable fuels (Syngas, formic acid, methane and methanol, etc.). Converting CO_2 into carbon-based fuels further closes the carbon neutral cycle, which contributes to the effort in reducing global CO_2 emission. Integration of organic ligands with transition metals shows great potential in developing selective electrochemical CO_2 reduction catalyst. Thiols covalently bonding to Au exhibits moeity-dependent catalysis characteristics: 6-fold enhancement in yield with 2-fold increase in selectivity for CO evolution accompanied by the suppression in the competing hydrogen evolution reaction (HER) through ligand induced surface reconstruction to specific sites; 20% increase in selectivity and 3-fold in yield for energy-dense liquid product (HCOOH) were achieved through ligand facilitated proton-coupled electron transfer by leveraging the dissociation constant (pKa) of the ligand functional moiety. Based on the insights on ligated Au electrodes, composite catalyst that integrated proton donating ligand on silica substrate with the strong CO binding Pd nanoparticle was fabricated and showed up to 6-fold selectivity and 2-fold yield increase in CH_3OH production.

CHAPTER 1. INTRODUCTION

Background

Energy is the essential need for the progress and prosperity of human societies. Combustion engines powered with fossil fuel has been the world's primary power source ever since industrial revolution. Utilization of alternative power sources such as batteries, nuclear plants and solar energy flourish in recent decades. Development in solar energy still restrained by the difficulty in storage. As is listed in Table 1.1, few of those energy source can surpass gasoline in terms of volumetric energy density which is a key limitation for transportation-used fuels.

Table 1.1. Fuel energy density

Fuel	Specific Energy (MJ/kg)	Energy density (MJ/L)
Gasoline	45	34.2
Lithium ion battery	0.36-0.87	0.9-2.43
Compressed air	0.30	0.45
H_2	121	0.01
Natural gas (CH_4)	56	0.04
Methanol (CH_3OH)	20	16
Ethanol (C_2H_5OH)	27	21

Batteries require extra space and further reduce space to convey people or freight. Therefore, only liquid fuels are plausible to be a sustainable alternative energy source.

Chemical fuels such as alcohols can also be fed into the existing combustion engines without capital cost in hardware upgrading.

Electrochemical reduction of CO_2 is robust in converting CO_2 into various chemical/fuels (syngas, CH_3OH, C_2H_5OH, etc.). These fuels may be produced using H_2O, CO_2 with renewable energy supplies. In addition to the fuels, the chemicals (HCOOH and aldehyde, etc) produced from CO_2 and H_2O can provide add-in value as ready-to-use chemical commodity.

Chemical fuels derived from CO_2 and water will reduce the consumption of unsustainable fossil fuels as well as the parasitic greenhouse gas emission which answers to call by the UN (Climate Convention in 1992, Kyoto Protocol in 1997 and the Paris Agreement in 2015) for effort to solve the growing threat of climate change. The carbon-neutral cycle is completed by using the CO_2 converted carbon-based fuels.

This work presents novel catalyst engineered to selectively reduce CO_2 to fuels.

This Work

Chapter 1 is an introduction to the motivation of developing catalysis for electrochemical reduction of CO_2. A brief overview on the context of each chapter is also presented.

Chapter 2 covers the literature review on previously published work on electrochemical CO_2 reduction reaction system. The state of art experimental methodology and density functional theory-based simulation brought insights into this work. It includes a peek into the ecological system that inspired idea of inducing ligand effect into catalyst design.

Chapter 3 presents the initial attempt to use ligands on Cu and Au-Cu alloy. The functionalized metal (alloy) exhibits enhanced CO production. This section details the experimental procedures and results. Part of this is included in a Journal of Applied Electrochemistry publication.[1]

Chapter 4 shows that thiols are capable of reconstructing Au surfaces to create low coordinated active sites for CO_2 reduction. Experimental results are interpreted with supported DFT calculations. The manuscript on this study is currently under preparation for publication.

Chapter 5 further studies the thiol- Au system that alters the selectivity from CO production to formic acid on Au by facilitating proton coupled electron transfer in hydrogenation with the presence of ligand. Detailed experiments and surface characterization were carried out on the catalyst. The experiment results are presented and interpreted with Butler-Volmer equations from kinetics perspective. A modified proton coupled electron transfer mechanism will be proposed. This work was published in Journal of the American Chemical Society.[2]

Chapter 6 evaluates the catalysts engineered based on the insights from previous chapters. Pd was chosen as the metal center in various form (thin film, dispersed particle and carbon supported nanoparticle), while Si serves as the support for both metal and ligand from functional siloxanes. Experiment details and results will be presented. Metal-ligand interface appeared to be effect method in selective hydrogenation reaction. The work was published in ECS Transactions.[3]

Chapter 7 is a conclusion on this dissertation, from the origin scheme of designed electrocatalyst for CO_2 reduction to the findings in ligated electrodes, and the application in

interface engineering for selective catalyst. Schemes for continuing development are proposed for rational engineering design to achieve an industrially viable process.

CHAPTER 2. LITERATURE REVIEW

The electrochemical reduction of CO_2 is considered to have multiple advantages (high-energy density fuels and environmental-friendly) for energy storage. Conceptually, the electrical energy from renewable energy sources is supplied to an electrolytic cell. CO_2 (e.g. from industrial emissions) can be collected, fed into the cell and obtain electrons to be reduced into chemicals/fuels at the cathode. The oxygen evolution reaction (ORR) takes place at the anode. (Figure 2.1 illustrates the overall scheme of this process.)

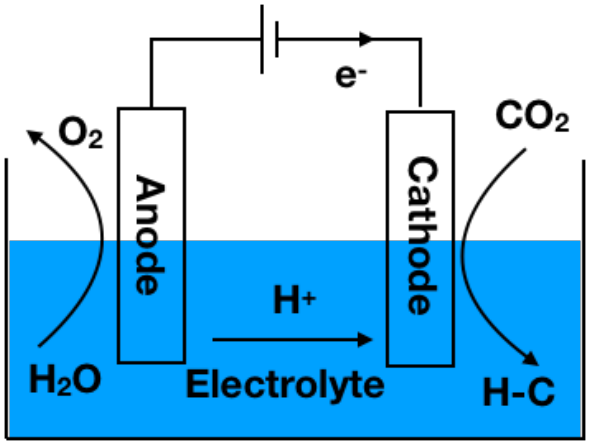

Figure 2.1. Scheme of CO_2 electrochemical reduction cell.

A commercially viable process requires the development of several factors: including reliable and low-cost source of renewable electricity, effective CO_2 capture and purification, productive CO_2 reduction reactions and adequate product collection and separation. The development in the renewable electricity has reduce the cost to as low as \$0.044/kW-hr which is much less than \$0.11/kW-hr from coal-based plant.[4] Commercial CO_2 capture and separation unit has been operating in the field. Mitsubishi's newly installed united offers a recovery capacity of 283 metric tons per day from its chemical plant. [5] The product

separation has yet to be thoroughly considered. This work focuses on the electrocatalysis, mainly selectivity and yields in the electrochemical reduction of CO_2.

History

CO_2 is the combustion product from fuels. Converting it back to chemicals/fuels is equivalent to the reverse of combustion process; therefore sufficient energy input is required. The first observed experiment of electrochemical CO_2 reduction date back to 19th century, in which the formic acid (HCOOH) was produced using a Zinc cathode as the catalyst.[6] This topic has received renewed attention since 1980s due to the price increase in fossil fuels. Hori et al. explored the CO_2 reduction on various metal catalysts in aqueous electrolyte. HCOO- dominates at Cd, In, Sn and Pb cathodes; CO is the primary product on Au[7] and Ag; H_2 evolution predominates on Ni, Fe and Pt.[8] Cu exhibited its unique catalytic performance in giving appreciate amount of CO and hydrocarbons (CH_4, C_2H_4, C_2H_5OH, HCOOH, etc.).[9] Table 2.1 is the reprint of Hori's work that reported detail product distribution from CO_2 reduction.[8] The potential was reported with respect to standard hydrogen electrode (SHE). Note, the SHE forms the basis of the thermodynamic scale of oxidation-reduction potentials based on the redox couple of ideal protons in solution (activity=1) and standard hydrogen (p=1 bar). This seminal work marked new era of this research topic.

Table 2.1. CO_2 reduction product distribution at various cathodes

Electrode	Electrode potential	Faradaic efficiency/%, Lower limit/upper limit				
	(V vs. SHE)	$HCOO^-$	CO	CH_4	H_2	Total
Cd[a)]	-1.66±0.02	65.3/67.2	6.2/11.1	0.2	14.9/22.2	93/100
Sn [a)]	-1.40±0.04	65.5/79.5	2.4/4.1	0.1/0.2	13.4/40.8	94/100
Pb [a)]	-1.62±0.03	72.5/88.8	0.3/0.6	0.1/0.2	3.8/30.9	94/100
In [a)]	-1.51±0.05	92.7/97.6	0.9/2.2	0	1.6/4.5	93/102
Zn [a)]	-1.56±0.08	17.6/85	3.3/63.3	0	2.2/17.6	90/98
Cu[b)]	-1.39±0.02	15.4/16.5	1.5/3.1	37.1/40.0	32.8/33.0	87/92
Ag [b)]	-1.45±0.02	1.6/4.6	61.4/89.9	0	10.4/35.3	99/106
Au [b)]	-1.14±0.01	0.4/1.0	81.2/93	0	6.7/23.2	100/105
Ni [b)]	-1.39	0.3	0	1.2	96.3	98
Fe [b)]	-1.42	2.1	1.4	0	97.5	101

a) Current density: 5.5 mA/cm^2. b) Current density:5.0 mA/cm^2. Concentration of $KHCO_3$: 1.0 mol/dm^3 for Cu electrode and 0.5 mol/dm^3 for other electrodes.

Thermodynamics

From the thermodynamic point of view, the reactions should be readily achievable. Table 2.2 summarized the Gibbs free energy of reactions and converted reversible potential

($\Delta G = -nFE^0_{rxn}$, where F is the Faraday's constant, n is the number of electrons transferred per reaction, and the E^0_{rxn} s are reported with respect to reversible hydrogen electrode (RHE). RHE is the PH independent standard hydrogen electrode (SHE). Since the activity and concentration of proton are defined as unity and 1 mol/l at standard condition, the standard Gibbs formation energy is correlated to the potential in RHE scale). The Pourbaix diagram (figure 2.2) shows the potential dependency on pH.

Table 2.2. Thermodynamic equilibrium data for CO_2 reduction

Reaction	$\boldsymbol{\Delta G}$ (kJ/mol)	$\boldsymbol{E^0_{rxn}}$ (V vs. RHE)
$\boldsymbol{CO_2 + 2H^+ + 2e^- \rightarrow HCOOH}$	3.86	-0.02
$\boldsymbol{CO_2 + 2H^+ + 2e^- \rightarrow CO + H_2O}$	20.09	-0.10
$\boldsymbol{CO_2 + 8H^+ + 8e^- \rightarrow CH_4 + 2H_2O}$	-123.50	0.16
$\boldsymbol{2CO_2 + 12H^+ + 12e^- \rightarrow C_2H_4 + 4H_2O}$	-81.05	0.07
$\boldsymbol{CO_2 + 6H^+ + 6e^- \rightarrow CH_3OH + H_2O}$	-5.79	0.01
$\boldsymbol{2CO_2 + 12H^+ + 12e^- \rightarrow C_2H_5OH + 3H_2O}$	-92.63	0.08

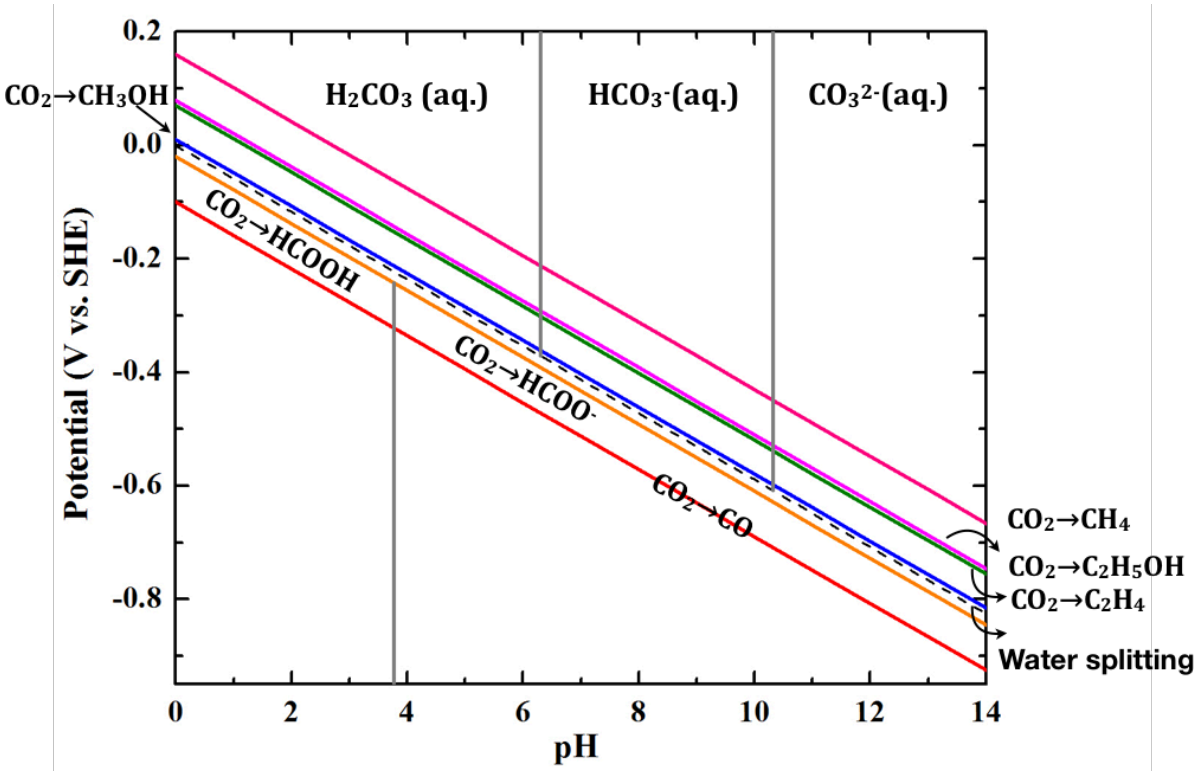

Figure 2.2. Pourbaix diagram for CO_2 reduction in H_2O at 25 °C. (Dash line represents HER)

However, the actual reactions were reported to take place at much more cathodic potential than the equilibrium potential which indicates higher energy input requirement. The chemical stability of linear centrosymmetric CO_2 molecule contributes to the rather high activation barrier for the chemical adsorption to form $CO_2^{\bullet-}$ (Eq. 2.1).[10] In addition to the thermodynamic uphill for the initiation, the competing hydrogen evolution (Eq. 2.2) from the proton H^+ is also consuming the flowing electrons therefore the energy efficiency is lower.

Equation 2.1 $CO_2 + * + e^- \rightarrow COO^{\bullet -}$ E=-0.41V vs. RHE[11]

Equation 2.2 $2H^+ + 2e^- \rightarrow H_2$ E=0 V vs. RHE

Ever since Hori's seminal work showing hydrocarbons from CO_2 reduction on Cu, numerous studies have been conducted on every aspects of this system including experimental parameters, anode catalyst, electrolyte, and cathode catalyst, in order to achieve an economically viable.

Experimental Parameters

There are relatively few experimental parameters can be tuned in the system including: gas flow/ solution flow rate, residence time, temperature and pressure, etc. From energy efficiency point of view, temperature and pressure are rarely considered. 2 compartment cells, 3-electrode reactors, and gas diffusion electrodes have been used as set up to evaluate the performances. Billy et al. [12] have demonstrated that changing the experimental parameters such as gas flow/solution flow rate can change the C_2H_4/CH_4 selectivity ratio by altering the CO_2 flux at the Nernst diffusion layer. Standardized experiment configuration will be important to evaluate catalyst performance. In order to realize large-scale pilot, a reactor design that can minimize the mass diffusion resistance will be necessary.

- Anode:

Most studies to date focused on the cathode catalyst development, therefore, in order to make direct comparison, Pt is often used as anode catalyst for oxygen evolution reaction (OER). Sichao et al[13] studied the implement of IrO_2 as anode catalyst that improve the activity of OER and lower the onset cell potential. Jingjie et al. chose hydrogen oxidation reaction as the anode side.[14] Tedd and Eric used Ru-based in anode in chlor-alkali for chlorine evolution

reaction.[15] Trials on alternative anodes showed possibility to further improve this energy storage technique to integrated with sustainable chemical industry.

- Electrolyte

The studies on supporting electrolyte diverged into two categories: aqueous electrolytes and ionic liquid mixed electrolytes. For aqueous electrolyte, PH and ionic species are considered two most important descriptors. Whipple et al. showed significant increase in formic acid production on Ru-Pd with acidic electrolyte.[16] Hori et al. measured product selectivity in different electrolyte buffers, and found the selectivity toward specific hydrocarbon depend on the availability of local proton concentration.[9] Verma et al. observed current density increases with the increase of concentration in ionic species regardless of anion species at same pH value.[17] later studies by Singh et al. found that the Faradaic selectivity switch from H_2 and CH_4 to CO, C_2H_4 and C_2H_5OH as the cation size increases.[18] The ionic liquid mixture electrolyte was tested for its unique property in bonding with CO_2 to form the complex thereby lower the activation barrier. Rosen et al. observed lowest onset potential for CO production with the 1-ethyl-3-methylimidazolium tetrafluoroborate (EMIM) in acid solution at 1.5 V cell potential.[19]

- Cathode

Most studies to date have been focused on the cathode catalyst for CO_2 reduction in aqueous electrolyte. Scientists surveyed elements in periodic table and their alloys for ideal cathode material. Table 2.3 summarized major products obtained.

Table 2.3. Major production distribution on various metal electrode at room temperature and pressure in aqueous electrolyte. Pt serves as auxiliary electrode.

(A)$HCOO^-$ formation		(B) CO formation		(C) Hydrocarbon formation	
Metal	Major products	Metal	Major products	Metal	Major products
Pb,Hg,Ti,In, Cd, Bi, Ga	$HCOO^-$	Au	CO	Cu, Cu_2O	CH_4, C_2H_4, C_2H_5OH, $HCOO^-$
Sn, Sn-Cd, Sn-Pb, Sn-Zn	$HCOO^-$	Ag	CO	Cu-Ni, Cu-Fe, Cu-Cd	CH_4, C_2H_4, CO
Hg/Cu,	$HCOO^-$	Zn	CO, $HCOO^-$	Cu-Ni, Cu-Sn, $Cu_{88}Sn_6Pb_6$, Cu-Pb, Cu-Cd	$HCOO^-$, CO
Ru-Pd, Pd-Pt	$HCOO^-$	Pd	CO, $HCOO^-$	Cu-Au[21]	CH_4, C_2H_4, $HCOO^-$,C_2H_5OH, C_3H_7OH-1
		Ga	CO	Cu-Ag[22]	CO, C_2H_4, CH_3CHO C_2H_5OH
		Ni-Cd alloy	CO	Cu-Zn[23]	C_2H_5OH
		Cu-Pd[24]	CO	RuO_2/TiO_2	CH_3OH
		Ni on N-doped graphene[25]	CO	$Cu_2O/PdCl_2$	C_2H_5OH
		Cd[26]	CO	Pd/SnO_2[27]	CH_3OH

In addition to the problem of the competing HER, most of surveyed catalysts are limited to the production of $2e^-$ products: CO or HCOOH, products that have lower energy densities when compared with hydrocarbons and alcohols. Cu's unique performance in yielding high value hydrocarbon products (CH_4: 40%, $HCOO^-$: 16%, H_2: 33% in Faradayic Efficiency, FE) attracted extensive studies in order to uncover the mechanism for hydrocarbon production. Experimentally, Hori examined the crystal facet dependent product selectivity with a series of Cu single crystal and found the promoted C_2H_4 formation coupled with suppressed CH_4 formation on higher order crystal orientation.[28] The discovery suggested that selectivity is sites specific. In 2012, with the low volume reactor design, Kuhl et al.[29] detailed the whole picture of the addition products (including CH_3OH, n-propanol, ally alcohol, glycolaldehyde, acetaldehyde, acetate, ethylene glycol propionaldehyde, acetone, hydroxyacetone, total in 11% FE. When CO was fed into the system as the reactant, formation of the same hydrocarbon and alcohol indicates that CO is likely an important intermediate product. [30-31] Contrary to the prosperous product distribution from CO, the use of HCOOH as staring reactant didn't give further reduction products.[32] In order to look for the intermediate hydrogenation step, Hori et al. studied the infrared (IR) spectroscopy on biased surface adsorbed CO and suggested that the formation of surface hydridocarbonyl complex is the preceding step to further reactions.[33] [34]However, spectroscopic experiments are not sufficient to make a strong statement about intermediates. Firstly, the IR captures all the vibration along its pathway, therefore it's hard to distinguish between surface adsorbed species and solvated species. Secondly, the hydrogenated CO intermediates have never been detected to prove its existence. The high turnover frequency (TOF) of surface species and interfering signal from solvated species in electrolyte increased the difficulty for mechanism

study in this case. Despite great amount of work such as the implement of ultra-fast sum frequency generation IR (SFG-IR) spectroscopy[35] in monitoring surface adsorbed intermediates have been dedicated to improve experimental technique seeking for real piece of evidence to either support or undermine the proposed mechanism, no striking achievement has been achieved yet.

Computational Mechanistic Insights

Though these mentioned experimental studies on the reaction mechanisms were not satisfactory, density function theory (DFT) based calculations provide another route to examine the reaction mechanisms. Different groups suggested mechanistic pathways based on their theoretical calculations are summarized the schemed presented in figure 2.3. Peterson et al.[11] used a computational hydrogen electrode (CHE) model to show the mechanistic pathway of CO_2 reduction. Corresponding well with the experiment results, CO vs. HCOOH are considered as the first diverging point where the first pair of proton coupled electron transfer happens with different mechanisms. Most groups agree that the reduction start from forming –COOH on surface until later Feaster et al. proposed the volcano correlation between the binding energy of *OCHO and the formation of HCOO-.[36] The next critical step toward hydrocarbon routes lies at the hydrogenation of adsorbed CO where different simulation groups have been under debate. Nørskov and Peterson[11] suggested that the proton in the second pair of proton-electron attack the C atom of CO while Asthagiri and Janik [37]suggested that the attack occurs on the O atom of CO with the addition of solvated water in the simulation system. The argument between two proposed intermediates is hard to prove with the feeding experiment due to the instantaneous life time of intermediates, therefore theoretical simulation stands out as the most prominent method in understanding

the mechanisms to date. Due to the inevitable involvement of H^+ in the reactions, the competing HER was also investigated in all simulations.

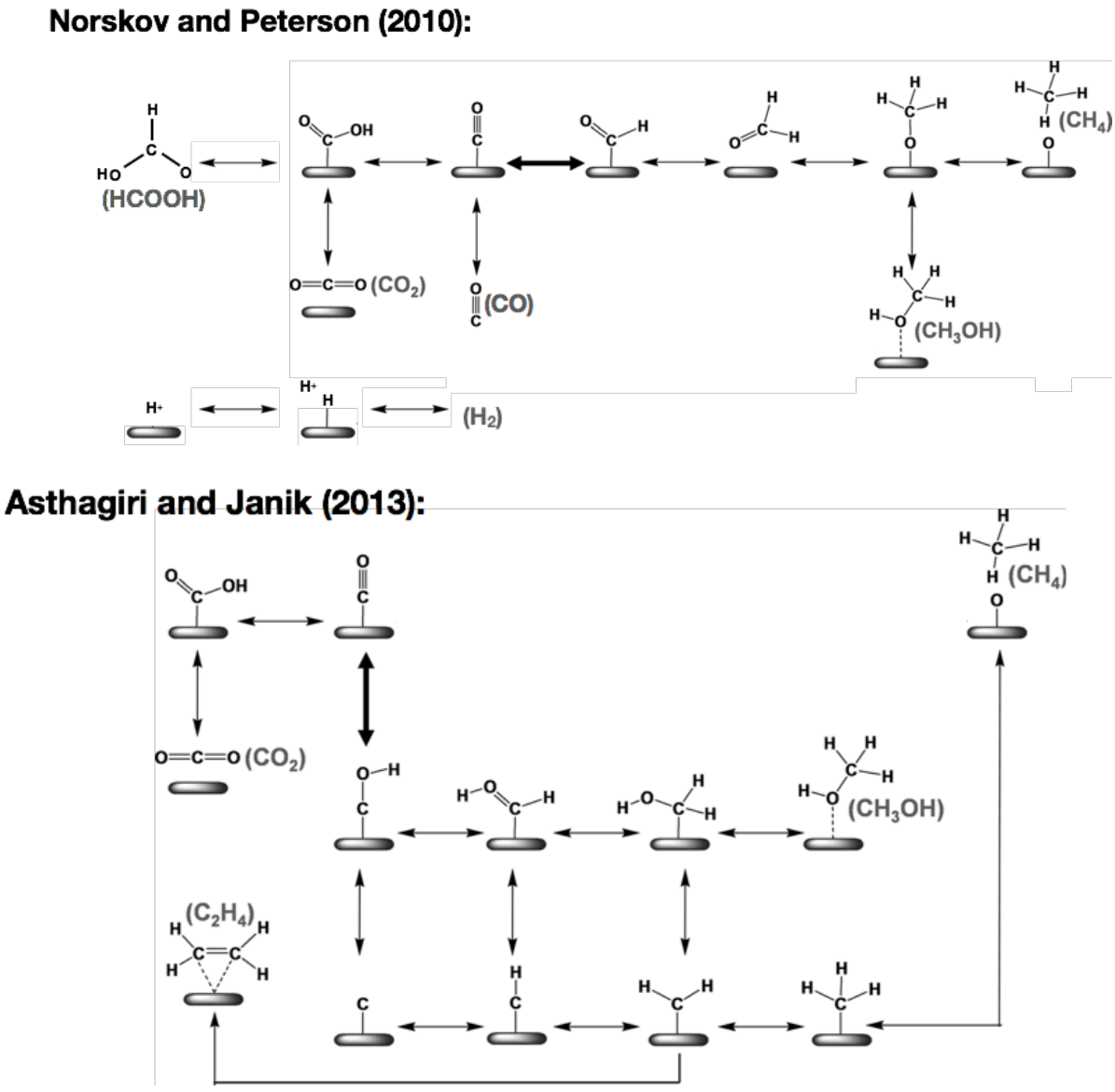

Figure 2.3. Simulation suggested reduction reaction pathways on Cu.

Calculations on different surface structures were studied including the effect of adsorbates-adsorbates interactions. The largest deviation on binding energy of intermediates between (111) and (211) is for the *COOH binding. Weak CO binding metals

show preference toward gas phase CO instead of further protonation to CO* for hydrocarbon production. High coverage of CO results in promotion effect of HER and has no effect on the scaling trend for protonation of CO*. Among all the transition metals, Cu lies at the top on the volcano plot (shown figure 2.4). The volcano plot presented by Nørskov et al. showed the limiting potential for CO hydrogenation to happen on (111) and (211) surface of several metals. The limiting potential was defined at which each reaction between surface- adsorbed species becomes exergonic.[38]

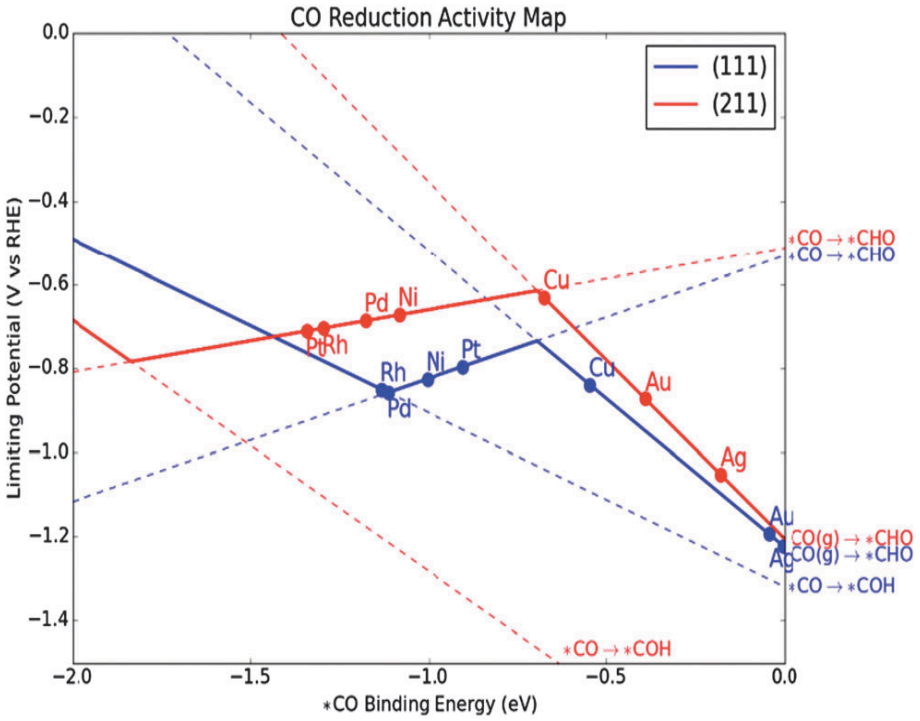

Figure 2.4. CO hydrogenation limiting potential activity map to hydrocarbons.

Though Cu lies on the top of the volcano plot, it is still not the ultimate solution to this problem. Figure 2.5 shows the scaling relationship presented by the same research group. As is shown, the limiting potential for HER is always less than CO hydrogenation (i.e. more facile) regardless of crystal facet or transition metal.

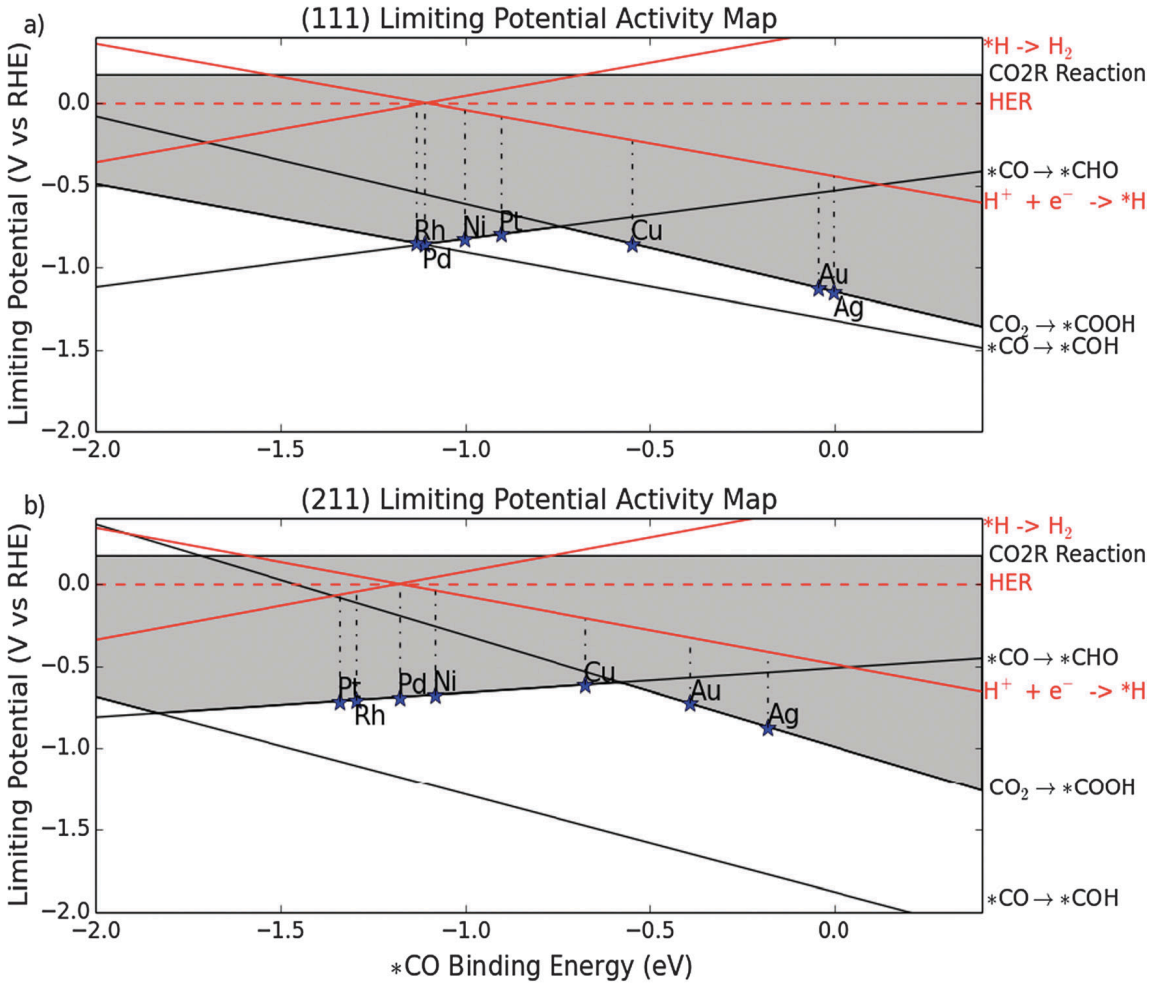

Figure 2.5. Limiting potentials for mechanistic steps in CO_2 reduction and HER on (111) and (211) metal surface.

Despite the elusive mechanism steps, those studies provided several new insights in designing the electrocatalysts:

Firstly, the binding energy of intermediates can be different on different surface structures and yield different product selectivity which corresponds well with Hori's study on Cu single crystal further.[28] Therefore, the selectivity of reaction product can be tuned by engineering catalysts with certain active surface sites that favor particular reduction pathway.

Secondly, DFT simulation is a strong initial screening method in searching for catalyst candidates by leverage the surface binding energy.

Thirdly, an selective catalyst that favor the hydrocarbon formation better than Cu will require special design that can break the scaling relationship between *CO, *COH, *CHO and *COOH.[39]

Methodologies

To break the scaling relationships described above, various methodologies have been pursued to engineer the cathodic catalyst such as: metal alloys, nanoparticles and oxide derived catalysts, etc.

- Metal Alloys:

Wantanabe et al.[40] studied distinct performance of Cu alloy from elemental metals. Later study by Kim et al. [41] on Au-Cu bimetallic nanoparticle and showed the shifting in the d-band energy level correlate with the activity of reduction. Ma et al.[42] investigated a range of Cu-Pd bimetallic catalyst and correlated the product selectivity with the atomic arrangement. They proposed the atomic arrangement affect the migration of surface adsorbed species and certain arrangement promote the coupling process therefore favors the multi-carbon production.

- Nanoparticles:

Nanoparticle has been known to be a magic tool due to the exposure of more low coordinated sites compared with bulk material. Kauffman et al.[43] synthesized the Au_{25} nanocluster which exhibited 7~ 700 times enhancement in CO production rate with low

overpotential requirement. Zhu et al. reported size-dependent catalytic behavior for Au nanoparticle and achieved 97% Faradayic efficiency (FE) for CO production at -0.52 V (vs. RHE). Their further DFT calculation pinpointed the active CO production sites to be the edge site versus HER on the corner sites. [44] Implementing the discovery in sites selectivity, they went on engineered Au nanowire (high edge to corner ratio) which achieved 95% FE at -0.2V (vs. RHE).[45]

- Oxide derived catalysts:

Oxidized Cu was reported to favor the methanol synthesis in gas phase CO2 hydrogenation.[46] Previous work in our lab studied the oxidized Cu in this electrochemical reaction and found that Cu(I) plays a critical role in CH_3OH production. [47] However, the effective Cu(I) sites suffered from the instability at reduction potential for CO_2. Upon this discovery, Li et al[48]. took a deeper investigation and found that the ability for Cu(I) to tune the product selectivity depend on the initial thickness of prepared Cu_2O but with the preference toward CO and HCOOH production. Their study on oxide-derived Au electrode,[49] on the other hand, exhibited 200mV anodic shift for CO production which was attributed to the extraordinary stabilization of $CO_2^{\bullet-}$ on the surface. The reported oxide-derived catalysts are all subject to the surface roughening to certain extent therefore exhibit enhanced production yield. The equilibrium between redox states of metal catalysts are proposed to create more active sites for the reactions.

Inspiration from Nature

Artificial approaches to date are nowhere near the natural photosynthesis in terms of

selectivity to energy-dense oxygenates. Photosynthesis is known to convert light energy into chemical storage with enzymes in plants. Sugars are usual carbohydrates form for chemical energy storage. Contrary to the multiple defects (selectivity or efficiency) in artificial process, photosynthesis owns its unique selectivity toward glucose (one kind of sugar, high energy density as 23.9 MJ/L). The Calvin cycle is the widely accepted route for the energy storage. Figure 2.6 shows the consecutive Calvin cycle: carbon fixation, reduction reaction and enzyme regeneration. Ribulose 1,5-bisphosphate (RuBP) captures CO_2 from the atomosphere to form 6 carbon unstable intermediates with the catalyzation by ribulose bisphosphate carboxylase oxygenase (RuBisCO) enzyme and uses the reduced Nicotinamide adenine dinucleotide phosphate (NADPH) to form three-carbon sugars with ATP as the energy supply.

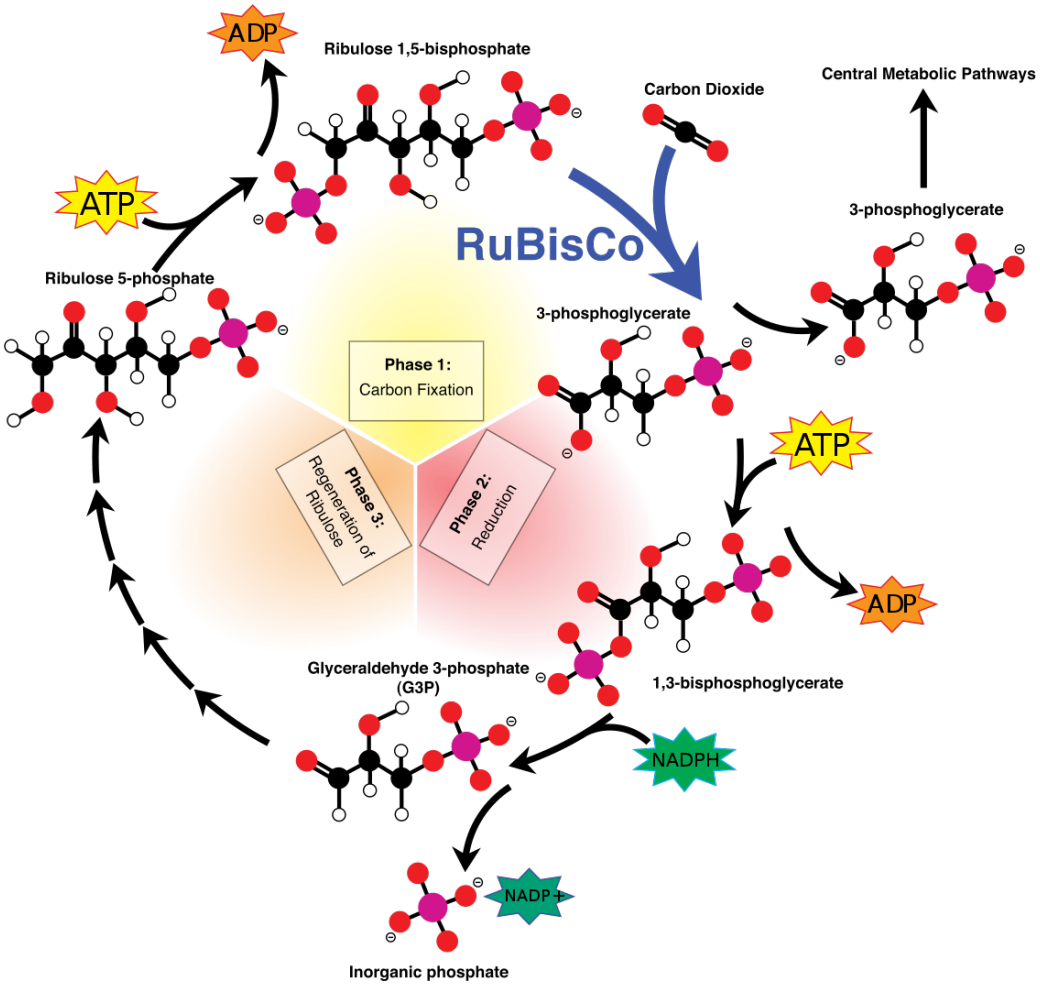

Figure 2.6. Calvin Cycle (Licensed under CC BY-SA 3.0 by OpenStax)

After the first chemical reaction for carbon fixation, the NADPH facilitated reduction reaction is replenished with fresh proton from the supporting the proton coupled electron transfer reaction between $NADP^+$ and NADPH through z scheme (shown in figure 2.7). Light activated Photosystem II extracts electrons and protons from water. The electrons are transferred through cytochrome ($Cyth_6f$) to plastocyanin (PC), which further feed electrons to light- oxidized photosystem I (PSI). The PSI pumped electrons to reduce the ferredoxin (Fd) for the NADPH production. Along the electron transfer, protons are transferred through

plastoqunione (PQ) to Fd. [50]

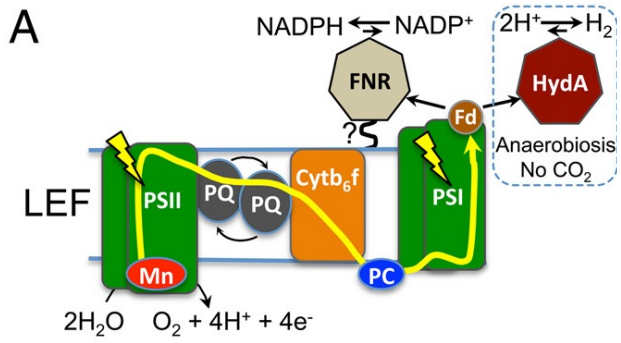

Figure 2.7. Z scheme

In the photosynthesis system, PC is a copper-containing protein with a single copper center ligated two histidines, a methionine and a cysteine.[51] Cytb6f is iron centered with ligated hemeprotein. Fd is an iron-sulfur protein. PQ and RubisCO are organic molecules. It is possible that natural achieved its selectivity with the leverage between metal and organic ligand in an oxidation and reduction reaction. DFT based model developed by Hansen et al. evaluated the CODH enzymes and suggested that the stabilization of hydrogen from ligands (lysine, histidine and cysteine) display a considerably more favorable sites than any metal on the volcano plots.[52] All these suggest that counting the ligand into the system should be the prominent to break the scaling relationship to realize the efficient energy storage like nature does.

Despite of the selectivity advantage, only 3~6% of energy efficiency in natural is outweighed by the synthetic process in terms of kinetics. Decent energy efficiency for CO_2 reduction has been reported as high as 22%.[53] In order to achieve an ideal energy efficient catalyst, an inference from natural and to date artificial process is that we should adapt natural's strategy in catalyst design while implement human power control.

If we take another look into the recently reported nanoclusters, the ligand is always involved though the original intention for adding them was to stabilized the nanocluster structure. The reported Au_{25} nanocluster that yielded 7~700 times CO compared with bulk Au foil was stabilized by 2-phenylethanethiol.[54] The Cu nanoparticles that enhanced methanation from 40%[8] to 85% were capped with tetradecylphosphonate.[55] The ligand effect could have always been overlooked under the overwhelming nano-size effect. Andrews et al. found that the Nafion immobilized Au nanocluster showed a ~170mV anodic onset potential shift from the polyvinylidene fluoride (PVDF) immobilized same Au nanocluster.[56] Bocarsly's discovery[57] in dosing the electrolyte with pyridine as co-catalyst to form methanol on Pt and Pd electrode also suggest the importance in using organic ligand as a mean to tune the selectivity of the reaction.

Metal-Ligand Interface

To explore the ligand effect in CO_2 reduction, self-assembled monolayer (SAM) on metal substrate was firstly investigated. The organic molecules adsorbed spontaneously onto the substrate and self-organized to a well-ordered domain. SAM molecules are consisted of a head group, tail and functional group at the end. Thiols and Silanes possess head group that has strong affinity to the Au and Si substrate surfaces, respectively. Therefore, stable covalent bonds will form upon chemical adsorption. SAM has been implemented extensively in electrochemical system in applications such as corrosion inhibition, dielectric barrier and lithography, etc. The end functional group provides additional degree of freedom to investigate the organic ligand effect in catalyzing CO_2 electrochemical reduction.

The ligand has a few advantages: Firstly, the ligand on bulk metal can avoid the

shadow from size effect. Secondly, no evidence has indicated that the ligand is restricted by the scaling relationship. Lastly but most importantly, ligands relaxed the limitation of same sources for electron and proton supplied to the reduction reaction and provided additional variables such as electronic interaction, hydrophobicity and conductivity, etc.

In summary, to achieve practical application of electrochemical CO_2 reduction, the catalyst must be selective and efficient. Based on the literature review, the ligated electrodes hold great potential in facilitating selective reactions which can circumvent the scaling relationships

CHAPTER 3. Cu BASED CATALYST (ALLOY AND LIGAND) FOR CO_2 ELECTROCHEMICAL REACTION

Introduction

Previous research has shown that Cu has unique ability to catalyze CO_2 reduction to yield various hydrocarbons. Theoretical simulation suggests this should be attributed to its top position on the volcano plot where the co-adsorption of CO and H reached balance for optimal catalytic activity.[58] Previous reviews provide insight that strategic design can be the separation of electron transfer source and protonation source. Here we studied two methods in utilizing Cu's uniqueness to enhance the production rate of hydrocarbons via Au-Cu alloy and Ligand SAM on Cu foil.

Cu-based bimetallic alloys were studied previoulsy.[40] Low overpotential with selective Cu alloys were examined for CO_2 reduction in carbonate electrolyte. Cu-Ni alloys appear to produce CH_3OH and HCOOH, and other Cu-based alloys (such as Cu-Zn, Cu-Cd or Cu-Ag) demonstrated catalysis that deviated from their parent metal which indicates possible solution to the limiting scaling relationship. Catalysis with Cu-Au alloys (in various elemental atomic ratios) at -1.9V vs. Ag/AgCl in phosphate electrolyte were studied by Christophe and his coworkers.[59] Efficient CO production was reported on $Au_{50}Cu_{50}$ though at the expense of possible further hydrogenated species (such as CH_4 or CH_3OH) production. Synergistic geometric and electronic effect for CO_2 reduction were also observed with Au-Cu alloys in nanoscale in which the d-band centers were found shifted and consequently shifted the catalytic performance.[41] In the first part of this chapter, we evaluated the potential

dependent CO_2 reduction catalytic performance of Au-Cu alloy at various weight compositions in carbonate electrolyte.

We evaluated the performance of ligand modified Cu foil in CO_2 reduction reaction to investigate the ligand effect that was buried under the size effect of nanoparticle. Glutathione (structure shown in Figure 3.1 (a)) [60] and 2-phenylethylthiol (shown in Figure 3.1 (b))[61] are two common capping ligands for nanoparticle synthesis, therefore we started from these two ligands. The glutathione modified Cu showed great enhancement in CO production which arouse the interest for further investigation. Since glutathione is a complex ligand with multiple functional moieties, thiols with each individual moiety were investigated (structures shown in figure 3.1).

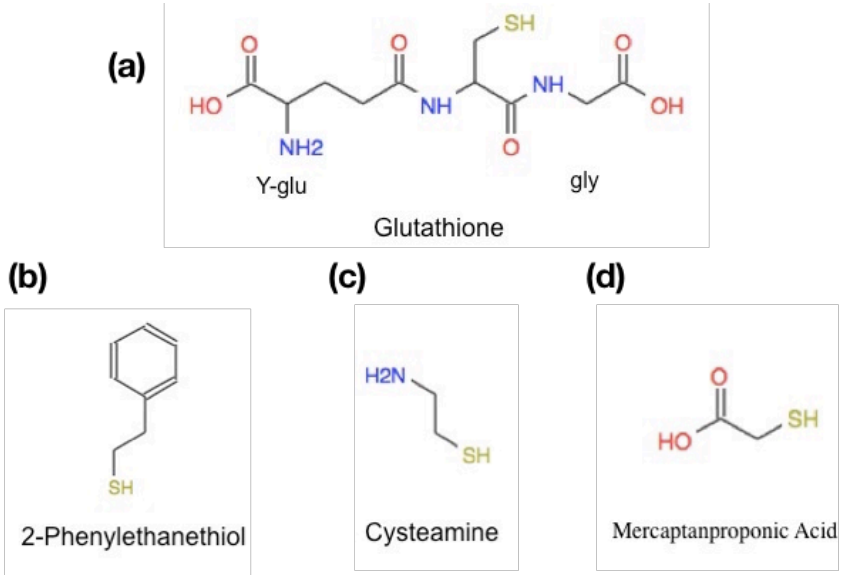

Figure 3.1. Chemical Structure of ligands

Experimental

Electrode Preparation

Cu (99.99%), Au (99.99%), Au-Cu 50%wt (99.99%), Au-Cu 75%wt (99.99%) and Au-Cu 90wt% (99.99%) were obtained from ESPI metal. The unfunctionalized foils were rinsed with deionized (DI) water (MegaPure system) and serve as working electrode. The functionalized foils were rinsed in DI water followed by the solvent of ligands copiously before being immersed into the 10mM Glutathione (GSH) (Sigma-Aldrich, >98%) aqueous solution, 10mM 2-phenylethylthiol (2-PET) (Sigma-Aldrich, >98%) ethanolic solution, 10mM 2- Mercaptoproponic acid (2-MPA) (Sigma-Aldrich, >95%) ethanolic solution, 10mM cysteamine (CYS) (Sigma-Aldrich, >98%) aqueous solution for 10 min, respectively. The functionalized electrodes were then removed from the solutions and rinse with the solvent to remove the excess physically adsorbed species followed by DI water to remove the solvent molecules. Fresh prepared electrodes were used at each experiment to ensure the consistency.

Electrochemical Methods

The reduction reactions were carried out in a 2-compartment-3-electrode cell set up. The Pt wire was used as counter electrode. 2 compartments were speparted by the 117 Nafion membrane (FuelCellsEts). The potentials of working electrodes were measured with respect to Ag/AgCl (saturated with 3M NaCl) reference electrode (BASi, RE-5B) by a PART model 263A potentiostat/glvanostat. The uncompensated resistances were measured and manually corrected. The final reported potential with respect to RHE is converted with E (vs RHE) = E (vs. Ag/AgCl)+0.197+0.059*pH. The currents were normalized with the geometric area.

CO_2 (UHP, Airgas) was flow into the cell continuously at a flow rate of 40ml/min through gas dispersion tube at room temperature and 1 atm. The effluent from the cell was auto-sampled in to the gas chromatograph (Shimadzu, GC 2014) that equipped with FID and TCD detectors.

Gas chromatograph is a common analytical technique for components that can be vaporized without decomposition. Individual component can be identified from the retention time on the column. The concentration quantification in the mixture can be determined with the pre-run calibration curve which correlates the known standard concentration with the electric signals on the detectors.

The auto sampling was performed at 15 min interval with applied potential. The concentration of CO and H_2 were analyzed to give the production rate (in express of partial current density) and selectivity (shown in faradaic efficiency).

Self-Assembled Monolayer (SAM) Characterization.

Infrared spectroscopy has been a well-established analytical technique to identify chemical structure by measuring absorbance at characteristic frequency. Surface IR analysis on freshly-prepared electrode proves the successful SAM development. Further analysis on post-reaction sample facilitating in stability analysis.

Ex situ infrared spectroscopy was corrected out on a smart-ITR diamond assembled Nicolet 6700 FTIR spectrometer with a nitrogen-cooled narrow-band MCT detector. Spectra were recorded for the fresh prepared electrodes before reaction. Same electrolysis experiments for were then performed in the same two-compartment electrochemical cell at the most cathodic potentials reported in potential-dependent product distribution. Spectra were taken for each post reaction samples. Interferograms were recorded at a resolution of 0.5 cm−1 and 256 scans.

Result and Discussion

Table 3.1 summarizes the onset potentials for HER and CO_2 RR of electrodes. Noted, no significant difference was found when comparing alloys with pure Au or Cu. Since the onset potentials were determined by the thermodynamic resistance of the catalytic reaction, the possible enhancement in electronic effect can be excluded in the set of alloys.

Table 3.1. Summary of the onset potential for HER and CO_2 RR

Electrode	Onset potential for HER (vs. RHE)	Onset potential for CO_2RR (vs. RHE)
Au	-0.36	-0.42
Au-Cu (10wt% Au)	-0.38	-0.37
Au-Cu (25wt% Au)	-0.37	-0.43
Au-Cu (50wt% Au)	-0.38	-0.44
Cu	-0.34	-0.48

Figure 3.2 shows the potential dependent catalytic performance of Au-Cu alloy in CO_2 electrochemical reduction reaction. At low overpotential (-1.0 ~ -1.15 V vs. SHE), the alloys intend to behave like Cu that favors HER in FE while the FE for CO is lower than the one on pure Au but higher than pure Cu. The partial current density of HER is 2 times higher than the one on Au and approximate j_{H2} on Cu. The fact that j_{CO} is negligible on alloy further consistent with the fact that the onset potentials for CO_2 reduction on alloys are dominated by Cu.

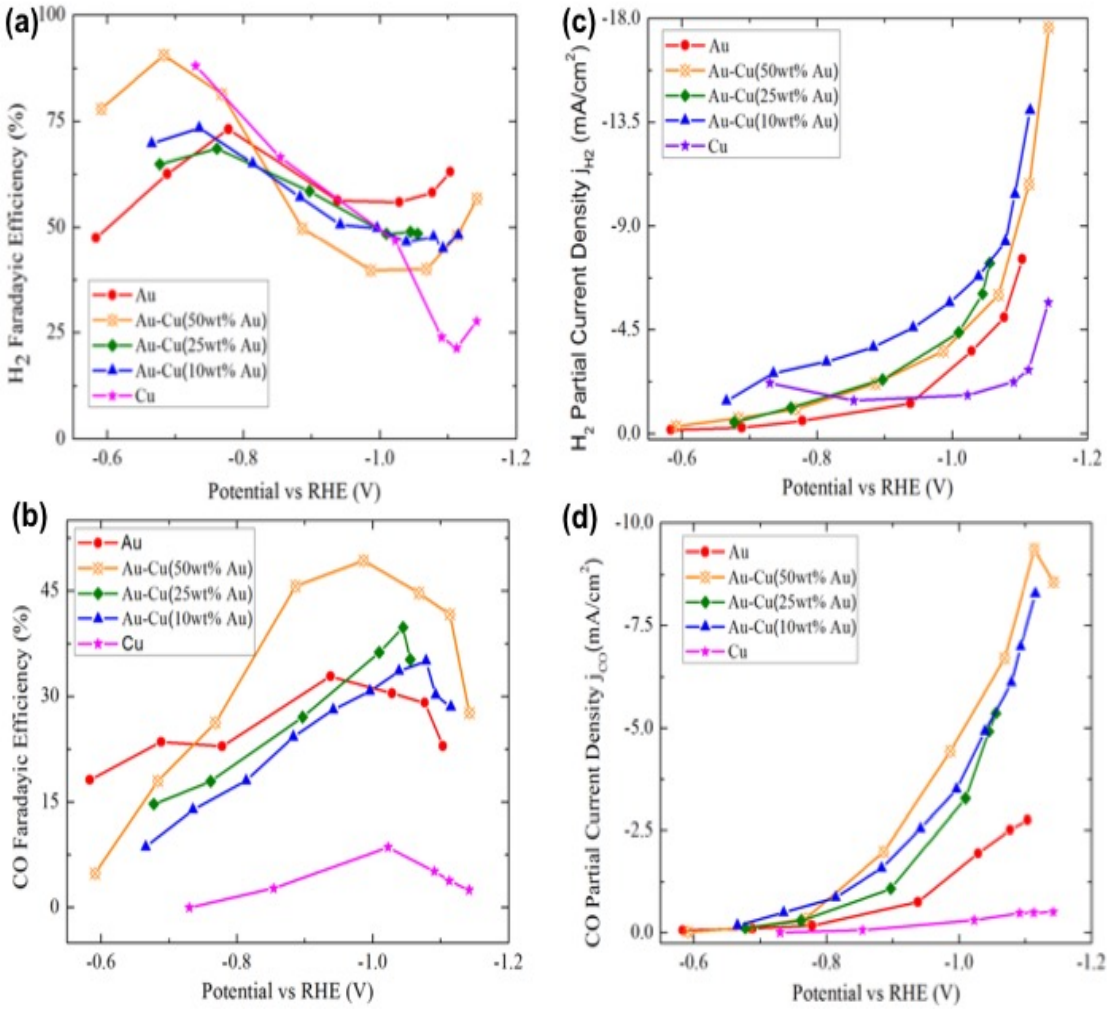

Figure 3.2. Comparison of product (H_2 and CO) partial current density and Faradaic efficiency (FE) on Au-Cu alloys. (a) FE of H_2 formation; (b)FE of CO formation, (c) partial current density of H_2 formation, and (d) partial current density of CO formation

At medium overpotential (-0.75 to -0.9 V vs. RHE), low Au content alloys (10 wt% and 25 wt%) starts to behave like the addition of Au and Cu in terms of the selectivity, while j_{CO} and j_{H2} both shown up to 5x enhancement. Since this potential range is out of the thermodynamically controlled region, the enhanced productivity can only be attribute to the kinetics of the reaction. The enhanced reaction kinetics can be resulted from either the increased catalytic active sites on alloy electrodes (same reaction condition exclude the

possibility of enhanced surface concentration for CO_2 or H^+) or accelerated CO desorption rate or both. Previous studies has suggested weaker bonding of CO on Au compared with Cu on volcano plot[39], the addition of Au to the copper could have resulted in weakened bonding of CO and further enhanced CO production rate by increasing CO desorption rate. The reduced further hydrocarbon production results from diminished available surface adsorbed CO for further hydrogenation.

Remarkably, the Au-Cu (50wt%) alloy shows a greater preference (up to 10% more) toward CO evolution, such preference was also exhibited in the partial current densities where the j_{CO} is even higher than other alloys. Therefore, it can be concluded that Au-Cu alloy behaves like "super Au" with the addition of Au content to certain ratio. Outstanding CO production on Au- Cu (50wt%) suggests that the intermediates' binding energy reach the optimal at this ratio.

At large overpotential (> -1.3V vs. SHE), the selectivity toward CO evolution was enhanced by 5 times from optimal 8% to 40% (at -1.3V vs. SHE) with the addition of Au and 5~15% higher than Au foil. The selectivity towards CO kept increase to >50% at -1.4V vs. RHE with 50 wt% Au was added which is higher that the optimal 36% on Au itself while the FE for HER showed the opposite trend. The FE for methane production is almost negligible. The shift in product selectivity should all be attribute to the shift in the binding energy shift from alloy effect as was suggested in previous literature.

Another strategy to engineer the Cu based catalyst is to implement the surface ligand chemistry. Figure 3.3 summarized the catalytic performance of ligand functionalized Cu and compared with Cu foil. The presence of 2-PET on the surface almost deactivated the catalysis for CO_2 reduction and left only the HER. Similar effects happened on MPA-modified Cu. The

S was expected to poison the catalytic sites activity in traditional catalysis.[62] However, GSH and CYS showed unexpected enhancement in catalytic performance.

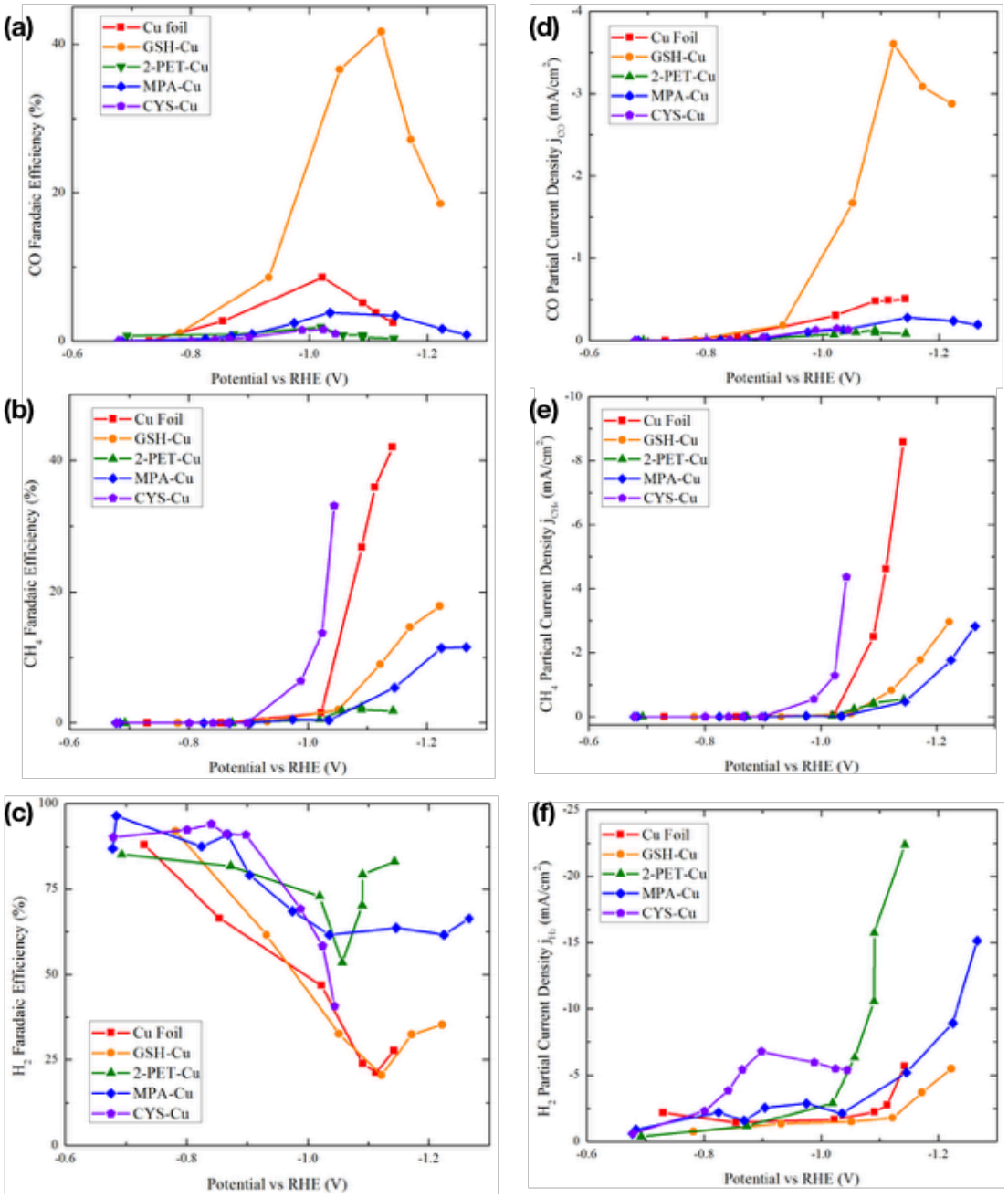

Figure 3.3. Comparison of product (H_2, CO, and CH_4) partial current density and Faradaic efficiency (FE) on (functionalized) Cu. (a)FE of CO formation, (b) FE of CH_4 formation, (c) FE of H_2 formation; (d) partial current density of CO formation, (e) partial current density of CH_4 formation and (f) partial current density of H_2 formation.

GSH-Cu showed remarkable performance in CO production over the entire range potential of interest contrary to the suppression effect on rest ligand-functionalized sample. The optimal FE for CO was increased from 8% to 40% (~5x) with the partial current density from 0.5 mA/cm^2 to 3.7 mA/cm^2 (~7x) with the FE for CH_4 reduced by half and the FE for HER remain unchanged. The onset potential for CO production remained unchanged, therefore kinetics was left for the reason for this promoted CO yield. However, glutathione is a complicated antioxidant with a carboxyl group, an amine group and a glycine. The fact that controlled experiment with carboxyl group (2-MPA), amine group (CYS) and L-cysteine (no change was found) didn't exhibit same CO production preference exclude the possibility to attribute the observation on Glutathione to single functional moiety. The mechanism of the enhanced catalytic performance with GSH remained unclear. It was speculated here that the glutathione prevent the deactivation[48] or oxidation[47] of Cu to Cu(I) that will yield methanol production. Recent study on glycine modified Cu by Xie et al.[63] showed effective enhancement in hydrocarbon production. Their simulation work suggested that the bonding between CHO* and -NH_3^+ ends of zwitterionic glycine lead to the promoted hydrogenation reaction. Although it was CO instead of hydrocarbon promotion on GSH, the glycine could also be the key to this effect.

On the CYS-Cu, ~100mV anodic shift (from -1.05 to -0.9 V vs. RHE) for CH_4 production onset was observed though at the expense of CO yield. The HER also prevailed at low overpotential. The anodic shift in onset for CH_4 indicates lower energy barrier for CH_4 production. The presence of amine moiety on the surface could result in lower the CO_2 adsorption barrier since the amine scrubbing was known to be used as CO_2 trapping agent since 1930.[64] CO was known to be the key intermediate for further protonation products.

The fact that the suppressed CO yield was compensated by the increased CH_4 production further indicates promoted protonation reaction at the presence of amine moiety. The promoted CO_2 reduction could result in higher surface CO concentration for protonation to happen. The alkalinic amine moiety relaxed the scaling relationship between H binding and CO binding[39]. Though the HER still prevailed, the higher yield for CH_4 was still achieved with the presence of cysteamine on Cu surface.

The stability of the SAM ligand on Cu was evaluated with the iTR experiment. Figure 3.4 shows the IR spectrum of ligand on SAM before and after the electrochemical reduction.

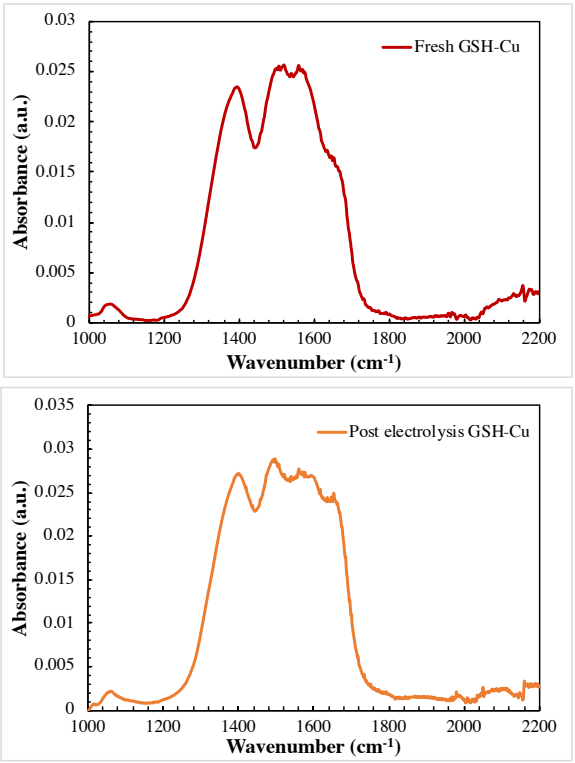

Figure 3.4. ATR-IR spectra for GSH-Cu before and after electrolysis.

Figure 3.4 compares the spectrum of GSH-Cu before and after electrolysis, the vibration wavelength of peaks remained roughly same. On the freshly prepared sample, peak

(i) at 1406 cm^{-1} corresponds to the symmetric stretching in $-COO^-$; peak (ii) at 1526 cm^{-1} corresponds to the N-H deformation in the secondary amine; peak (iii) at 1578 cm^{-1} corresponds to the asymmetric stretching in $-COO^-$; peak (iv) at 1672 cm^{-1} corresponds to the N-H deformation in the primary amine.[65-66] The spectrum on post electrolysis sample didn't show apparent difference in vibration wavenumber, however, the relative intensity of peak (iv) to the other peaks varied which is probably due to the conversion of GSH to ionic form.[67] The lack of in situ data restrained this work to provide further conclusion of surface condition.

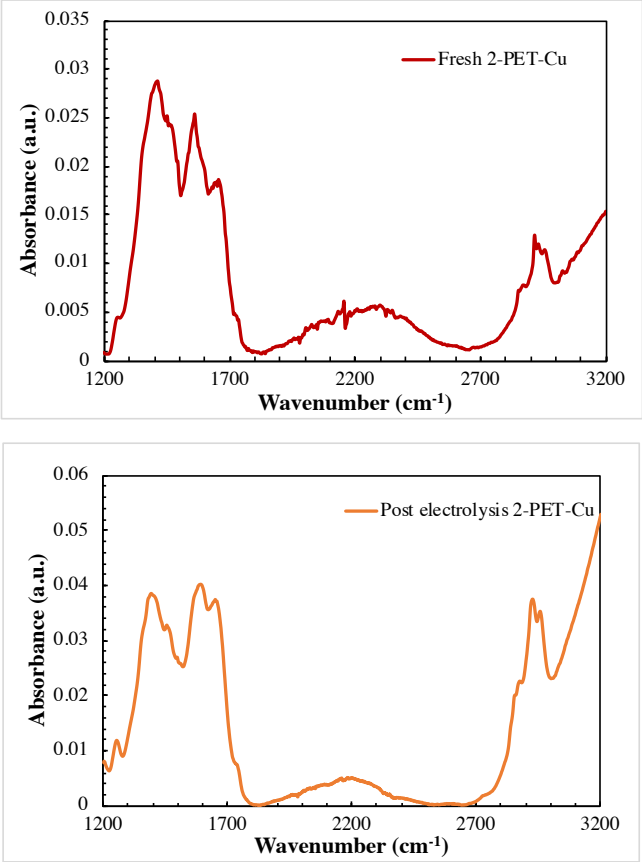

Figure 3.5. ATR-IR spectra for 2-PET-Cu before and after electrolysis

Figure 3.5 presents the IR spectrum of 2-PET on Cu. On the freshly prepared sample, peak (i) at 1259 cm^{-1} corresponds to the =C-H in-plane deformation in monosubstituted benzene; peak (ii) through (v) at 1422 cm^{-1}, 1478 cm^{-1}, 1565 cm^{-1} and 1667 cm^{-1}correspond to the aromatic -C=C- stretching vibration. Peak (vi) and peak (vii) at 2863 cm^{-1} and 2929 cm^{-1} corresponds to the symmetric and asymmetric Alkane C-H stretching vibration, respectively.[66, 68-69] No apparent shift or disappearance of vibration was observed on the spectra of post electrolysis sample.

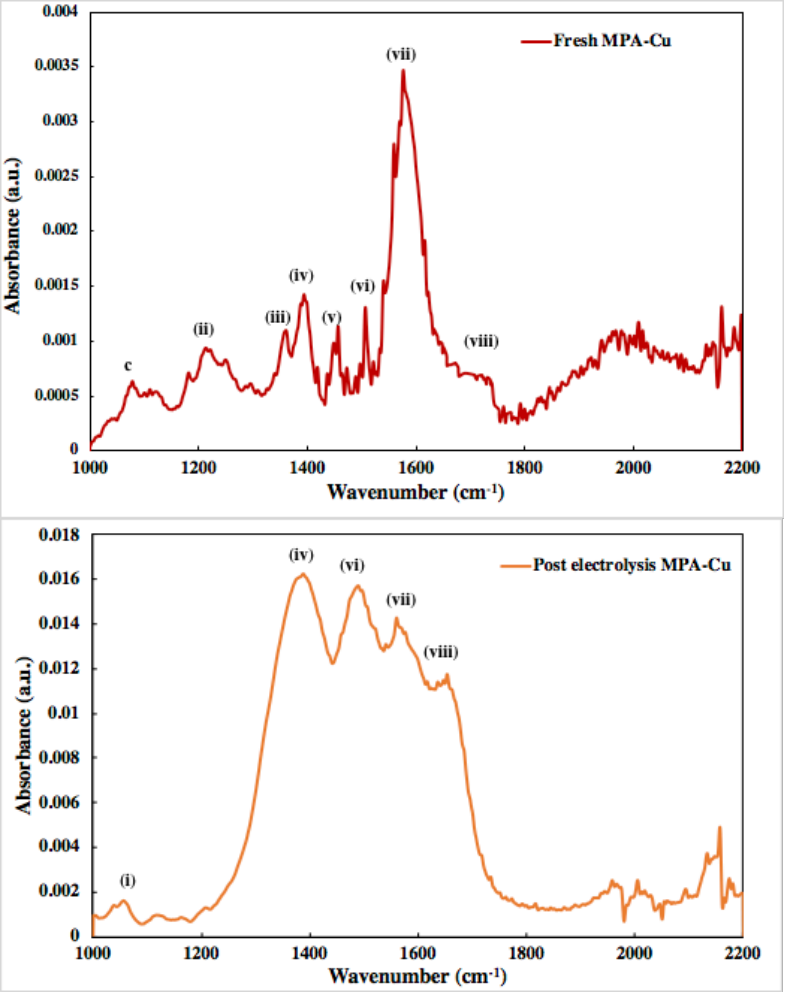

Figure 3.6. ATR-IR spectra for MPA-Cu before and after electrolysis.

Figure 3.6 shows the spectrum of MPA on Cu. There are significant differences between the spectra of before and after electrolysis sample. On the freshly prepared sample, peak (i) at 1086 cm^{-1} corresponds to the C-O stretching vibration in -COOH; peak (ii) at 1226 cm^{-1} corresponds to the skeleton C-C stretching vibration; peak (iii) at 1363 cm^{-1} and peak (v) at 1458 cm^{-1} correspond to the symmetric and asymmetric C-H deformation in $-CH_3$; peak (iv) at 1397 cm^{-1} corresponds to the symmetric stretching in $-COO^-$; peak (vi) and (vii) at 1508 cm^{-1} and 1578 cm^{-1} both corresponds the asymmetric stretching in $-COO^-$; and shoulder (viii) at 1737 cm^{-1} corresponds to the C=O stretching in -COOH.[66, 70] On the other hand, the spectra on the post electrolyzed sample showed distinct feature of vibration in $-COO^-$ group, with the diminish of feature in -COOH. Peak (i) appear to be less prominent, and peak (viii) shift to the left which is close to the asymmetric stretching of $-COO^-$. The variation in the spectra suggests that the monolayer will be dominant by the thiol with $-COO^-$ moiety instead of the -COOH. The losing of proton from ligand after electrolysis will be rationalized in the later chapters.

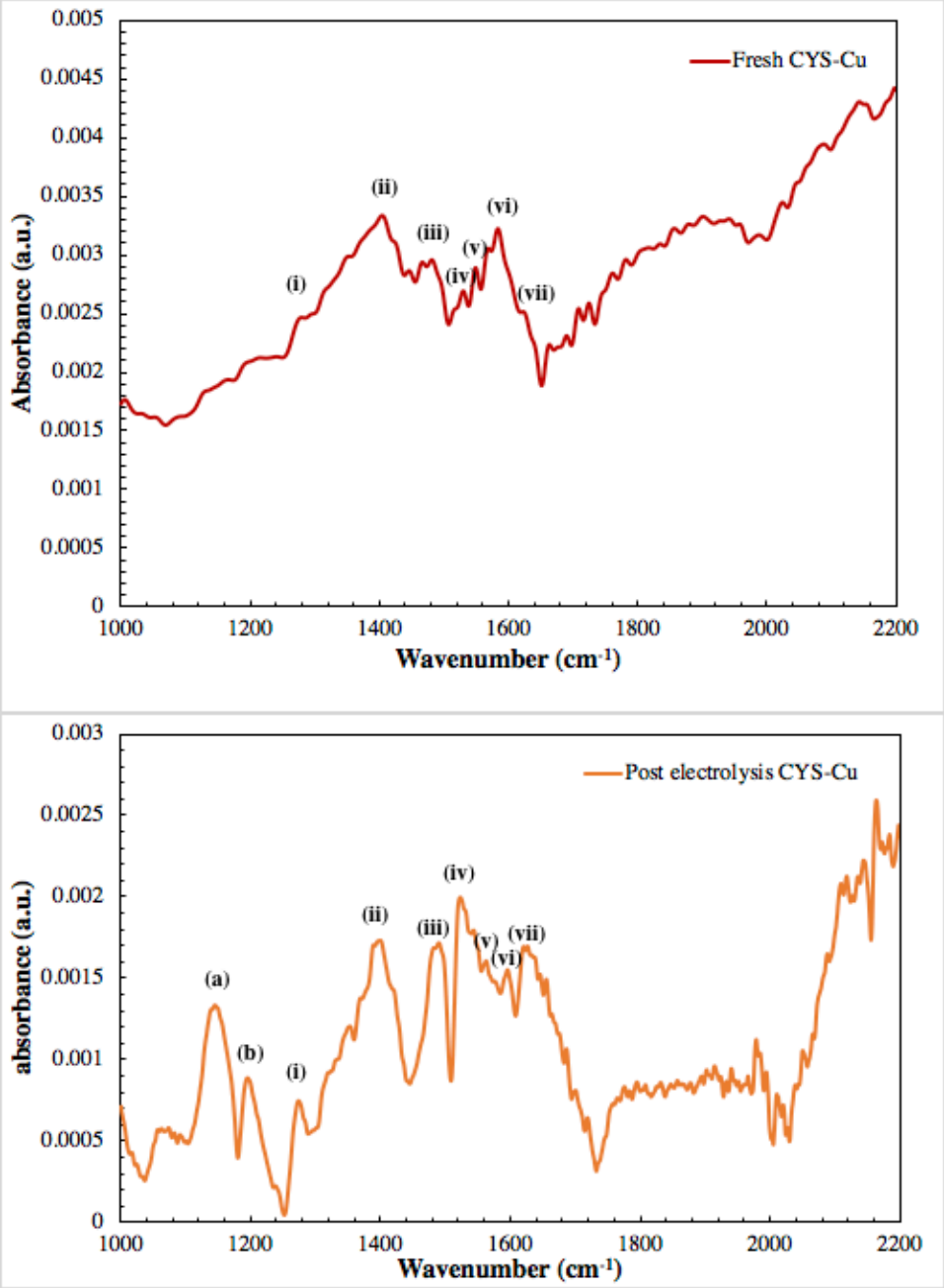

Figure 3.7. ATR-IR spectra for CYS-Cu before and after electrolysis.

In Figure 3.7 demonstrate the spectrum of CYS on Cu. The characteristic features of CYS are noticeable. On the freshly prepared sample, the absorbance peak (i) at 1270 cm^{-1} corresponds to the C-H wagging in -CH_2-S-; peak (ii) at 1410 cm^{-1} corresponds to C-H

deformation in -CH_2-S-; peak (iii) at 1483 cm^{-1} corresponds to C-H deformation in -CH_2-NH_2; peak (iv) at 1535 cm^{-1} and peak (vi) at 1575 cm^{-1} each corresponds to the symmetric and asymmetric N-H^+ stretching in -NH_3^+; peak (v) at 1551 cm^{-1} corresponds to N-H bending[71] in -NH_2 and peak (vii) at 1628 cm^{-1} is the N-H deformation vibration in -NH_2.[66] When compared with spectrum of freshly prepared sample, the post-electrolysis sample shows more apparent features (a, b iv and vi) of -NH_3^+. The present of NH_3^+ indicates that the CYS is involved in the proton transfer from electrolyte to either catalyst surface or CO_2 for reactions. Real mechanism remains to be discovered with isotope and spectroscopic experiments.

Conclusion

Au-Cu (50wt% Au) alloy was found to work as "super Au" for efficient CO evolution with up to 5 times increase in selectivity and 7 times higher production rates than parental pure element catalyst. This was attribute to the weak adsorption of CO on Au. However, further hydrogenation products are limited by the strong desorption effect from Au.

Ligand functionalization on Cu appears to be another effective strategy for catalyst design. Glutathione modified Cu give rise to significance in selectivity and production rate of CO. Over 100 mV anodic shift for CH_4 production on Cu was achieved at the presence of cysteamine. Though the mechanism of the enhanced catalytic performance remains unclear. The ligand functionalization shows great potential in breaking scaling relationship and effective engineering for selective catalyst.

CHAPTER 4. LIGAND RECONSTRUCTION ON AU ELECTRODE

Introduction

Au has been extensively studied as a cathode catalyst in multiple forms such as alloy, nanoparticles and oxide derived treatment. Herein two different thiol ligands on Au affecting the activity and selectivity of electrochemical CO_2RR are presented. Au electrodes modified with 2-phenylethanethiol ($C_6H_5(CH_2)_2SH$, abbreviated henceforth as 2-PET;) increased the FE and partial current density toward CO while suppressing the competing HER, whereas on Au electrodes modified with 2-mercaptopropanoic acid (or thiolactic acid, $CH_3CHSHCOOH$, abbreviated henceforth as 2-MPA;) HER achieved nearly 100% FE at the expense of CO_2RR, around -0.5 V_{RHE}. Furthermore, the total current density on 2-PET-Au was higher than on blank Au, while that on 2-MPA-Au was comparable to blank Au. Complementary Density functional theory (DFT) calculations suggest that certain thiolated Au defect sites created via thiol self-adsorption can promote CO_2 reduction in the potential range of study.

Experimental

Electrode preparation

Blank Au foil electrode (99.99%, MTI corp.) was rinsed with deionized water (Mega Pure system) and used as working electrode. Functionalized electrode was prepared as follows: The DI water-rinsed metal foils were immersed in a 20 mM ethanolic solution of 2-phenylethanethiol (Sigma-Aldrich, 98%) or 2-mercaptopropionic acid (Sigma-Aldrich, 95%) for 10 min. The thiol-functionalized electrodes were then rinsed with ethanol (Pharmco-

Credit for simulation part goes to Xun Cheng and Dr. Ye Xu.

Aaper, ACS) copiously after being taken out from the solution to remove non-chemisorbed species such as un-dissociated thiols. DI water rinse was followed the exclude the solvent adsorption.

Electrode Characterization

ATR-IR infrared spectra of functionalized gold electrodes were taken using a smart-ITR assembled Nicolet 6700 FTIR spectrometer with a nitrogen-cooled narrow-band MCT detector. Each (functionalized) Au sample was mounted on the sampling stage where the diamond crystal was located at the center, and the sample was then fixed with the high-pressure clamp from the top. For both ligand-modified electrodes, one spectrum was taken on the fresh prepared electrode. The electrodes then underwent chronoamperometry in the same two-compartment electrochemical cell at various controlled potentials until -1.1 V_{RHE}, which was the most negative potential applied in the product analysis. Spectra were taken after each potential was held for 15 min for 2-PET-Au and 30 min for 2-MPA-Au. The spectra were recorded at a resolution of 0.5 cm^{-1} and 256 scans.

The thiol coverage measurements with linear sweep voltammetry[72] were conducted in a one compartment 3-electrode cell. Freshly prepared and post-reaction samples served as working electrode with Pt wire as the counter electrode, the potentials was measured with respect to Ag/AgCl (saturated with 3M NaCl) reference electrode (BASi, RE-5B) by VSTAT 3 potentiostat. The potential sweeped from 0 to -1.5 V at a scan rate of 50 mV/s in 0.5 M KOH and 0.1 M KOH for 2-PET-Au and 2-MPA-Au, respectively. Note, the reason to use 0.5 M KOH for 2-PET-Au is that reductive desorption peak in 0.1 M KOH was indiscernible. The molecule coverages were reported in mol/cm^2 based on faraday's law of electrolysis.

Electrochemical Catalysis.

Electrochemical experiments were carried out using a three-electrode cell in a two-compartment glass reactor separated by Nafion membrane (FuelCellsEtc) to prevent the product from being re-oxidized. The potential of the cathode was measured with respect to an Ag/AgCl (saturated with 3M NaCl) reference electrode by a model 263A potentiostat/galvanostat. The Pt wire in the anode compartment served as counter electrode. All measured potentials (uncompensated resistance corrected) were converted to the Reversible Hydrogen Electrode scale (RHE). The current density was normalized by the geometric area of the gold electrode surface.

The cyclic voltammetry was performed under the same condition with the scanning rate at 10 mV/s from 0.2 V to -2.0 V vs. Ag/AgCl. 0.1 M $KHCO_3$ (Sigma-Aldrich, ACS reagent) in Mega-Pure water was used as supporting electrolyte. The solution was bubbled with N_2 (Air Liquide, UHP) for 30 min to produce a purged solution of pH 9 for HER studies. For the CO_2 (Air Liquide, 99.99%) reduction reaction, it was bubbled with CO_2 for 30 min producing a saturated solution with pH 6.8. For the product analysis, CO_2 was bubbled continuously into the electrochemical cell at a flow rate of 40 ml/min and a pressure of 1 atm while potentials were applied by stepping to desired potential and held for 15 min. The gas products (CO and H_2) in the effluent from the electrolysis were auto-sampled after 15 min system stabilization to the gas chromatograph (SHIMADZ, GC 2014) with HP-Plot U column (Agilent Technologies, Inc.) that equipped with FID and TCD detectors, and the concentrations of individual gases were analyzed with the calibration curve.

Result and Discussion

Electrochemical measurements.

We determined the onset potentials for CO_2RR and HER based on Tafel plots[73] The onset potentials are summarized in Table 4.1, while Figure 4.1 compares the FE and partial current density for CO and H_2 on blank Au, 2-PET-Au, and 2-MPA-Au. The only detected major gas products from the on all the Au electrodes were H_2 and CO. The onset of CO evolution at ca. -0.3 vs. RHE on polycrystalline Au is consistent with previous reports[20] and has been conclusively proven by Dunwell et al. recently with surface enhanced infrared absorption spectroscopy, which captured the vibrational signature of CO on Au under a square-wave potential profile. The onset potential for CO2 reduction on both of the functionalized Au electrodes (2-PET-Au and 2-MPA-Au) was increased to -0.24 vs. RHE, which is a 90 mV improvement (anodic shift) compared to the blank Au foil. For HER, the onset potential on 2-PET-Au barely changed, while a 160 mV anodic shift was observed on 2-MPA-Au.

Table 4.1. Comparison of onset potentials (vs. RHE) of HER and CO_2RR on blank and functionalized Au foil electrodes at room temperature

Electrode	HER	CO_2RR
Au foil	-0.27	-0.33
2-PET-Au	-0.26	-0.24
2-MPA-Au	-0.11	-0.24

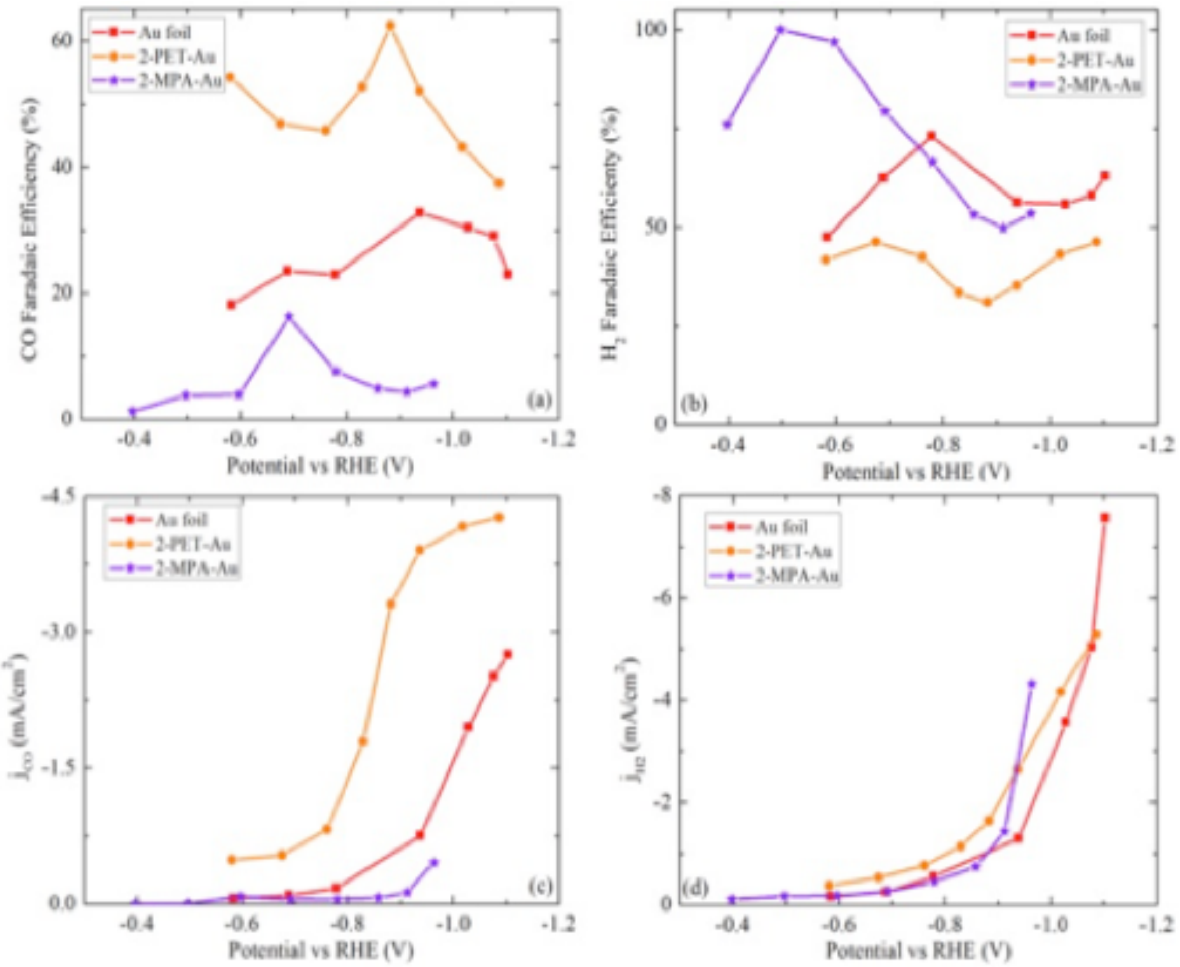

Figure 4.1. Comparison of electrolytic behavior between blank and functionalized Au foil electrodes at room temperature and pCO2 = 1 atm showing the altered catalytic behavior of Au in the presence of thiol ligands. (a) Faradaic efficiency of CO; (b) Faradaic efficiency of H_2; (c) partial current density of CO (j_{CO}); (d) partial current density of H_2 (j_{H_2}).

Figure 4.1 compares the catalytic performance of ligand functionalized Au with Au foil. At the presence of 2-PET on Au, the FE of CO was doubled while the FE for H_2 was suppressed by half. The partial current densities for both products increased, the one for CO was enhanced in a remarkable way. At -0.8 V_{RHE}, the FE for CO evolution on 2-PET-Au was twice that on blank Au, and the current density for CO on 2-PET-Au was 7.6 times that on blank Au foil.

2-MPA-Au exhibited the opposite effects on product selectivity: The FE for CO evolution was suppressed while the FE for H_2 was promoted to near unity at low overpotentials. The partial current density for CO was lower than on blank Au, while that for H_2 was comparable to blank Au foil. But the performance resembles to Au foil at more cathodic potential than -0.9V, this is speculated to be resulted for the desorption of thiol from Au surface.

Stability of thiols on Au.

Ex situ ATR-IR and desorption voltammetry experiments were used to explore the stability of 2-PET and 2-MPA on Au, before and after they are subject to the same CO_2 electrolysis experiments.

The ATR-IR spectra are presented in Figure 4.2. On 2-PET-Au, the CH_2 wagging vibration in $–CH_2$-S- at 1260 cm^{-1} (i), $-CH_2-CH_2-$ bending at 1380 cm^{-1} (ii), the $–CH_2-$ asymmetric stretching at 2947 cm^{-1} (v) and the aromatic ring C=C stretching at 1580 cm^{-1} (iii) and 1623 cm^{-1} (iv) appeared for the electrode both as prepared and 15 min post electrolysis at -1.1 V vs. RHE (peak assignments as indicated in Figure 4.3(a)).[66, 68-69] The overall intensities of the signals are similar. The blue shift of peak i to higher wavenumber (corresponding to higher energy) can be attributed to the fraction of gauche defect.[74] In presence of gauche conformation, the phenyl ring will be in close contact with the surface. This deformation is also supported by the simulation results. The relative intensity between $-CH_2-CH_2-$ bending (ii) and aromatic ring C=C stretching (iii &iv) can be expected under the deformation of structure.

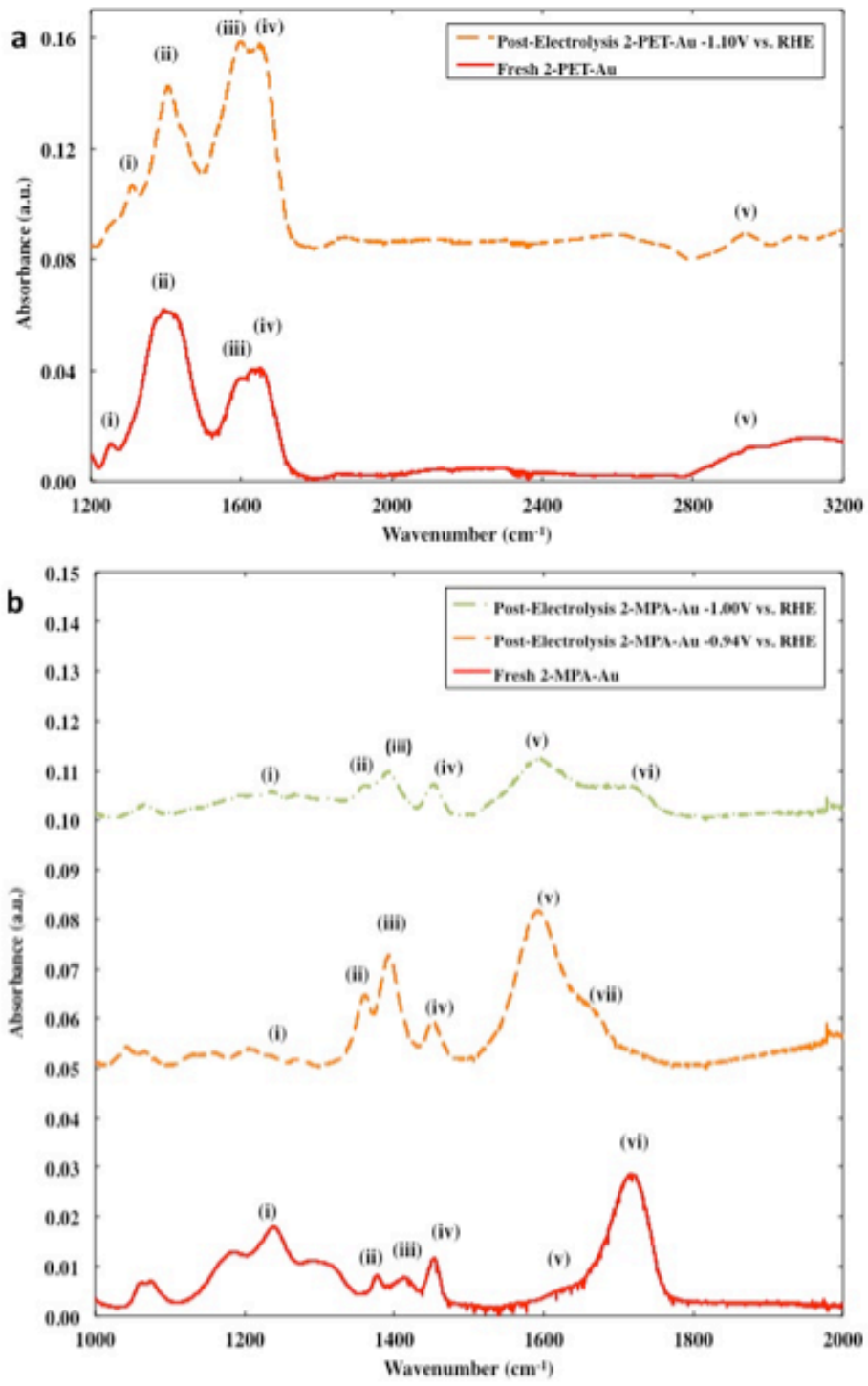

Figure 4.2. ATR-IR spectra for as-prepared and electrochemically reduced. (a) 2-PET-Au and (b) 2-MPA-Au.

In the spectrum of the as-prepared 2-MPA-Au electrode (peak assignments as in Figure 4.3(b)), the peak at 1723 cm^{-1} (vi) was assigned to the C=O stretching of the COOH group, whereas the weak shoulders at 1602 cm^{-1} (v) and 1421 cm^{-1} (iii) were assigned to the asymmetric and symmetric stretching of $–COO^-$, respectively.[75-76] The peaks at 1372 cm^{-1} (ii) and 1449 cm^{-1} (iv) were assigned to the symmetric and asymmetric stretching of the $-CH_3$ group, and 1241 cm^{-1} (i) to the C-C stretching.[66] Comparison with reported literature excluded the possibility that these absorption peaks are due to $KHCO_3$.[77] After 30 min of CO_2 electrolysis at -0.94 V vs. RHE, the rise of peaks (iii) and (v), and diminishment of peak (vi) indicate that the dominant species on the surface is the deprotonated form of 2-MPA. The conclusion regarding the deprotonation of the COOH group is based on the findings of surface science studies of carboxylic acids interacting with metals as well as oxides in the literature.[75, 78-80] However, after 30 min of electrolysis at -1.00 V vs. RHE, the intensity of most of the bands decreased significantly. This indicates notable loss of the ligand molecules between -0.94 and -1.00 V vs. RHE.

Figure 4.3 shows the complimentary voltammetry experiment for stability analysis. Figure 4.3(a) shows the voltammogram of 2-PET on Au in 0.5 M KOH aqueous electrolyte. The difference in background current might arise from non-faradaic capacitive charging. The reductive peak at -1.06 V vs. Ag/AgCl, is integrated to give a reductive charge of 116 $\mu C/cm^2$ for the freshly prepared 2-PET-Au, which corresponds to a coverage of 1.2×10^{-9} mol/cm^2 (summarized in Table 2) based on Faraday's law of electrolysis. This value is close to those reported in previous literature.[72] 89 $\mu C/cm^2$ was obtained by integrating the reductive peak for post-electrolysis 2-PET-Au, corresponding to 9.26×10^{-10} mol/cm^2, which indicates that 77% of 2-PET remained on Au surface following CO_2 electrolysis.

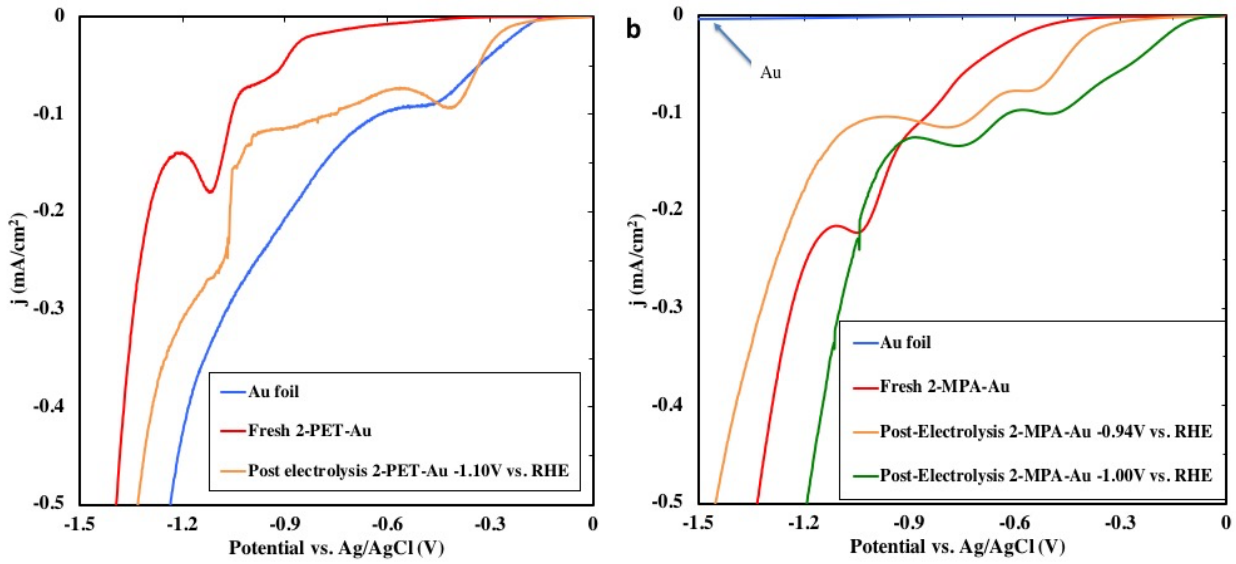

Figure 4.3. Linear voltammograms of (a) 2-PET and (b) 2-MPA on Au foil electrodes at room temperature. Scan rate was 50 mV/s.

Figure 4.3b shows the corresponding voltammogram of 2-MPA on Au in 0.1 M KOH. The integrated reductive charges were 95 μC/cm^2, 89 μC/cm^2, and 63 μC/cm^2 for freshly prepared 2-MPA-Au, Post electrolysis 2-MPA-Au (-0.94 and -1.00 vs. Ag/AgCl), respectively. This indicates that 2-MPA loss becomes significant below -0.94 vs. Ag/AgCl. These results further prove the stability of the ligand, though the 2-PET appear to be more stable than 2-MPA. Note, the ex situ experiments limited the elucidate conclusion on ligand during reaction, ie. the ligand could have dethiolate during the reaction but adsorbed back post reaction due to their hydrophobic characteristic. 2-PET is known to be more hydrophobic than 2-MPA.

Table 4.2. Reductive charge and coverages of 2-PET and 2-MPA on Au electrodes estimated from linear voltammetry.

Ligand	Sample	Reductive Charge ($\mu C/cm^2$)	Coverage (mol/cm^2)	Percent remain (%)
2-PET	Fresh	116	1.2×10^{-9}	100
	-1.10 V_{RHE}	89	9.26×10^{-10}	77
2-MPA	Fresh	95	9.85×10^{-10}	100
	-0.94 V_{RHE}	89	9.21×10^{-10}	94
	-1.00 V_{RHE}	63	6.56×10^{-10}	72

Reconstruction mechanism

The two ligands included in this study, 2-PET and 2-MPA, belong to a large class of organothiol compounds, including alkanethiols and arenethiols, which are known for their tendency to self-assemble into stable monolayers ("SAM") on Au and other metals and have been used to functionalize the surfaces with different chemical groups.[81-84] The anodic shift at the presence of ligand suggest the promoted thermodynamics which further indicates the presence of more catalytic-active sites than blank foil. Previous literature has proposed that the fully ligand protected Au nanocluster is not an active CO_2 reduction catalyst and the active sites are the singly dethiolated sites[85] Therefore, a possible mechanism behind our observation of enhanced CO_2 reduction activity is the presence thiol is able to create active sites through dethiolation. The ex situ stability evidences suggest that this step is a

continuing process since the ligand never really permanently leave the surface. That is to say, the presence of thiol induced the surface reconstruction and resulted in sites that altered the catalysis.

Ample scanning tunneling microscopy (STM) studies in the literature have reported that the morphology of Au surfaces can undergo significant changes with the adsorption of thiols.[86-93] At low coverages, thiol adsorption lifts the $(23\times\sqrt{3})$ "herringbone" reconstruction of the Au(111) surface[94-96] and restores the bulk (1×1) structure, which implies that the extra Au atoms embedded in the herringbone structure are released.[88, 90, 92, 97-101] At sufficiently high coverages, thiol adsorption induces pitting and vacancy formation on Au(111) together with formation of new islands, while Au step edges take on a characteristic "saw-tooth" appearance, on a time scale of minutes.[86, 88, 92, 98, 100, 102-103] The reconstruction is most likely accomplished via extraction of Au atoms by thiolates. It has been discovered that self-assembled monolayers of thiols on Au contain Au adatoms.[102-104] The "staple" motif (with a chemical formula of R-S-Au-S-R, i.e., dithiolate-Au complexes) has been suggested by various experiments to form at ambient or sub-ambient temperature upon thiol adsorption on Au.[103, 105-106] The higher stability of the dithiolate-Au complexes than directly adsorbed thiolates on Au(111) has been shown for representative species such as methylthiol using DFT calculations.[107-108]

In our case, the reconstruction process would begin prior to the electrochemical experiments, starting with the submersion of an Au foil in an ethanolic thiol solution and continuing as the Au foil was dried and later placed in thiol-less CO_2 electrolysis solutions, thereby generating new sites. A likely process is illustrated in Figure 4.1. It begins with a ligand-covered Au(111) surface as may result from the deposition of appropriate precursors,

and proceeds with a thiolate molecule extracting an Au atom out of Au(111) forming an intermediate state such as a monothiolate-Au complex and leaving behind a Au vacancy. As this process repeats itself, extended vacancy clusters are created with new defect sites, and a steady supply of monothiolate-Au complexes is generated that coalesce into either new step edges or dithiolate-Au complexes. Existing and newly created defect sites are expected to be occupied by thiolate species to the extent that the pre-existing surface coverage of thiolates permits (since no additional thiol is available once the Au foil is taken out of the thiol solution).

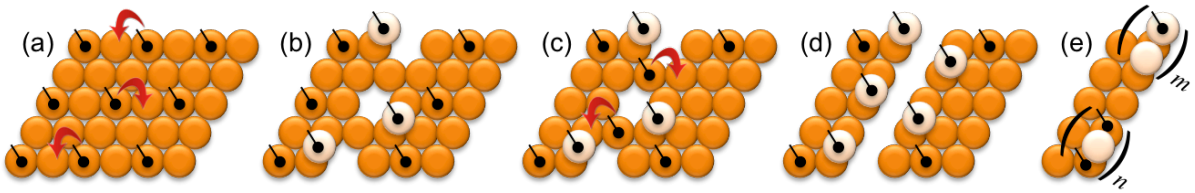

Figure 4.4. Schematic illustration of the proposed reconstruction process on Au(111). (a) thiolates cover Au(111); (b) thiolates create isolated vacancy defects by extracting Au atoms out of the surface; (c) additional thiolates diffuse over and extract more Au atoms; (d) a new monatomic step lined with monothiolate-Au complexes is formed; (e) monothiolate-Au complexes condenses into domains of thiolated edges (indicated by *m* repeating units) and of dithiolate-Au complexes (the "staple" motif) adsorbed on edges (indicated by *n* repeating units). Large spheres represent Au atoms (different shading denotes different layers); black dots with tails denote ligands.

DFT simulation was used to clarify the ligand effect on Au for the observed activity change in CO_2 reduction. Au(111), (100), (211), and (563) facets to represent Au sites of different morphologies (hexagonal close-packed and square close-packed terraces, step edges, and corners, respectively), which have different coordination numbers (9, 8, 7, and 6, respectively).[109] We consider the following steps as representing the main steps in CO_2 reduction (Steps 1, 2, and 3) and H_2 evolution (Step 4):[52, 110]

$$CO_{2(g)} + H^{+}_{(aq)} + e^{-} + * \rightarrow COOH^{*} \quad (1)$$

$$COOH^{*} + H^{+}_{(aq)} + e^{-} \rightarrow CO^{*} + H_2O_{(aq)} \quad (2)$$

$$CO^{*} \leftrightarrow CO_{(g)} + * \quad (3)$$

$$H^{+}_{(aq)} + e^{-} + * \rightarrow H^{*} \quad (4)$$

The reaction mechanism can alternatively be written by replacing H^{+}(aq) with $H_2O - OH^{-}$(aq),[111] but the results are the same on the RHE. The equilibrium potential for Step 4 is taken to be the limiting potential for H_2 evolution, whereas the more negative of the potentials for Steps 1 and 2 is taken to be the limiting potential for CO_2 reduction. We find that the limiting potential for Step 1 is negative while that of Step 2 positive on all four surfaces. Kinetically we assume that the transfer of a proton/electron to an oxygen atom occurs with a small barrier,[112-113] which applies to both Steps 1 and 2. Furthermore, we have calculated that the addition of a proton/electron to COOH adsorbed on Au results in the formation and spontaneous detachment of a water molecule, while CO desorption (Step 3) from bulk Au is not expected to be rate-determining because experimentally CO desorption from Au is complete below 300 K except for very small Au particles.[114-115] Thus the thermodynamic barrier represented by the more negative of the equilibrium potentials for Steps 1 and 2 is the controlling factor in the activity of CO_2 reduction on Au.

Table 4.3 listed the limiting potentials for HER and CO_2 RR on different site. The difference in the overpotential for CO_2RR vs. HER narrows as the coordination of the Au site decreases, although HER is more active than CO_2RR on all of the blank Au sites considered here. This pattern is qualitatively the same as the observed anodic shifts of the HER and CO_2RR onset potentials on the functionalized vs. blank Au electrodes.

Table 4.3. Calculated limiting potentials for HER and CO_2RR and their differences (vs. RHE) on various blank Au sites.

	HER	CO_2RR	difference
Au(111)	-0.34	-0.66	-0.32
Au(100)	-0.35	-0.63	-0.28
Au(211)	-0.22	-0.35	-0.13
Au(563)	-0.23	-0.26	-0.03

The adsorption energies for thiols were calculated and summarized in table 4.4. As was expected the thiolates prefer binding to defect sites over terrace sites just like typical adsorbates. Therefore, adsorption of the thiolate species and the reaction intermediates was considered on the edge of Au(211) only.

Table 4.4. DFT-calculated adsorption energies (ΔE_{ads}, eV) and dipole moments (μ_0,eÅ) for thiols

Species		ΔE_{ads}	μ_0
$C_6H_5(CH_2)_2S$	Au(111)	-1.38	-0.18
	Au(211)	-1.92	-0.29
$CH_3CHSCOOH$	Au(111)	-1.35	-0.02
	Au(211)	-1.79	+0.43

We have also examined the projected local density of states (see Figure 4.5) for an edge site on blank Au(211) and for the open edge site on $(2\text{-PETt})_2Au/Au$ and $(2\text{-MPAt})_2Au/Au$. The Au sites show very similar electronic structures. The center of the projected Au d-band is downshifted slightly for both of the thiolated sites compared to blank

Au(211), which is consistent with S-Au interaction, which destabilizes COOH and H intermediates adsorbed on the neighboring site as expected.

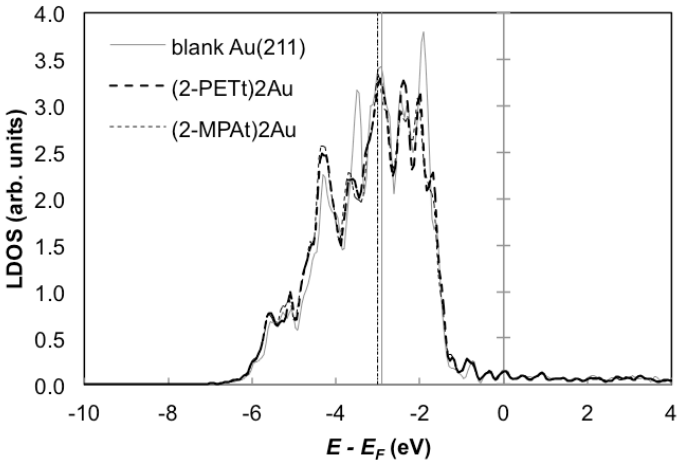

Figure 4.5. Local density of d states (LDOS) projected onto an open edge site on blank and thiolated Au(211). E_F denotes the Fermi level. The center of the Au d band at each site is indicated by a vertical line (blank Au(211): -2.91 eV; $(2\text{-PETt})_2$Au on Au(211): -3.01 eV; $(2\text{-MPAt})_2$Au on Au(211): -3.01 eV).

On the other hand, the 2-PET thiolate species (both the directly adsorbed thiolate and the dithiolate-Au complex) induce a more negative dipole moment than the 2-MPA thiolate species. This is due to the fact that, while there is a small net charge transfer to the thiolates according to Bader analysis[116], the carboxylate group in 2-MPA is better than 2-PET at redistributing charge density away from the surface when adsorbed on Au as is shown in figure 4.6. Since a negative dipole moment interacts unfavorably with a negative interfacial electric field, and since the negative dipole moment is counteracted by COOH but not by atomic H because the latter has a nearly zero dipole moment, 2-PET thiolate species effectively create a local electrostatic environment that is more favorable to COOH adsorption than H adsorption. This effect is much less pronounced for the 2-MPA counterparts. A more favorable local electrostatic environment partially explains the

improved selectivity to CO_2RR on 2-PET-Au vs. 2-MPA-Au. However, it does not explain the improved selectivity to CO_2RR on 2-PET-Au vs. blank Au, which, we hypothesize, is due to additional interfacial effects. For instance, the carboxylate group in 2-MPA may have proton conduction properties similar to Nafion that enhance proton concentrations near the electrode, whereas the hydrophobicity of the phenyl group in 2-PET would lower local proton concentrations instead. The interfacial proton activity would further modulate the selectivity of the electrochemical reactions[14, 117-118] in addition to the effects that we have directly modeled using DFT.

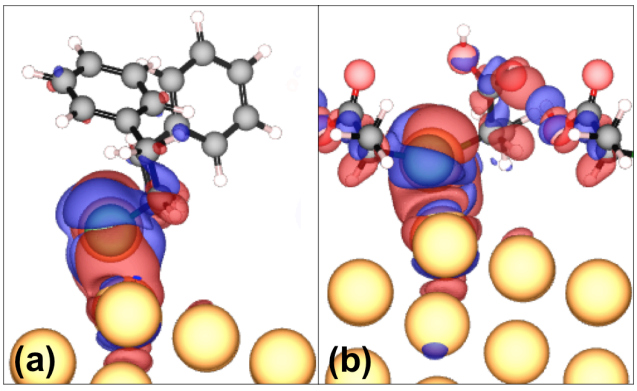

Figure 4.6. Charge density difference ($\Delta\rho = \rho_{total} - \rho_{surface} - \rho_{mol1} - \rho_{mol2}$) . for (a) (2-PETt)$_2$/Au(211) and (b) (2-MPAt)$_2$/Au(211) (on (4×3) surface unit cells) as viewed down the step edge. The Au adatom is taken to be part of the surface, and the two thiolates are treated as individual molecules. The contours depicted are +0.001 (density increase, red) and -0.001 (density depletion, blue) e/Å^3, respectively. The maximum range of change is +0.028 ~ -0.056 e/Å^3 for (2-PETt)$_2$/Au(211) and +0.035 ~ -0.056 e/Å^3 for (2-MPAt)$_2$/Au(211). The surface dipole moment (μ_0) is -0.45 eÅ for (a) and -0.10 eÅ for (b). Gold, green, red, black, and white spheres represent Au, S, O, C, and H atoms, respectively.

Computationally, attempts to reduce the magnitude of the dipole moment of the 2-PET thiolate species raised the total energy of the system concomitantly and did not lower the free energy of the system. The effect of solvent on the interfacial dipole moment is not

captured by the current vacuum models, but we expect the difference between 2-PET and 2-MPA to persist due to the intrinsic nonpolar, hydrophobic nature of the phenyl group vs. the polar, hydrophilic nature of the carboxylate group, and due to the high dielectric constant of water.

The activity of various Au sites toward CO_2RR thus follows this order: blank defect sites (~ -0.3 V_{RHE}) > blank terrace sites (~ -0.6 V_{RHE}). While thiolate-induced surface reconstruction may have a limited impact on the *onset for CO_2RR on Au*, the newly formed defect sites, though less active than blank defect sites, are more active than the original blank terrace sites, which means an effective increase in the surface density of moderately active sites. This is consistent with the observation that *the total current density was not reduced compared to blank Au by thiol adsorption* at -0.6 V_{RHE} and below. The fact that the total current density followed the order of 2-PET-Au > 2-MPA-Au ~ blank Au may be due to either the adsorption of more 2-PET than 2-MPA in the thiol solution treatment, or different ability of 2-PET and 2-MPA thiolates to reconstruct Au, or both.

Conclusion

In this work, we demonstrated that surface-adsorbed thiolate ligands, introduced by pretreating polycrystalline Au electrodes in ethanolic solutions of thiols, thereby the activity and selectivity of electrochemical CO_2 reduction will be altered. A 2-fold enhancement in Faradaic efficiency and more than 7-fold increase in current density for CO evolution accompanied by the suppression of the competing H_2 evolution reaction were observed on Au electrodes functionalized with 2-phenylethanethiol (2-PET). On the other hand, functionalization with 2-mercaptopropionic acid (2-MPA) strongly favored H_2 evolution over CO evolution. Thiolate-induced surface reconstruction was proposed to be the key in

the modified behavior of the functionalized Au electrodes. Based on DFT calculations .certain thiolated structures, such as dithiolate-Au complexes, which are readily formed in surface reconstruction, were proposed to have a milder impact on the catalytic activity of nearby sites than directly adsorbed thiolates at comparable coverage, and depending on the thiol species, they may in fact allow CO_2RR to turn up at lower overpotentials than blank Au terraces do, so as current density following Bulter-Volmer's law in the intermediate potential range (ca. -0.6 ~ -1.0 V vs. RHE), as observed in our experiment. The ligands essentially play the role of creating new local environments on an Au electrode that are geometrically and electrostatically favorable to reactions such as CO_2RR or HER. Our study thus demonstrates that ligand chemistry can be another axis in modifying the activity and selectivity of Au for different electrode reactions.

CHAPTER 5. LIGAND FACILITATED PROTON-COUPLED ELECTRON TRANSFER ON AU ELECTRODE

Introduction

As was discussed in previous chapter, pretreating Au surface with thiols has shown its capability in surface reconstruction to alter the catalytic activity in CO_2 reduction reaction. Engineering metal catalyst with ligand appear to be an effective method to control the product selectivity. In this chapter, we will discuss another aspect of ligand effect in which ligand play important role in promoting the selectivity toward hydrogenated species.

Several literatures have reported the enhanced hydrogenated species production with organic additives into the catalyst system. Bocarsly et al. showed Faradaic efficiencies up to 30% for CH_3OH at 40 $\mu A/cm^2$ on Pd/Pt using 10mM pyridine additives to the electrolyte.[57] The pyridinium ($pyrH^+$) was proposed as the active homogenous catalysts until later studies suggested that the pyridinium radical ($pyrH^*$) functioned as one-electron charge-transfer mediator for the production of methanol at the electrode surface.[119-120] Further pyridine substituted groups yielded up to 30% Faradaic efficiency to CH_3OH production; however, these results were generated at relatively low current densities (~50 $\mu A/cm^2$). [121] Likewise Dyer et al. studied the use of pterins, namely mercaptopteridine (PTE) as molecular catalysts in 0.1 M KCl at glassy carbon electrodes that yielded 10~24% CH_3OH at 100 $\mu A/cm^2$ which was similarly attributed to the electron transfer ability of pterin.[122] The mechanism behind the enhanced hydrogenated species production is still under debate.

In this chapter, we used monolayers of thiol-tethered functional ligands with different pKa (which represent their proton donating ability) on Au electrodes to look into the ligands' capability in surface hydrogenation in CO_2 reduction. Three ligands: 2-mercaptopropionic acid (MPA, pKa=3.7), cystemine (CYS, pKa=9.25) and 4-pyridylethylmercaptan (4-PEM, pKa=5.2) were investigated. The gas and liquid products at the surface modified electrodes are analyzed as well as the stability of the ligand-modified modified surfaces.

Experimental

Electrode preparation

Au foil electrodes (99.99%, ESPI) were rinsed with deionized water (MegaPure system) and used as working electrode. The functionalized electrodes were prepared as follows: Au metal foils were rinsed in deionized (DI) water followed by the solvent of ligands copiously before immersion into the 20 mM of 2-mercaptopropionic acid (Sigma-Aldrich, 95%) ethanolic (Pharmco-Aaper, ACS) solution, 20 mM of cysteamine (Sigma-Aldrich 95%) aqueous solution and 20 mM of 4-pyridylethylmercaptan (AldrichCPR) methanolic (EMDTM, ACS) solution for 10 min, 10 min and 5 min, respectively. Previous studies have shown short immersion times are sufficient for the chemical adsorption of thiolate at μM thiol solution to reach a packing density at 4.47*10-10 mol/cm^2.[123-124] The formation of thiol layer takes less time at higher concentration solution.[125] A well ordered pyridinylthiol monolayer on Au was studied after 5 min immersion.[126-127] The thiolate-modified electrodes were then rinsed with solvent of the solution followed by DI water to remove the non-chemisorbed thiol and solvent molecule. A fresh electrode was prepared at each potential to ensure the consistency of the experiments.

Electrochemical Methods

Electrochemical experiments were carried out using a H-type electrochemical cell separated by Nafion membrane (FuelCellsEtc) which is to prevent the CO_2 reduction product from being reoxidized. The (functionalized) Au foil served as the cathode, while the Pt wire served as the auxiliary electrode. The potential was measured with respect to an Ag/AgCl (saturated with 3 M NaCl) reference electrode (BASi, RE-5B) by a PAR model 263A potentiostat/galvanostat followed by the manual correction of uncompensated resistance. The potentials in this study were reported versus RHE with the conversion E(vs. RHE)= E(vs. Ag/AgCl)+0.197+0.059*pH. The current density was obtained by normalized with the Au geometric surface area.

Cyclic voltammetry (CV) was performed with the scanning rate at 10 mV/s from 0.2V to -2.0V vs. Ag/AgCl in 0.1M $KHCO_3$ (Sigma-Aldrich, ACS reagent) as supporting electrolyte. The solution was bubbled with N_2 (Air Liquide, UHP) for 30 min to produce a purged solution of pH 9 for HER reaction studies. For the CO_2 (Air Liquide, 99.99%) reduction reaction, it was purged with N_2 for 20 min to remove O_2, and then CO_2 was bubbled into the solution for 30 minutes producing a saturated solution with pH 6.8. The onset potentials for HER and CO_2 RR were determined from Tafel plots of CVs in N_2 saturated electrolyte and CO_2 saturated electrolyte, respectively.[128] [73]

For the gaseous product analyses, CO_2 was bubbled continuously into the electrochemical cell at a flow rate of 40 ml/min and a pressure of 1 atm, while potentials were applied by stepping to desired potential and held for 15 min. At the 15 min interval, the gas products (CO and H_2) in the effluent from the electrolysis were auto-sampled to the gas chromatograph (SHIMADZU, GC 2014) that equipped with FID and TCD detectors. The

concentrations of individual gases were analyzed to give the production rate (expressed in partial current density, ji) and Faradaic selectivity.

The liquid products were analyzed with Nuclear Magnetic Resonance (NMR). NMR has been a preeminent technique to determine the structure of organic compounds. In a common NMR spectroscopy, the radio frequency radiation will be casted on the compound confined in a 5mm tube which is placed in a strong external magnetic field. With the external excitation, the nucleus at lower energy state will be excited to higher energy state. The falling back from high energy state to ground zero state results in the emission of energy which is measured by the receiver to determine the bonding information. A calibration curve was also pre made for quantitative analysis of individual component in the electrolyte solution.

The liquid products analyses on the 30 min bulk electrolysis electrolyte were carried out with an VNMS 700 spectrometer with an excitation sculpting pulse technique for water suppression as described by Jaramillo et al.[29] 10 mM DMSO was used as the reference peak. The 1D 1H NMR data were processed with MestReNova. Considering the alcoholic thiol solution used here may result in false reading in higher hydrocarbon product, formate is the only liquid product discussed here.

Surface Self-Assembled Monolayer (SAM) Characterization

The surfaces were characterized with atomic force microscopy (AFM). AFM is a high resoluction scanning probe microscopy which employs a cantilever tip for mechanic interaction with surface when traveling on the surface. The changing surface condition will induce instantaneous deflection on the cantilever that is magnified by the laser detection.

The surface roughness was measured on surfaces that was freshly prepared. Characterizations were carried out with an Agilent 5500AFM/SPM scanning probe

microscope system. Oxide-sharpened silicon nitride probes (kavg=0.5 N/m) was used at contact mode from Veeco Probes for imaging. The surface roughness are reported with Picoscan v 5.3.3 software analysis.

ATR-IR infrared spectra were measured on a smart-ITR diamond assembled Nicolet 6700 FTIR spectrometer with a nitrogen-cooled narrow-band MCT detector. Spectra were recorded for the fresh prepared electrode before any electro-reduction. The same chronoampermetry experiments for NMR electrolysis were then performed in the same two-compartment electrochemical cell at various controlled potentials till -1.1V vs. RHE where the highest overpotential applied for the product analysis. Spectra were taken after each potential step. Interferograms were recorded at a resolution of 0.5 cm^{-1} and 256 scans. Comparison with previous reported literature excluded the possibility that the absorption peaks are from the potassium bicarbonate. [77]

Results and Discussion

Product Analysis

Figure 5.1 shows the potential dependent product distribution (expressed in Faradaic efficiency for selectivity and partial current density for yield of each compound) from CO_2 reduction on functionalized-Au and untreated Au surfaces. The primary products including formate, CO and H_2 were characterized by NMR and GC analysis. Their potential dependent yield behavior and Faradaic efficiencies are discussed in the following sections.

Relative to untreated Au foil, MPA modified Au electrodes produced hydrogen as a primary product (Faradaic efficiency near 100%) in the low overpotential range (>-0.8V vs. RHE) while CO evolution was suppressed. The greatest observed Faradaic efficiency for CO evolution is less than 20% which is roughly half of that on untreated Au. Likewise, the

formate production is reduced by approximately half when MPA is tethered to the electrode. The potential range investigated using MPA modified Au was limited to less than -0.94 V vs. RHE, likely due to desorption of surface ligands at high overpotentials which is discussed later.

Remarkably, the 4-PEM modified electrodes produced approximately 3 times more formate (-4.1 mA/cm^2) relative to the optimal observed on Au foil (-1.37 mA/cm^2). In terms of the Faradaic efficiency for the reduction to formate, a maxima of 21% with Au/4-PEM electrode (at -1.00V vs. RHE) was achieved compared with 11% on Au surfaces (at -1.01V vs. RHE). On the other hand, the CO partial current was suppressed on the same electrode by at least half relative to Au over the entire potential range of interest. It is interesting to note that the 4-PEM modified Au shows selectivity toward the HER at low potentials (-0.5 to -0.7V vs. RHE), then CO_2 reduction increases in the potential range from -0.7 to -1.1V vs. RHE. Electrolysis in N_2 saturated electrolyte experiments were employed to rule out the possibility of thiolate decomposition into formate.

As for the CYS-functionalized Au electrode, formate production was suppressed relative to Au within the entire potential range of interest. Although the selectivities of CO and H_2 were similar to Au foil, the electrode was significantly more active (i.e. the partial current density j_{CO} and j_{H2} were increased by more than 2 folds).

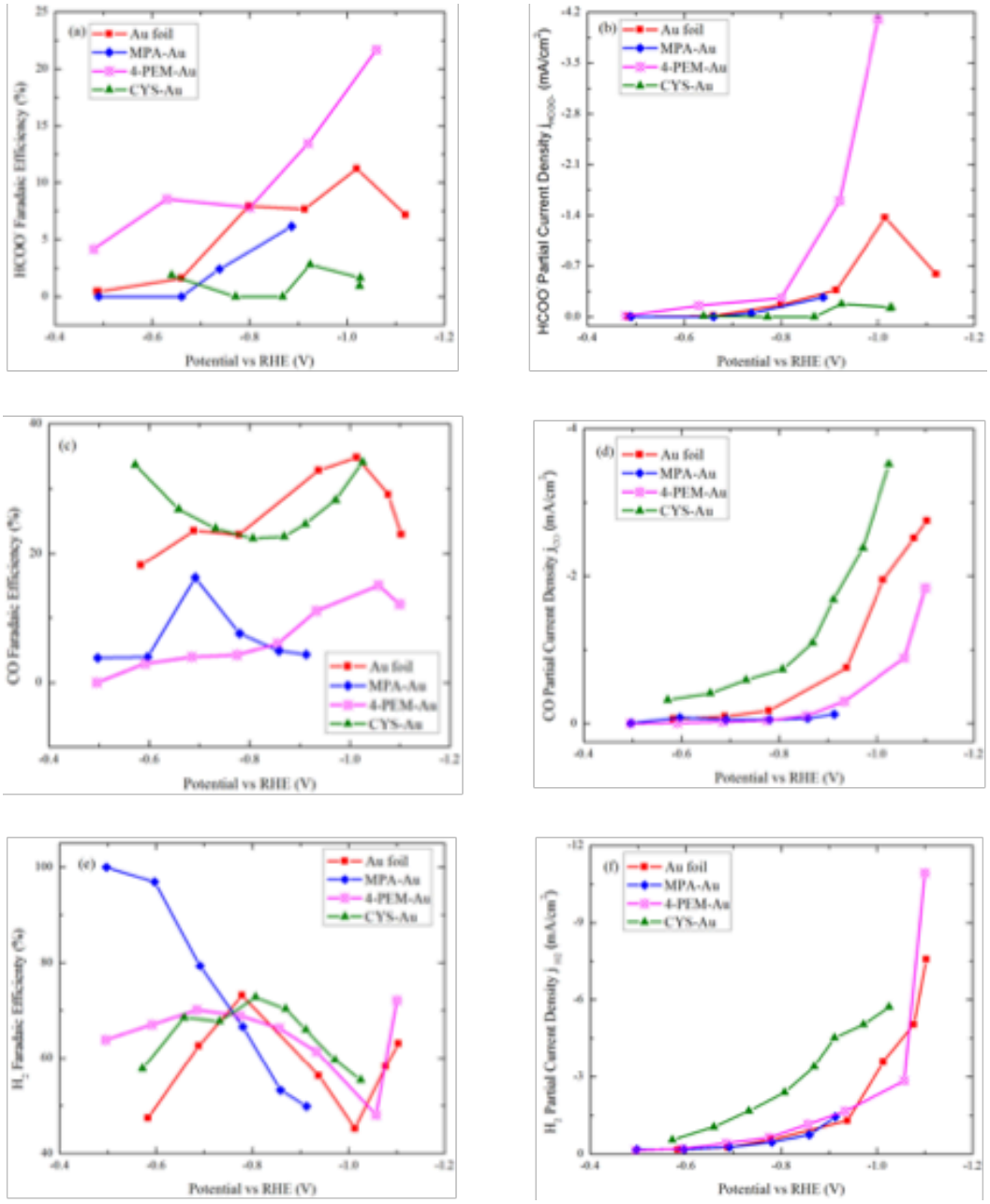

Figure 5.1. Comparison of partial current density and Faradaic efficiency (FE) for thiolate ligand on polycrystalline Au and pure polycrystalline Au. (a) FE of Formate formation; (±2.5% at 95% Confidence Level (CL) (b) FE of CO formation; (±6.2% at CL>95%) (c) FE of H_2 formation (± 25% at CL>95%); (d) Partial current density of formate formation; (e) Partial current density of CO formation (e) Partial current density of H_2 formation.

Table 5.1 summarizes the onset potentials for HER and CO_2 reduction on (functionalized) Au substrates. An Example of determining onset potential from Tafel plot is

given in figure 5.2.[73, 129] The transition point from the thermodynamic controlled region to the kinetic controlled region was defined as the onset potential. The onset potential here is referring to the experimental equilibrium potential.[128]s

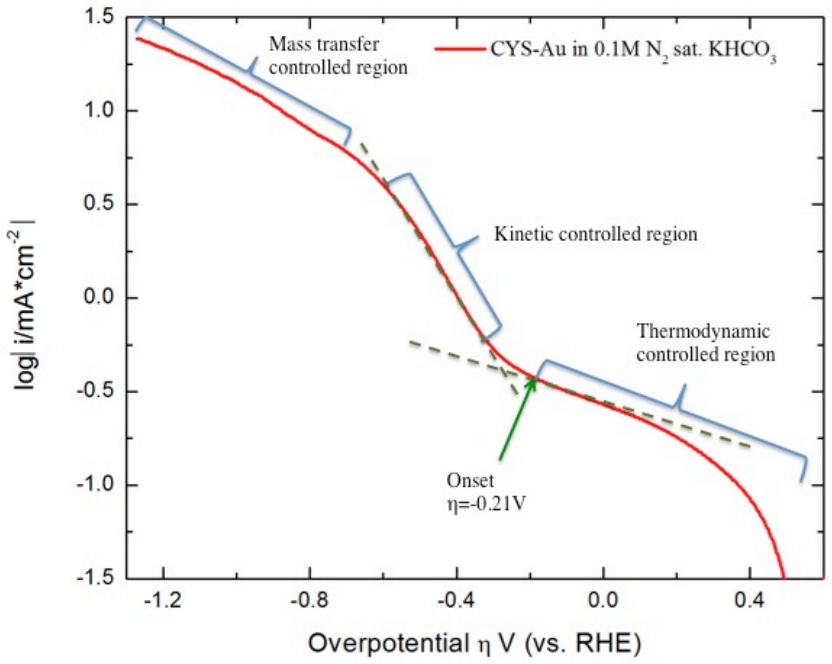

Figure 5.2. Example of method to determine the onset potential for HER on CYS-Au is -0.21V. vs RHE

On the MPA functionalized Au, onset potentials for HER and CO_2 reduction were both shifted anodically (by +10 mV and +100 mV respectively). With the 4-PEM functionalized Au electrode, the HER onset potential was shifted cathodically (-50 mV) and the onset potential of CO_2 reduction was shifted anodically (+30mV). On the CYS functionalized Au, both onset potentials were shifted anodically (+90 mV and +70 mV, respectively).

Table 5.1. Summary of the onset potential of HER and CO_2 reduction and their difference on (functionalized)Au surface

Surface	HER (V vs. RHE)	CO_2 Reduction (V vs. RHE)	V_{HER}-V_{CO2RR} (mV)
Au	-0.30	-0.42	120
MPA-Au	-0.29	-0.32	30
4-PEM-Au	-0.35	-0.39	40
CYS-Au	-0.21	-0.35	140

The enhancement in Faradaic selectivity toward HER on MPA and 4-PEM functionalized Au may be associated with the decreased onset potential differences (E_{HER}^0-E_{CO2}^0) following ligand modification. The correlation between HER selectivity change (S_1/S_2) and onset potential difference may be expressed in a Butler-Volmer relationship. For a 2e-electron transfer process, the current density –potential characteristic can be written as Equation 5.1, where F is the Faraday's constant, k_0 is the standard kinetic rate constant $C_O(0,t)$ is the concentration of oxidized species (in this case proton for HER and CO_2 for CO_2 reduction.) on the electrode at any time, C_R is the concentration of the reduced species (in this case H_2 for HER and CO/HCOOH for CO_2 reduction.), α is the transfer coefficient (in most case, α lies between 0.3 to 0.7, 0.5 is the usual approximate in lack of measurement. α is assumed to be same both reaction for simplicity. f is F/RT, E is the applied potential and E^0 is the equilibrium potential. The reverse reaction can be neglected in this system since the concentration of the reactant is much higher, thus the equation can be reduced to Equation

5.2.[129] The selectivity of HER over CO_2 reduction can be defined as S in Equation 5.3.[130] The selectivity change expressed in S_1/S_2 (sample 1 selectivity / Sample 2 selectivity) is derived in Equation 5.4 with the substitution of Equation 5.2 into Equation 5.3. Assuming the exact same experiment condition (same T, P, C_0, t and E), Equation 5.4 can be simplified into Equation 5.5.

$$j = 2Fk_0[C_o(0,t)e^{-2\alpha f\left(E-E^0\right)} - C_R(0,t)e^{(1-\alpha)2f\left(E-E^0\right)}] \quad \text{Equation 5.1}$$

$$j = 2Fk_0[C_o(0,t)e^{-2\alpha f\left(E-E^0\right)}] \quad \text{Equation 5.2}$$

$$S = \frac{FE_{HER}}{FE_{CO2}} = \frac{i_{HER}}{i_{CO2}} \quad \text{Equation 5.3}$$

$$\frac{S_1}{S_2} = \frac{C_{H1}(0,t)*C_{C2}(0,t)}{C_{H2}(0,t)*C_{C1}(0,t)} e^{-2\alpha f[(E^0_{2,HER}-E^0_{2,CO2})-(E^0_{1,HER}-E^0_{1,CO2})]} \quad \text{Equation 5.4}$$

$$\frac{S_1}{S_2} = e^{-2\alpha f[(E^0_{2,HER}-E^0_{2,CO2})-(E^0_{1,HER}-E^0_{1,CO2})]} \quad \text{Equation 5.5}$$

$$\text{if } \Delta E_2^0 > \Delta E_1^0$$

$$\text{then, } \frac{S_1}{S_2} < 1 \text{ and vice versa.}$$

Thus, the decrease in the difference of onset potentials results in increased HER selectivity. On CYS functionalized Au, the onset potential shifts anodically for both reactions so the product selectivity remains roughly equivalent to the untreated Au electrode.

The dramatic differences in HER selectivity on 2-MPA-Au and 4-PEM-Au at lower potentials (with approximately same onset potential differences) suggest the surface concentration ratio R ($R=C_H/C_C$) must be different. Recent studies on the role of cations by Bell et al. have suggested proton donation from the dissociation of hydrated cations buffers the local electrolyte once the pKa of hydrated cations is lower than local pH.[18] Similar behavior was also observed by Kenis et al.'s study on the effect of hydrated cations on the current density of CO evolution.[131] The pKa of the functional groups are summarized in Table

5.2. Thus, the higher $R_{(MPA)}$ may be attributed to the lower pKa of surface ligand. The HER selectivity at higher potentials may also be attributed to the dominant surface species. As shown in the following section, the deprotonated MPA is the main species on MPA-Au (shown in the stability analysis with IR spectrum). Here, the lower pKa makes MPA both a good proton donor and poor acceptor, thus the surface concentration ratio of H^+ to CO_2 is lower at high potential. The selectivity shift from CO and current density enhancement associate with formate evolution is further discussed in later sections.

Table 5.2. Summary of the pKas of thiolate ligands

Ligands	pKa
2-Mercaptanproponic Acid, (2-MPA)	3.7[132]
4-pyridylethylmercaptan, (4-PEM)	5.2[121]
Cysteamine, (CYS)	9.25[133]

Stability Analysis

The presence of SAM on the freshly prepared samples were first confirmed with AFM characterization. The roughnesses of the surfaces were characterized with AFM. The reduced surface roughness on functionalized Au suggests a uniformly packed structure.[134]

Table 5.3. Surface roughness of samples.

Surface	RMS (nm)
Au	7.38
MPA-Au	2.60
4-PEM-Au	2.08
CYS-Au	2.27

One important concern associated with the electrochemical reduction of CO_2 in the presence of functionalized surfaces is the stability of the ligand at the potentials required to reduce CO_2. Several studies have shown the cathodic desorption and dissolution of alkanethiolates on gold;[135-136] however, many thiolates are considered stable at cathodic potentials. [137] More recent *in situ* work with sum frequency generation vibrational spectroscopy by Badeli et al[72] shows that octadecanethiol ligands remain at the surface even at high cathodic potentials owing to the van der Waals interaction between alkyl chain and the low solubility in aqueous solution. Aromatic thiolates are particularly stable as the aromatic group appears to enhance surface bonding.[138] Here we carried out the ex-situ ATR-IR experiments to study the stability of ligands on Au foil.

2-Mercaptopropionic acid (MPA)

Figure 5.3 (b) compares the ATR-IR spectrum between freshly prepared MPA-Au sample along with the same sample post electrolysis at -0.94V vs. RHE and post electrolysis at -1.00V vs. RHE (solution phase thiols spectra are available in the figure 5.3 (a)). In the freshly prepared electrode spectra, vibrations at 1723 cm^{-1} (a) corresponds to the C=O stretching of the COOH group. The symmetric and asymmetric stretching of the $-CH_3$ group showed up at 1372 cm^{-1} (b) and 1449 cm^{-1} (c). The C-C stretching is also observed at 1241cm^{-}

[1] (d).[66, 70] The slight shoulder at 1607 cm^{-1} (e) and the small peak at 1421 cm^{-1} (g) correspond to the asymmetric and symmetric stretching of $-COO^-$, respectively.[66] On the spectrum of the post-electrolysis (-0.94 V vs. RHE) MPA modified Au sample, the asymmetric stretching vibration at 1583 cm^{-1} (e) with a shoulder at 1662 cm^{-1} (f) indicates the presence of the deprotonated COO^- group and COOH group, respectively. The rise of peak g coupling with peak e indicates that deprotonated ligand species dominant the surface during/after the electrolysis. The vibrations of the CH_3 group and the C-C bond remain similar in pre and post electrolysis sample. Slight shifts in wavenumbers indicate the change in configuration of the monolayer results in stronger interaction between Au surface and the functional group. However, at more negative potentials (-1.00V vs. RHE), decreased absorbance associated with $-CH_3$ group and COO- group suggests the lower concentration of surface ligand. This suggests the potential window for MPA to remain on the surface is below -0.94 V vs. RHE.

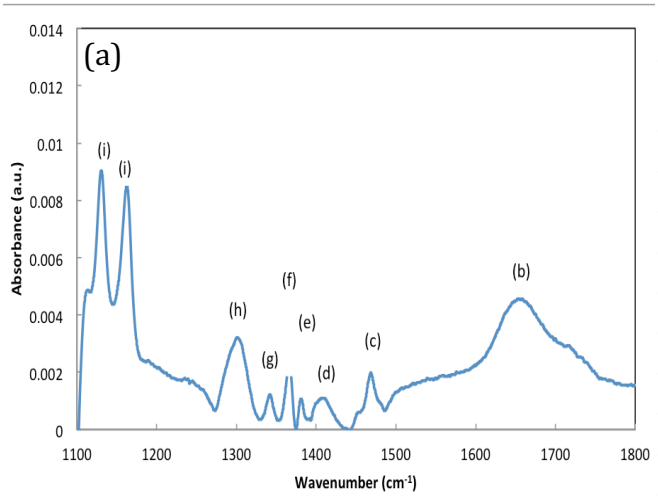

(b)

Peak	Wavenumber (cm^{-1})	Assignment
a	1723	C=O str in -COOH
b	1642	$-COO^-$ asym str
c	1463	$-CH_3$ asym str
d	1398	$-COO^-$ sym str
e	1378	$-CH_3$ sym str
f	1362	$-COO^-$ sym str
g	1337	-OH deformation
h	1294	C-C str
i	1128 &1159	C-O str

Figure 5.3. (a)Solution phase MPA spectra and peak assignments (b)Comparison of ATR-IR spectra for MPA SAM on Au (—) fresh prepared (– –) Post-electrolysis at -0.94V vs. RHE (–·) Post-electrolysis at -1.00V vs. RHE

Figure 5.3 cont'd.

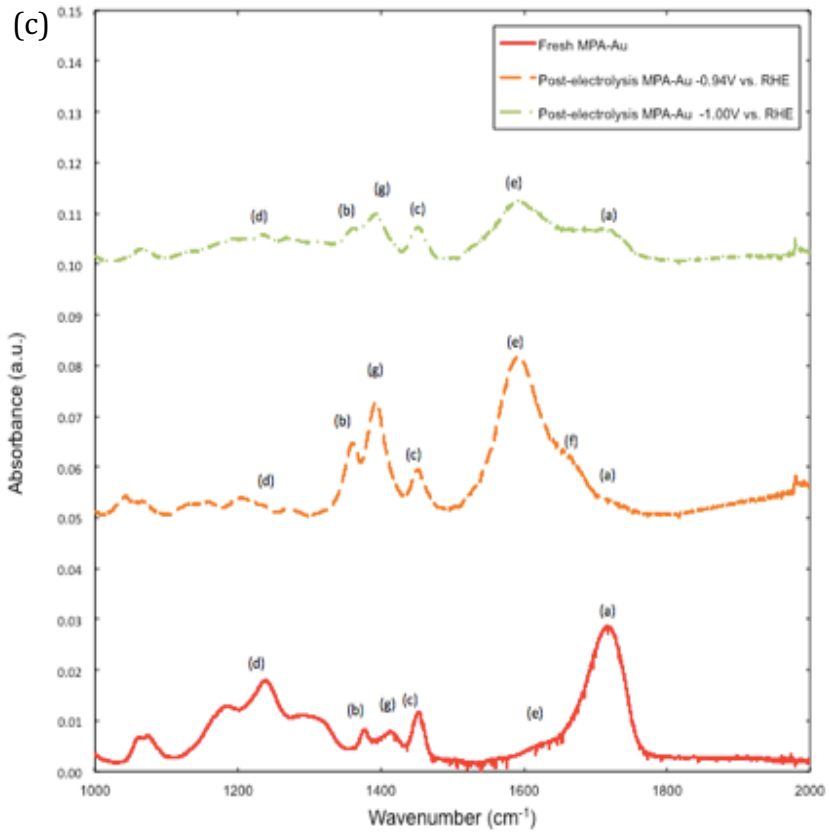

4-pyridylethylmercaptan (4-PEM)

Figure 5.4(b) presents the comparison between the freshly prepared 4-PEM-Au spectra and the post-reaction spectra at -1.04V vs. RHE for the sample. The bands at 1606 cm^{-1} (a), 1564 cm^{-1} (b), and 1521 cm^{-1} (c) [66, 139] characterizing for the ring structures in pyridine and 780 cm-1 [f] and 850 cm^{-1} (e) charactering C-H deformation vibration present in both spectra. [66, 126] The vibration d was shifted from 1506 cm^{-1} to 1484 cm^{-1} indicating the presence of protonated pyridine species on the surface.[139] This indicates that the 4-pyridylethylmercaptan remains intact at -1.04 V vs. RHE within time of electrolysis for the product analysis and further the pyridinium is the main functioning ligand in the reactions.

The presence of protonated species during/after further supports the notion of ligand participation in proton transfer reactions.

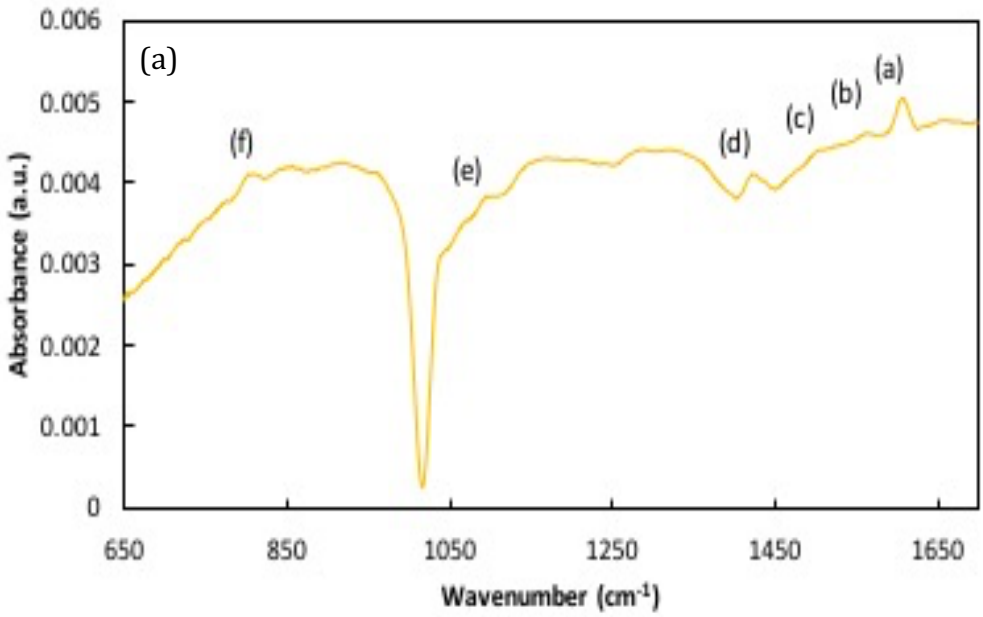

(b)

Peak	Wavenumber (cm^{-1})	Assignment
a	1602	C=C Ring str
b	1556	C=C Ring str
c	1496	C=N Ring str
d	1417	C=C Ring str
e	1089	Pyridine C-H deformation
f	798	Pyridine C-H deformation

Figure 5.4. (a)Solution phase 4-PEM spectra and peak assignments (b) Comparison of ATR-IR spectra for 4-PEM SAM on Au (—) fresh prepared (—) Post-electrolysis at -1.04V vs. RHE

Figure 5.4 cont'd.

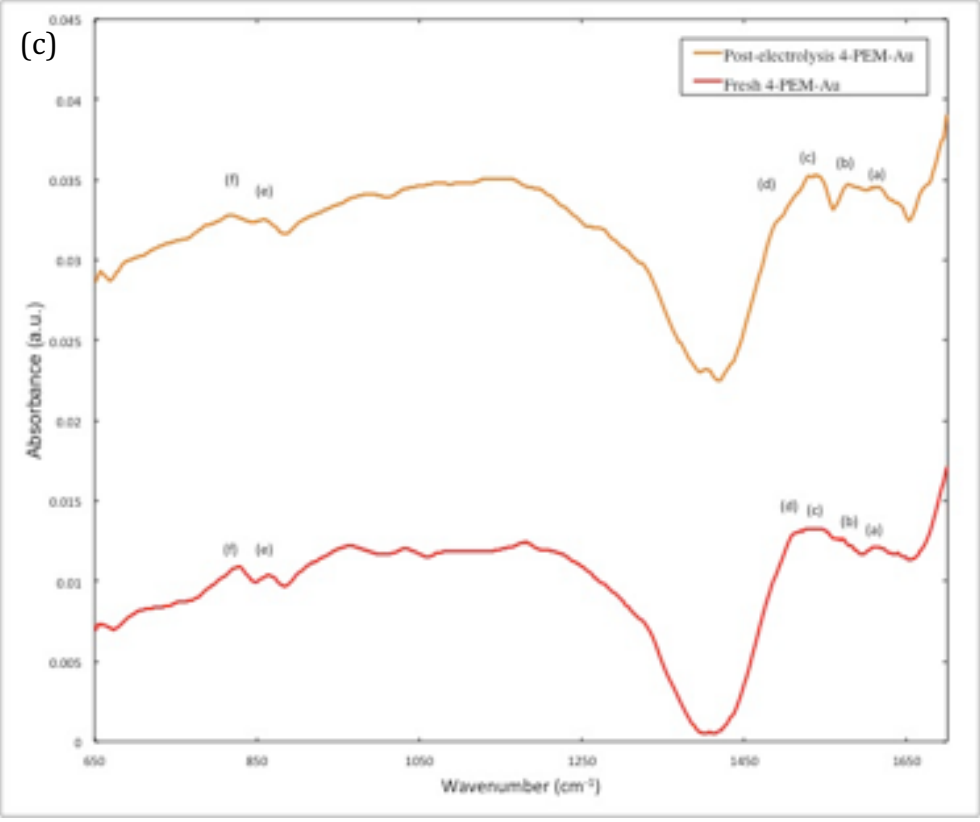

Cysteamine (CYS)

Figure 5.5(b) shows the comparison between the spectra of the freshly prepared CYS-Au surface and the spectra from the same electrode post electrolysis. These spectra show absorbance peaks at 1550 cm^{-1} (a), 1465 cm^{-1} (b), 1430 cm^{-1}(c), 1272 cm^{-1} (d) and 1064 cm^{-1} (e), which correspond to the N-H bonds bending vibrations, CH_2 deformation, CH_2-S wagging and C-N stretching respectively. [66, 71] Note, the solution phase ligand FTIR spectra may be found in the SI. The red shifts indicate the strong interactions between the surface and the ligand. The presence of the absorption peaks in both spectra confirms the stability of cysteamine on the Au surfaces within the potential range of interest.

(a)

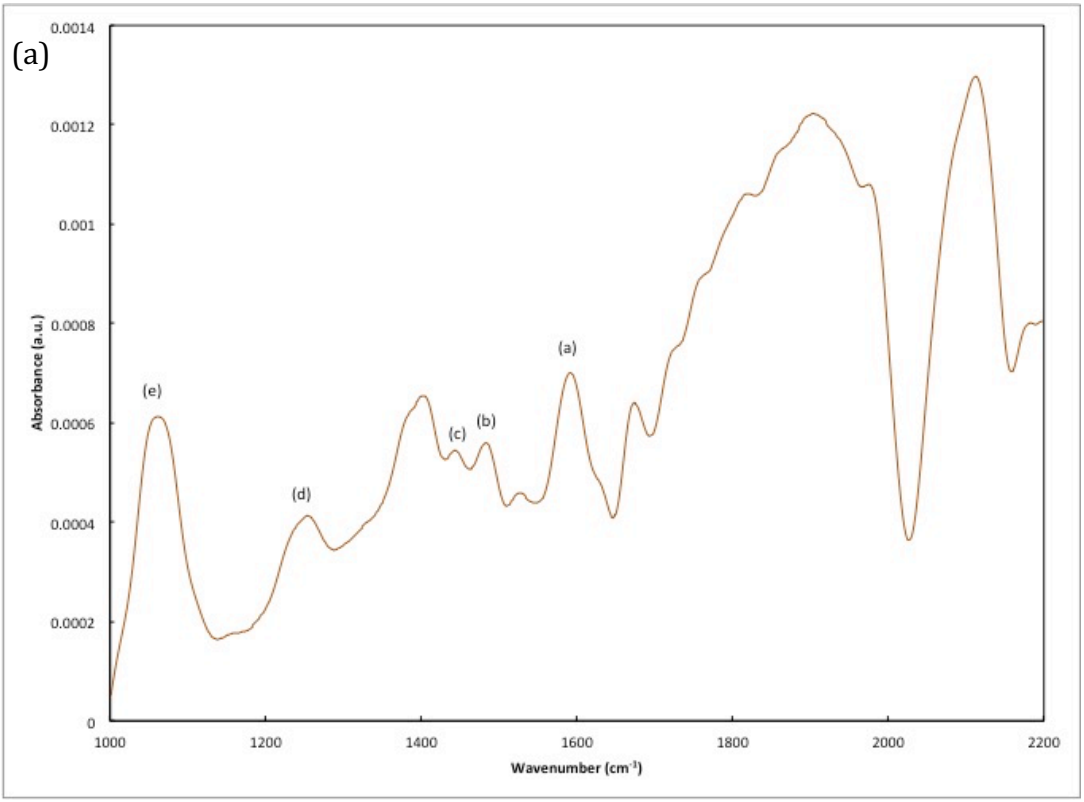

(b)

Peak	Wavenumber (cm^{-1})	Assignment
a	1587	N-H deformation
b	1475	C-H deformation $–CH_2-$
c	1437	C-H deformation in $–CH_2-S-$
d	1243	C-H wagging in $–CH_2-S-$
e	1055	C-N str

Figure 5.5. (a)Solution phase CYS spectra and peak assignments. (b) Comparison of ATR-IR spectra for CYS SAM on Au (—) Fresh prepared
(—) Post electrolysis at -1.1V vs. RHE

Figure 5.5 cont'd.

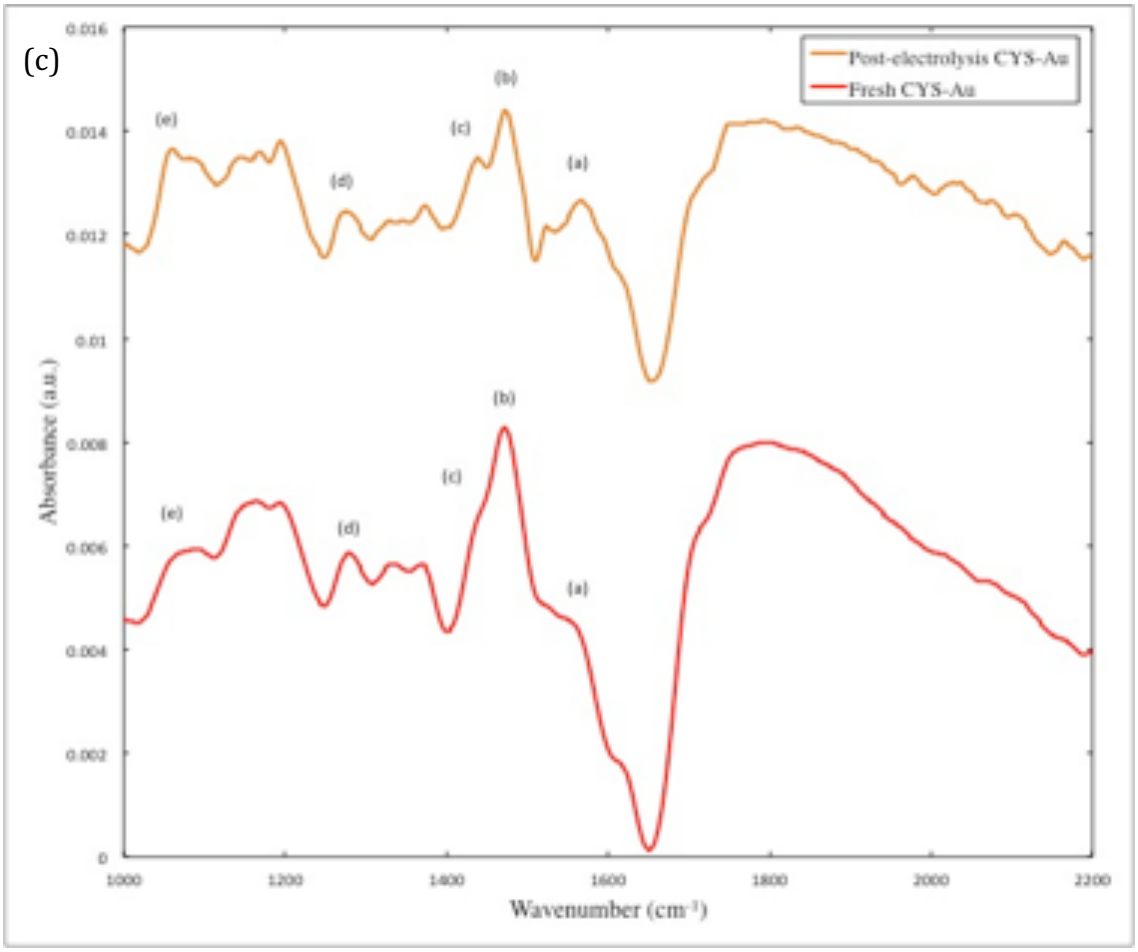

Mechanism

Clearly, ligand modification of Au electrodes influences product selectivity of the CO_2 reduction reaction. Based on these results, the nature of the shifted selectivity likely originates from the separation of proton and electron transfer reactions enabled by the ligand. For example, consider the directed proton transfer behavior of enzymes involved in coupled electron transfer (PCET) reactions.[140-142] Nocera et al. showed enzymes are capable of disentangling proton transfer and electron transfer and allowing transfer coordinates on highly different length scales. In fact several studies have explored the potential of "wiring"

enzymes to combine the selectivity of the natural catalysts with the advantages of externally-driven cells.[143] [144] [145] While there are limitations related to the wiring of enzymes and stability concerns; there are a number of works showing functionalized electrodes, such as those considered here, are stable in the potential range needed for electrochemical reduction reactions.[63, 146-147] Given the wonderful selectivity of natural catalysts, it is likely that similar directed proton transfer reactions may be possible at ligand functionalized electrodes, especially at moderate potentials.

The 3-fold increase observed in formate production when Au electrodes are functionalized with 4-PEM is remarkable. Given the presence of pyridine functional group, previous results on pyridine/Pt systems may provide some mechanistic insights. Bocarsly et al. reported the production of CH_3OH (11~39% Faradaic efficiency) and HCOOH (7~16% Faradaic efficiency) with Pt/Pd electrodes in the presence of 10mM pyridine and its substituted derivatives in the supporting electrolyte.[57, 121] Pt was reported as HER dominant (~95% Faradaic efficiency) electrocatalysts, and Pd mainly yields CO formation.[20] While the current density with the 10 mM pyridine-dosed electrolysis was relatively low (50 $\mu A/cm^2$) compared to this work (0.2~15 mA/cm^2); pyridine appears to have a strong influence in the CO_2 reduction selectivity. However, the nature specifically whether a surface or solution phase pyridinium is involved is not well established.

Initial work by Bocarsly et al. analyzed the data from cyclic voltammetry and proposed a mechanism[119] that proceeds with pyrH* as cocatalyst based on Gaussian calculations: a $1e^-$ reduction of the $pyrH^+$ to pyrH* that reacts with CO_2 and forms a CO_2-pyrH radical carbamate with inner-sphere interaction, and another surface-adsorbed H atom reacted with the surface adsorbed carbamate to yield formic acid. In that mechanism, further

proton shuttling to formate yields methanol. Later work considering acidity constants for $pyrH^+$ and pyrH* by Keith and Carter showed the unfavorable deprotonation step for $pyrH^*$ since its pKa was calculated as ~27[148]. Instead, they proposed a surface mechanism[149-150] using first-principles quantum chemistry where the surface bound dihydropyridine (DHP) is the co-catalyst that takes hydride from Pt and transfers the hydride and proton to the CO_2 to yield formate.

In another study of the functional role of $pyrH^+$ during aqueous CO_2 electrochemical reduction, Batista et al. proposed an alternate proton–coupled hydride transfer mechanism[151]. The 1 e^- reduction of $pyrH^+$ produced hydride on Pt surface. CO_2 is susceptible to a 1 e^- reduction by the surface hydride coupled with another proton from $pyrH^+$. In this work, the structure of the tethered 4-PEM likely prohibits formation of DHP since the carbon atom para to N is fully bonded and does not undergo hydrogenation. Also, the thiol-tether and electron transfer requirements[152] makes the pyridinium radical formation unlikely since the electron transfer rate constant decays exponentially with the increase in donor-acceptor distance (Au and N). The electron transfer limitations also apply to Batista's proton-coupled electron transfer model where the surface hydride is replenished by the reduction of $pyrH^+$.

Here, we propose a modified formate production mechanism (depicted in Figure 5.6) on 4-PEM modified Au electrodes. The first proton from aqueous solution is reduced and forms H atom adsorbed on Au (step 1a). Note the moderate pKa suggesting that the surface is not dominated by protons from the $pyrH^+$. A two-electron transfer to hyride is not plausible since the hydride dominated surface would result in HER assuming sufficient protons are available from solution. The electrophilic attack of CO_2 to the adsorbed H yields HCO_2* (step 2).[153]

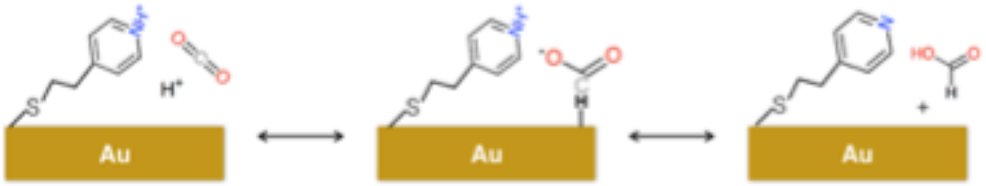

Figure 5.6. Proposed Formate formation mechanism at 4-pyridylethylmercaptan modified Au surface

Compared with Au foil, the slightly higher surface concentration of H^+ (5.2 for 4-PEM versus 6.8 in 0.1M $KHCO_3$) decreases the probability of first electron transfer to CO_2^- and forms the -COOH with the proton from the solution which is the expected path to the CO evolution[44-45, 49, 153]. Thus, a HCO_2* intermediate after the first pair of proton-electron transfer steps is likely a key step toward the production of formate. Previous simulation studies by Nørskov et al. have shown strong correlations between HCO_2* and $HCOO^-$.[153] Thus a slight selectivity shift between CO and formate is probable. Next, the tethered $pyrH^+$ in thiolate group, transfers a proton to the nearby oxygen of the HCO_2* coupled with 1e- transfer from surface (Step 3a). The enhanced HER observed at lower potentials also supports this proton-induced desorption mechanism (Step 3b). The protonated pyrH+ is replenished with proton source from the electrolyte (Step 1b).

Step 1a:

Step 1b:

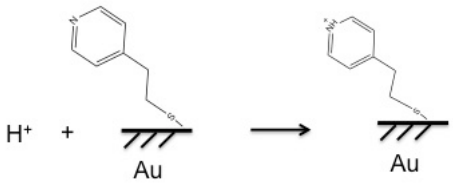

Step 2:

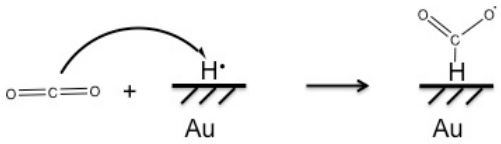

Step 3a:

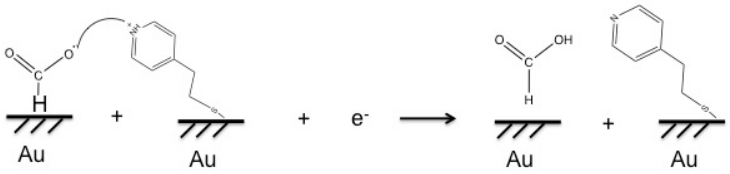

Step 3b:

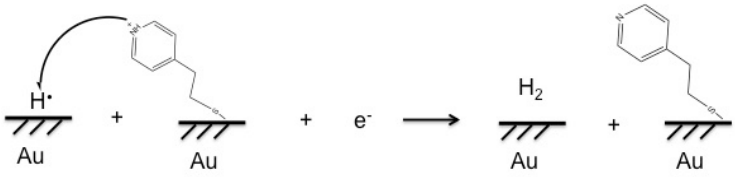

According to this mechanism, we propose that the proton donating ability (pKa) of the ligand correlates with CO_2 reduction to formate and H_2 yields as observed on functionalized Au electrodes. Ligands with low pKa values such as 2-MPA, facile proton donation favors the HER through step 3b. Ligands with high pKa, such as CYS result in diminished deprotonation as well as step 3b. The product selectivity is virtually unchanged relative to untreated Au electrodes as well. The 2-fold enhancement in partial current density observed with CYS is likely the result of the amine's ability[154] to complex CO_2 near

the surface. The intermediate pKa of 4-PEM (=5.2) facilitates the proton transfer to CO_2 in a way that yields formate.

Conclusion

Au electrodes functionalized with monolayers of thiol-tethered ligands were evaluated for their ability alter the selectively of CO_2 reduction reaction. A two-fold increase in Faradaic efficiency and three-fold increase in formate yield were observed with the 4-PEM-modified Au compared to the best results with untreated Au. MPA-modified Au electrodes favored only the HER and CYS-modified Au resulted in increased CO and H_2 production with virtually no changes in selectivity. A proton-induced desorption mechanism is proposed to account for the remarkable increase in formate production on 4-PEM-modified Au electrodes. The inability of the CYS and MPA-modified electrodes to yield significant amounts of formate is believed to be associated with the pKa of the surface tethered functional group. At a more fundamental level, the ligand-mediated proton transfer with electron transfer at the surfaces demonstrates the potential for improved selectivity via "directed hydrogenation" reactions.

CHAPTER 6. FUNCTIONALIZED SILICA FACILITATED PROTON-COUPLED ELECTRON TRANSFER IN ELECTROCHEMICAL REDUCTION OF CO_2

Introduction

Previous studies have shown that the ligands can be used to tune the catalysis of CO_2 reduction through methods such as: reconstructing metal surface to high coordinated catalytic active sites and leveraging surface proton concentration with CO_2 concentration. However, the reaction on SAM modified are still limited to give $2e^-$ products (CO and HCOOH). Though the reconstruction of Au will create additional sites for CO production which is known to be the key intermediate for further reduction reaction, the weak adsorption of CO on Au[39] prevents the further hydrogenation from going on. Despite that the protonation did can be leveraged with the pKa of ligands to certain extent, it also sacrificed the production of CO that can be further reduced to methanol which holds higher energy density. Further catalyst engineering is still in need to optimal catalyst that can selectively catalyze CO_2 reduction to oxygenates (such as CH_3OH, C_2H_5OH, etc.),

First lesson from thiol-Au system is that metal substrate with stronger CO adsorption is a vital part for any downstream reduction. Metals on the left part of volcano plot are of choice. Pt[155], Fe[156] and Ni[157] are excluded since they are known for CO poisoning, which leave Pd as a potential candidate. Previously, Hori et al. has look into the product distribution with Pd foil catalyzed CO_2 reduction, CH_4, CO, HCOOH and H_2 are all found.[158] CH_3OH production was also detected on Pd with the pyridine added electrolyte. [57] The formation of CH_4 and

---

Partially reprinted with permission from ECS Transctions.

CH_3OH indicate the possibility for CO to be further reduced and hydrogenated for further hydrocarbon or alcoholic products on Pd.

Previously, Min and Kanan[159] has looked into the Pd nanoparticle (NP) dispersed on carbon support. Formate production was found to be favored at low overpotential. The CO production dominates at high overpotential. Gao et al.[160] reported the size -dependent activity/ selectivity in CO_2 reduction on Pd NP. 91.3% FE for CO production was achieved at -0.89 V vs. RHE over 3.7 nm Pd NP. Based on the previous literature, Pd np should be a promising candidate in producing CO and CO* can be stabilized for further hydrogenation to oxygenate products.

Second lesson from previous experiment is that the presence of ligand on the Au will only result in protonating to the substrate surface which favor the formation of -HCOO instead of -COOH that give CO which is the real intermediate in need for proton. A second substrate for ligand is necessary to keep the ligand away from metal surface to lower the probability of proton transfer to metal surface while still remaining protonation ability. SiO_2 was a good candidate due to its strong covalent bond with silanes. Previous observation of enhanced CO production on the cysteamine modified Au suggested that the surface amine moiety inherits from the CO_2 absorption with amine. Therefore, silanes with moieties that holds pKa range from 5.2 to 12.75 were chosen in the experiment. The silanes also fell in 3 categories of amine: primary, secondary and tertiary.

Previous study has shown the macroscopic composite Pd/C-Pt/C catalyst in promoting the formic acid productions. The H_2 formed from Pt/C layered contributed to the HCOO* formation which is the key intermediate for HCOOH production.[161] By mixing the functionalized silica with the Pd/C np (Pd/C-X/SiO_2, X stand for the ligand), the composite

electrocatalysts were evaluated in the CO_2 reduction reaction for CH_3OH production. Pd/C-Pyr/SiO_2 showed 6 times increase in FE and 2 times in partial current density for CH_3OH production when compared with Pd/C. Interfaces in the composite catalyst with enhanced CO_2 and proton concentration are attributed to enhanced oxygenate production.

Experimental

Electrode Fabrication:

Nanoparticle synthesis**:** Carbon-supported Pd nanoparticle (Pd/C np) was synthesized according previously reported method[160] with $NABH_4$ (Sigma Aldrich, ≥96%) as a reductive agent and $Na_3C_6H_5O_7 \bullet 2H_2O$ (Sigma Aldrich, ≥99%) as the capping agent. 0.5 mmol of $PdCl_2$ (dissolved in 0.1M HCl) was mixed with 4 mmol sodium citrate dissolving in 200 ml of H_2O. 212.8 mg of carbon black (Vulcan XC-72R) was added to the solution and sonicated for 30 min. 50 ml of 0.1 M $NaBH_4$ was added into the colloidal suspension in dropwise under vigorous stirring. The solution was kept stirring for 8h. The precipitate was filtered, washed and dried overnight under vacuum.

Silica powder functionalization[162]: The silica powder was baked at 200°C for 2 hrs before silianization. The silanes ((3-acetamidopropyl) trimethoxysilane (Ace-SiO_2), 2-(2-pyridylethyl) trimethoxysilane (Pyr-SiO_2), and 3-aminopropyltrimethoxysilane (Ami-SiO_2)) was hydrolyzed in deionized water for 30 min. The concentrations for all silanes were kept for 0.25% by weight. 0.55g of silica powder (Aldrich, 99%) was added to a vial with 5ml of hydrolyzed saline solution and sonicated vigorously. The silanes were allowed to interact with the silica powder for 3 min before being removed by centrifusion for 5 min at 14000x

rps and decanted. The functionalized silica powder was air dried and stored for later catalysis study.

Cathode: 4.4 mg of effective catalyst (with / without 20 wt% (functionalized) silica) was dissolved in 200 µl isopropanol (IPA, Sigma Aldrich, ≥99.7 %) with 20 µl 5wt% Nafion as conductive binder. The choice of IPA was to prevent false reading in NMR products. The catalyst suspension was sonicated for 30 min before brush painted onto the well-polished glassy carbon electrode. The painted electrode was air-dried overnight. The reductive desorption experiment of silanes on Pd wire was performed to exclude the possibility of self-assembled monolayer on Pd.

Electrochemical measurement:

The reduction reaction was carried out in a H-type cell with 10 ml of 0.1 M $KHCO_3$ supporting electrolyte in each compartment. The two compartments were separated by Nafion 117 membrane (FuelCellEtc) to prevent the reduced product from being oxidized at the anode. The prepared electrode serves as working electrode, while the Pt wire serves as the counter electrode with the Ag/AgCl (sat. 3 M NaCl, BASI, RE-5B) as reference electrode. The electrolytic potential was supplied by potentiostat (PAR 263A) and reported in this work with the manual correction of measured uncompensated resistance. Electrochemical current density was normalized to the catalyst electrochemical surface are (ECSA), as measured with the oxide stripping method[163].

CO_2 was flowed continuously through a DI water filled bubbler followed by a gas dispersion tube into the cell at a flow rate of 40 ml/min and a pressure of 1 atm. The electrolyte was kept stirred to minimize the mass transfer resistance. Chrononamperometry experiments were conducted after both cells (to avoid PH cell in between) were saturated

with CO_2 for 15 min at each potential, and the gas effluent from the cell was auto-sampled to the FID and TCD equipped gas chromatograph (Shimadzu, GC 2014) at 15 min interval.

The liquid products were collected after 30 min electrolysis and analyzed with NMR (Bruker AVIII 500MHz spectrometer with liquid nitrogen cooled prodigy TCI probe) with an excitation sculpting pulse technique for water suppression as described in previous literature. 10 mM DMSO was chosen as the reference peak. The 1D ^1H NMR data were processed with topspin 3.2.

The linear sweep voltammetry (LSV) was performed in a three-electrode cell. The electrolytes were purged with N_2 and CO_2 for 15 min in advance for HER and CO_2RR, respectively. The voltammetry was cruised from 0 to -2 V vs. Ag/Cl at a scan rate of 10 mV/s. The reported voltages were converted to RHE scales

Characterization:

Nanoparticles:

Transmission electron microscopy (TEM)provides high resolution image of ultra-small specimen by transmitting a beam of electrons through. The electron beam works the same way as light microscopy except lower de Broglie wavelength. The interference formed by beams can provide detail information about crystal facet.

The Pd/C np was examined with transmission electron microscopy (TEM) by dispersing the IPA dissolved sample onto Cu mesh grids to obtain the size of the synthesized nanoparticle.

Functionalized Silica:

The infrared spectrum of the ligand functionalized silica were collected with a Nicolet 6700 FTIR spectrometer with a nitrogen-cooled narrow-band MCT detector in the Diffuse

Reflectance Infrared Fourier transform (DRIFT) accessory set up. DRIFT has been a sensitive spectroscopy for surface structure on powders.[164] The spectra on SiO_2 powder was taken as background. Spectrum on ligand-silianized silica were taken with a resolution of 0.5cm^{-1} and 128 scans. The reported spectrum were background corrected and smoothed.

Result and Discussion

The as synthesized Pd/C np was characterized with TEM. Figure 6.1 shows the TEM image of nanoparticle, the average particle size was 4.9 ± 0.7 nm with characteristic Pd (111) lattice spacing of 0.21nm. Previous publication[160] has reported dominate CO production on Pd/C np at this size.

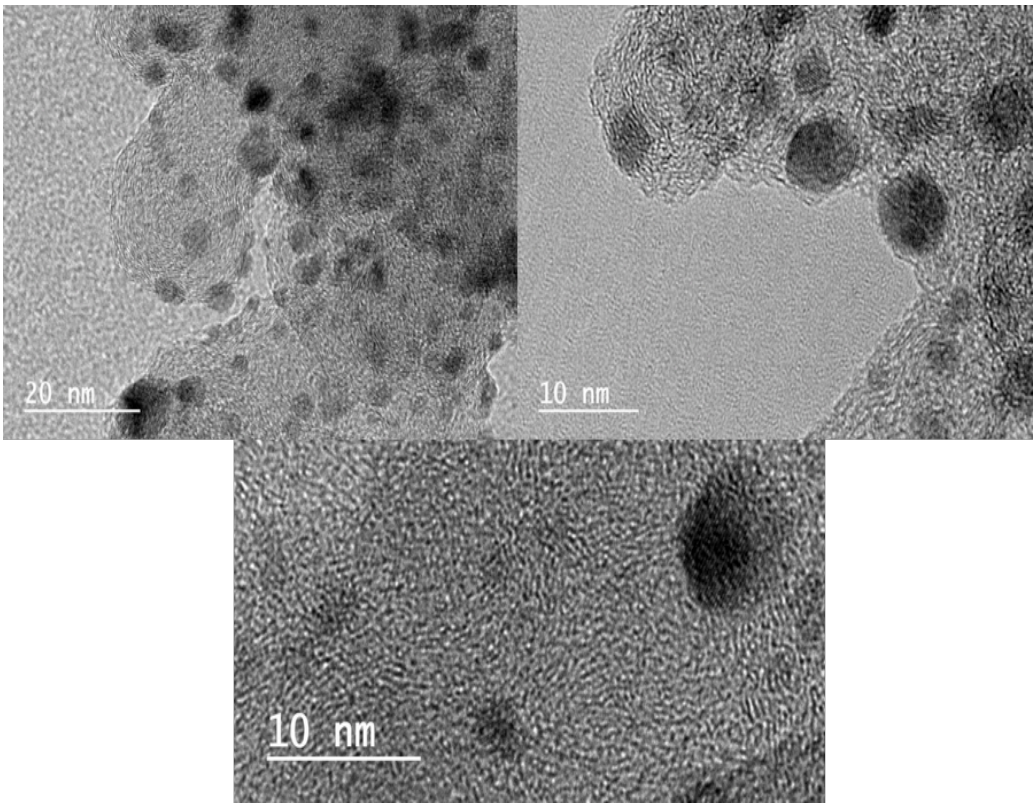

Figure 6.1. TEM image of Pd/C np.

The silainzed silica powder was characterized with FTIR. The IR spectrum were shown in figure 6.2. The absorption peaks corresponding to functional groups were assigned according to previous literature.

Figure 6.2 (a) presents the infrared spectrum of Ace on silica powder. Due to the complexity of the silianes' structure, only features from functional moieties are discussed here. Absorbance peaks at 1288 cm^{-1} (i), 1382 cm^{-1} (ii), 1508 cm^{-1} (iii), 1733 cm^{-1} (iv) and 2994 cm^{-1} (v) are due to vibration of amide III band, symmetric C-H deformation in CH_3-CO-, amide II band, amide I band[165] and asymmetric C-H stretching in CH_3-CO-, respectively.[66]

Figure 6.2 (b) shows the IR spectrum of Pyr/SiO_2. The absorption peaks (i) through (iii) between 1440 cm^{-1} to 1615 cm^{-1} arise from the framework vibration of pyridine ring stretching.[66, 166] Peaks (iv) and (v) are ascribed to the C-H stretching in -CH_2- backbone chain groups.[66]

Figure 6.2 (c) displays the IR spectrum of Ami/SiO_2. The absorption features from NH_2- are evident. Vibration at 829 cm^{-1} (i), 1240 cm-1 (iii) and 1612 cm^{-1} (iv)[167] are stretching from N-H out of plane bending, NH_2 rocking and N-H deformation. Vibration at 1142 cm^{-1} (ii) is the C-N stretching in -CH_2-NH_2.[66]

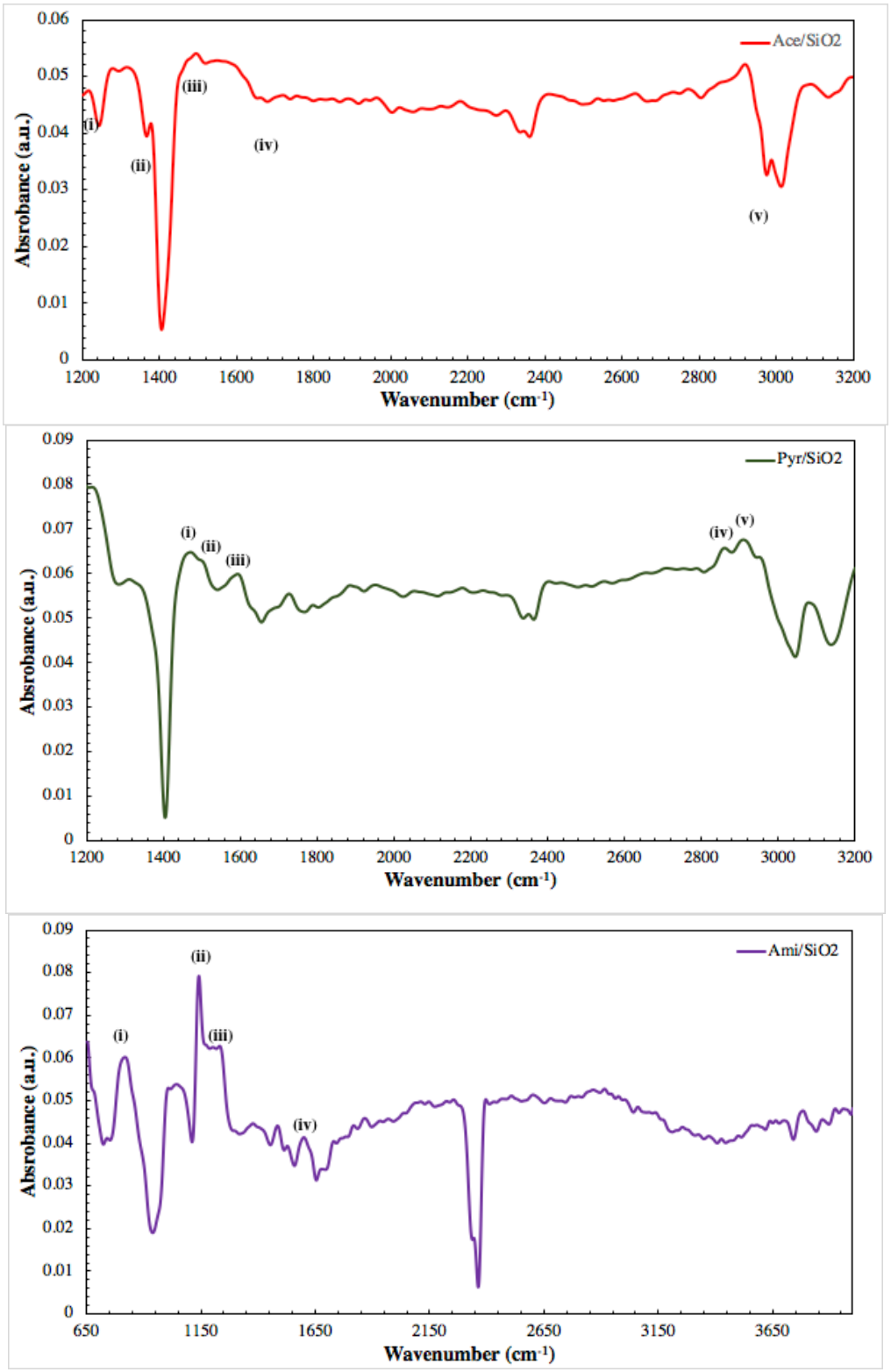

Figure 6.2. FTIR spectrum for (a) Ace-SiO_2 (b) Pyr-SiO_2 (c) Ami-SiO_2

The vibrations featuring the corresponding moieties confirms the successful functionalization of silica powders that were be used for composite catalyst fabrication. The post-electrolysis was hard to retrieve for ligand characterization. However, the ligand was observed in the NMR data suggests that the reductive desorption happens during the electrolysis which substantiate that the total product FE is less than 100%.

Figure 6.3 summarized the catalytic performance of Pd/C np with ligand/SiO_2 in CO_2 reduction. The measured CO faradaic efficiency on Pd/C was slightly below the valued reported in previous literature[160]. This was attributed to the difference in reactor setup that the gas diffusion electrodes were used in the literature as opposed to the H-type cell here. Previously study has also suggested that reactor setup could affect the selectivity.[12] Data reported in this work are generated with the same setup for consistency.

Comparing with Pd/C np, the H_2 production was obviously suppressed at low overpotential (>-1.0 V vs. RHE) in terms of both FE and j_{H2} over Pd/C-Pyr-SiO_2 and Pd/C-Ami/SiO_2 by 10~20% and -0.2 mA/cm^2, respectively. Though the j_{H2} on Pd/C-Ace/SiO_2 was also suppressed, the FE remained same with Pd/C np. At high overpotential (<-1.0 V vs. RHE), the H_2 production was enhanced over Pd/C-Pyr/SiO_2 in both FE and j_{H2}.

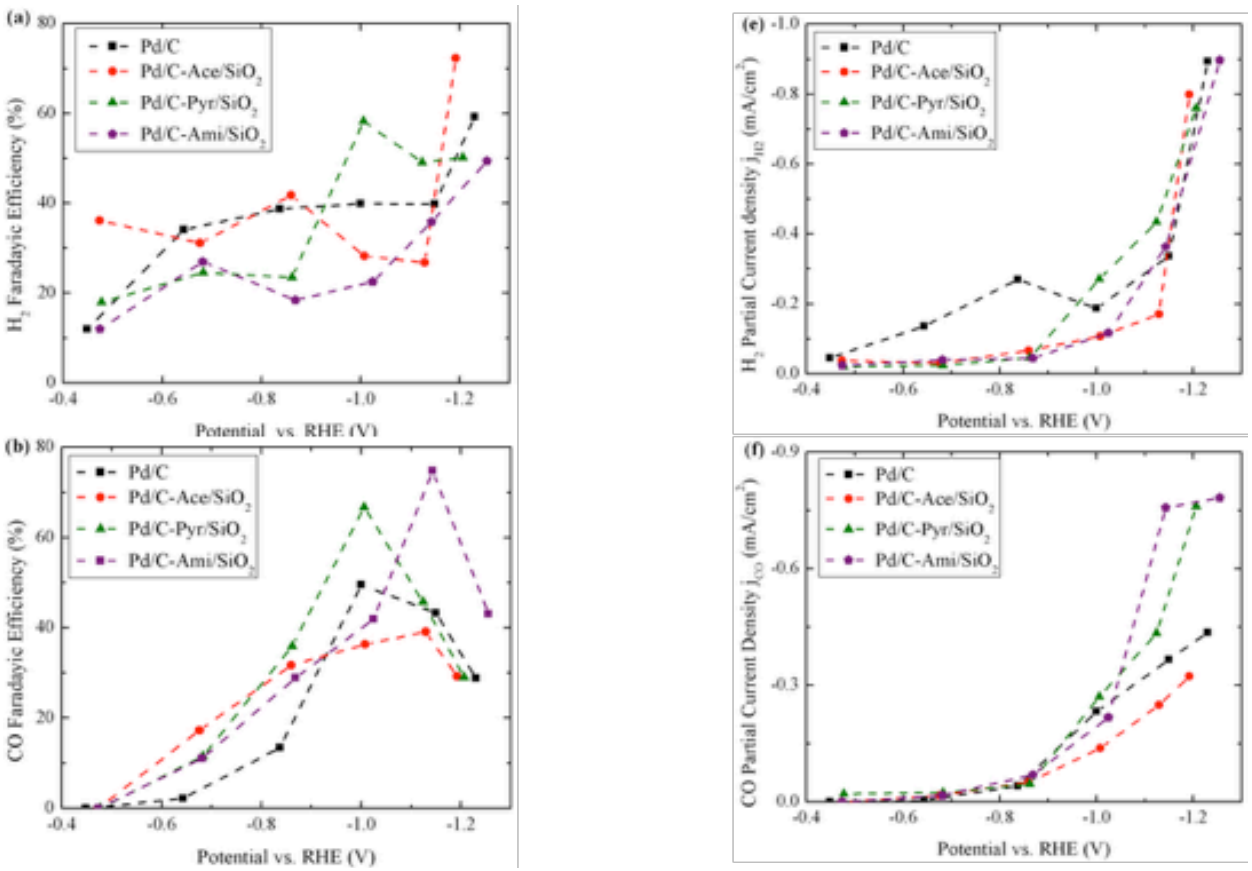

Figure 6.3. Comparison of product (H_2, CO, HCOOH and CH_3OH) partial current density and Faradaic efficiency (FE) for Pd/C and Pd/C with ligand supported on SiO_2. (a) FE of H_2 formation, (b) FE of CO formation, (c) FE of HCOOH formation (d) FE of CH_3OH formation, (e) partial current density of H_2 formation; (f) partial current density of CO formation, and (g) partial current density of HCOOH formation (h) partial current density of CH_3OH formation.

Figure 6.3 cont'd.

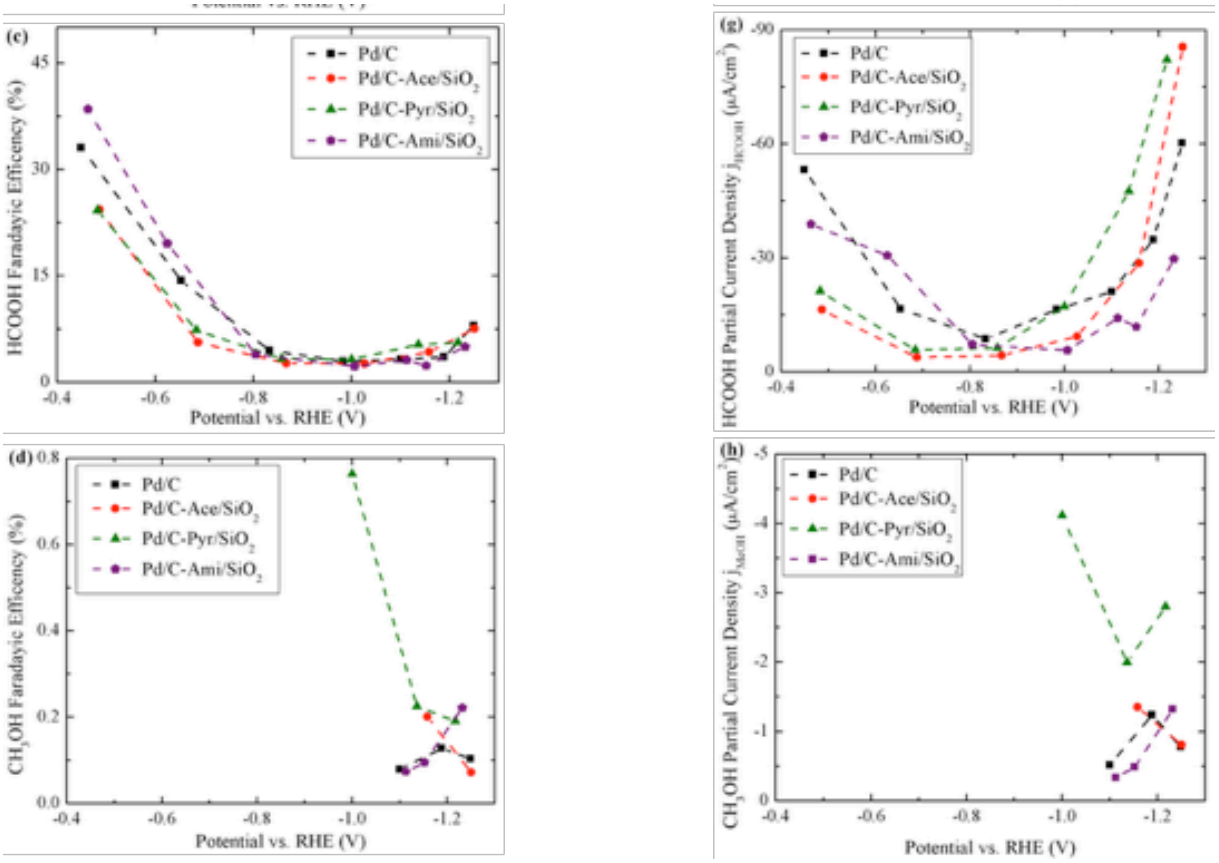

The CO production FE were enhanced over the entire range of potential investigated for all the catalysts with functionalized silica except minor decrease over Pd/C-Ace/SiO_2 at overpotential greater than 1 V vs. RHE. The enhancement ranges from 20~ 40%. Drastic increase (2x) in j_{CO} was not obvious until high overpotential.

The formate production was only vigorous (~30%) at low overpotential (>-0.8 V vs. RHE). The presence of ligand mainly suppressed the reaction in the low overpotential except the increase on the Pd/C-Ami/SiO_2. The performance was altered at large overpotential where Pd/C-Ami/SiO_2 showed suppression while other ligands promote the formate production.

The production of methanol was not detected until -1.0V vs. RHE. Notably, up to 6x FE and 2 ~ 4x j_{CH3OH} was found with the Pd/C-Pyr-SiO_2 when compared with Pd/C. No significant improvement in methanol production was found with other composite catalyst sample. The pre-electrolysis electrolyte was taken as blank sample to make sure that the detected methanol are not the residual from silianization reactions.

In order to deconvolute the ligand effect from the effect form SiO_2 powder, ligand-free SiO_2 powder with Pd/C np was evaluated for the reactions. Figure 6.4 summarized comparation of catalytic performance in gas product. It can be found that the no statistically significant difference in catalytic performances were found with the presence of SiO_2 except CO production at -1.2 V vs. RHE.

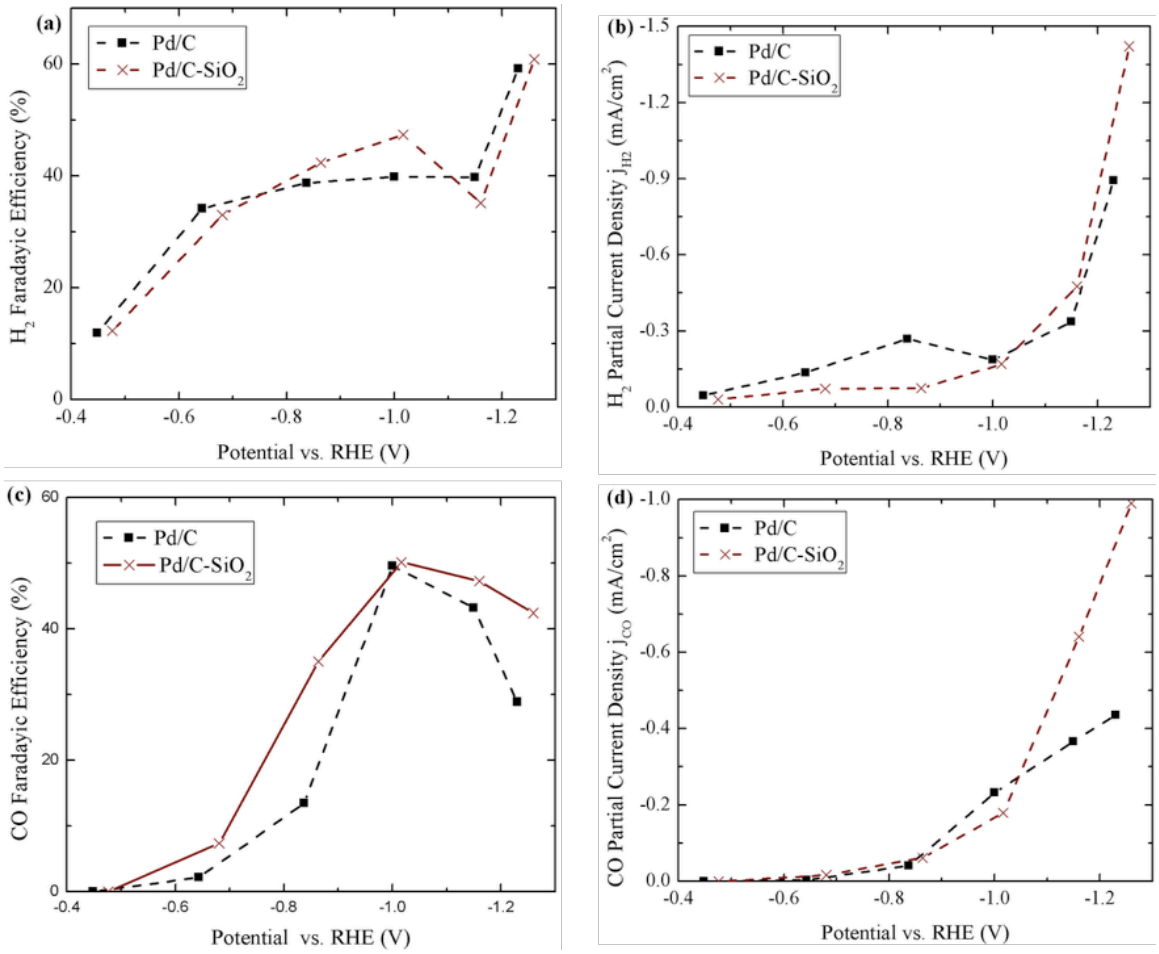

Figure 6.4. Comparison of product (H_2 and CO) partial current density and Faradaic efficiency (FE) for Pd/C and Pd/C with pure SiO2. (a) FE of H_2 formation, (b) partial current density of H_2 formation (c) FE of CO formation, (d) partial current density of CO formation

Figure 6.5 shows the LSV of the reactions that reached the same conclusion. Therefore, all the different catalytic performance can be attributed to the ligand without the interference from SiO_2.

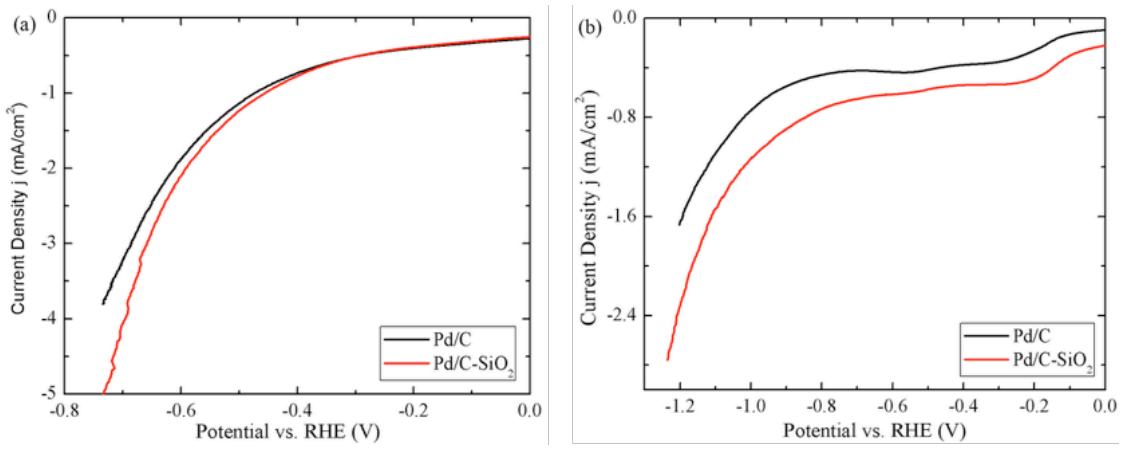

Figure 6.5. Comparison of LSV in (a) N_2 purged 0.1 M $KHCO_3$, (b) CO_2 purged 0.1M $KHCO_3$ on (SiO_2)-Pd/C

Each ligand evaluated in this work contains a nitrogen involved moiety that holds a lone pair of electrons. The Ace/SiO_2 and Ami/SiO_2 both have an amine group that is known for strong CO_2 absorption ability. It was reported[168] that the binding energy for secondary amine (Ace) is stronger than primary amine (Ami). The lone pair electrons on Pyr/SiO_2 is not in the aromatic ring so it holds chemical property similar to the tertiary amine which holds the strongest uptake for CO_2 absorption[169]. Therefore, the order for local concentration of CO_2 on all the composite catalyst here is: Pd/C -Pyr/SiO_2 > Pd/C-Ace/SiO_2> Pd/C-Ami/SiO_2 > Pd/C. The enhanced local CO_2 concentration will compete for the sites for proton adsorption and in return suppress all reactions involved surface proton (HER and HCOOH production). The reason that same trend was not found on the Pd/C-Ace/SiO_2 will be discussed from thermodynamic point of view later.

The pKa of the functional group are listed in the table 6.1 from which we can conclude the order for the available proton transfer ability from ligand is: Pd/C -Pyr/SiO_2 > Pd/C-Ami/SiO_2 > Pd/C-Ace/SiO_2.

Table 6.1. Summary of the pKas of functional groups

Functional group	pKa
Acetamido-	12.75
Amino-	9.7
Pyridyl-	5.2

Only on Pd/C -Pyr/SiO_2 did both CO_2 and proton concentration increased. Kinetically this should favor either CO2RR or HER or both. The enhancement in CO2RR is consistent with the experiment results that CO production enhanced in the entire potential range of interest. With the overwhelming CO* presence on the surface, the CO* could either desorb into gas phase CO or adopt a atop adsorption configuration to accommodate more CO*. The atop configuration apparently favors hydrogenation. At large overpotential, the 6-fold methanol production suggest that CO* on Pd is probably getting hydrogenated as was intended. However, detail mechanism is still unknown due to the lack of in situ spectroscopy experiment support.

The onset potentials for HER and CO2RR were extracted from the Tafel plots and summarized in the Table 6.2 to provide the insight in reaction mechanisms from thermodynamic point of view. The onset potentials for CO_2RR were all shifted anodically to certain extend on the composite catalysts. Same anodic shifts for HER were observed with an exception on Pd/C -Pyr/SiO_2. As was derived with Butler-Volmer equation in chapter 5, the difference in onset potential determines the relative selectivity between HER and CO2RR. When comparing the relative onset potentials, the lowest value was observed on the Pd/C-

Ace/SiO_2 which did show the prestigious for HER even with the lowest available proton concentration. The suppression for HER on Pd/C-Pyr/SiO_2 followed the trend. The unexpected suppression on Pd/C-Ami/SiO_2 was attributed to the limited available proton that cause the thermodynamic advantage being overwhelmed.

Table 6.2. Summary of onset potentials （vs. RHE） of HER and CO_2RR

Catalyst	HER	CO2RR	V_{HER}-V_{CO2RR}
Pd/C	-0.2	-0.07	-0.13
Pd/C-Ace/SiO_2	-0.04	-0.01	-0.03
Pd/C -Pyr/SiO_2	-0.26	0	-0.26
Pd/C-Ami/SiO_2	-0.14	-0.02	-0.12

Conclusion

The composite electrocatalyst Pd/C -Pyr/SiO_2 exhibited 6 times increase in faradaic efficiency and up to 4 times increase in partial current density for CH_3OH production. The engineered interface with ligand facilitated proton coupled electron transfer to the Pd nanoparticle appeared to be a plausible method for promoting hydrogenation in CO_2 reduction without the limitation from the scaling relationship. Further efforts are necessary to increase of population of interface.

CHAPTER 7. CONCLUSION

Electrochemical CO_2 reduction is a promising method for renewable fuel synthesis. The reduction products from CO_2 can range from HCOOH, CO, CH_3OH to C_2H_5OH, etc. The major challenge in making this process industrially viable is the reaction selectivity and energy efficiency. To date, extensive researches have studied cathode catalysts, the best catalyst produce CO selectively. As was analyzed in the introduction, the volumetric energy of liquid fuels are much higher than gas.

In nature, photosynthesis converts CO_2 to glucose with 100% selectivity with enzyme chemistry. To date, state of the art in engineering is far from this. The core idea of enzyme chemistry can be summarized by bimetallic alloy for proper intermediates binding, nanoscale cluster for atomistic precise active sites, and ligand facilitated proton coupled electron transfer. Selective catalysts can be engineered by combining the scheme from nature catalysis and the artificial controlled renewable power supply.

In this work, Au-Cu alloy, ligated Cu, and ligated Au were studied to explore the ligand effect initially. The product distribution shows dependency with the Au-Cu ratio in the alloy. The introduction of Au into Cu content tends to make the alloy a “super Au”. Au-Cu (50wt% Au) showed up to 5-fold increase in faradaic efficiency for CO evolution when compared with pure Cu.

Ligands with different functional moieties showed effect in product distribution on the Cu and Au surface. Glutathione increases the CO evolution. Contradictory effects were observed for 2-phenylethethiol on Cu and Au. The reactions no longer present on Cu but exhibited up to 7.6-fold increase in CO production on Au. Complementary computational

simulation suggests that the ligand reconstructs Au surface and creates active sites that favor the CO_2 reduction reaction over the competing hydrogen evolution reaction.

Further studies on ligated Au electrodes: such as carbolic group (2-Mercaptanproponic acid), pyridyl group (4-pyridylethylmercaptan), and the amine group (cysteamine) uncover the dependency of proton-coupled-electron transfer on the proton donation ability (pKa) of the functional moieties. Mild acidic ligand (4-PEM) is able to switch the selectivity from CO (gas product) to HCOOH (liquid product) through the ligand-facilitated-proton transfer. By transferring protons to the surface to favor the HCOO intermediate instead of -COOH for the CO production path, Faradaic efficiency and yield of HCOOH production was doubled and tripled, respectively and therefore increase the overall product volumetric energy density. However, HCOOH is not as valuable as alcohol products such as CH_3OH, which has to go through the COOH reduction path. That is to say, the ligand facilitated proton couple electron transfer is desired to happen to CO instead of CO_2.

Based on the knowledge from the initial study in ligand effect, the metal-ligand interfaces were engineered through the macro-composite catalyst, that is composed of Pd nanoclusters supported on carbon (Pd/C) and siloxane functionalized silica powder (4-Pyr/Si). Pd/C was chosen because of it's selective CO production and strong bonding with CO. With the engineered catalyst, up to 6-fold increase in CH_3OH was obtained compared with pure Pd/C. Though the absolute current density for CH_3OH is as low as $4\mu A/cm^2$, the engineering concept that utilizes the metal ligand interface was shown to be a plausible strategy.

In order to improve the production rate for scalable processes, the next stage for catalyst engineers should be to maximize the available interfaces thereby increasing the

active site population. Another strategy with microscopic composite catalyst is to deposit active metal center and proton transfer ligand on the same conductive supporting substrate.

In addition to this scheme, there are a few other strategies that can be approached for catalyst engineering such as other ligand or dual-ligand functionalization. Dual-ligand functionalization can implement either two functional moieties on the same ligand or two independent ligands. For example, one hydrophobic ligand reconstructs the surface for active sites where the metal center has to be capable of CO production and stabilization (the hydrophobicity character can prevent proton adsorption to the surface), with the other ligand facilitates the near surface proton transfer to CO.

Ligand chemistry guided by mother nature, relaxing at least one degree of freedom, is a powerful tool in electrocatalysis engineering.

REFERENCES

1. Andrews, E.; Fang, Y.; Flake, J., *J. Appl. Electrochem.* **2018,** *48*, 435-441.

2. Fang, Y.; Flake, J. C., *J. Am. Chem. Soc.* **2017,** *139*, 3399-3405.

3. Fang, Y.; Flake, J., *ECS Transactions* **2018,** *85*, 1025-1029.

4. Levelized Cost and Levelized Avoided Cost of New Generation Resources in the Annual Energy Outlook 2018. U.S. Energy Information Administration: 2018.

5. MHI Completes Installation of CO2 Capture Unit at Nippon Ekitan's Mizushima Plant -- Recovery Capacity of 283 Metric Tons per Day for New Liquefied Gas Production Facility --. Mitsubishi Heavy Industries: 2017.

6. Royer, E., *CR Acad Sci* **1870,** *70*, 731-735.

7. Yoshio Hori, A. M., Katsuhei Kikuchi, Shin Suzuki, *J. Chem. Soc., Chem. Commun.* **1987**, 728-729.

8. Hori, Y.; Kikuchi, K.; Suzuki, S., *Chem. Lett.* **1985,** *14*, 1695-1698.

9. Hori, Y.; Murata, A.; Takahashi, R., *J. Chem. Soc., Faraday Trans. 1* **1989,** *85*, 2309-2326.

10. Wu, J.; Huang, Y.; Ye, W.; Li, Y., *Advanced Science* **2017,** *4*, 1700194-n/a.

11. Andrew A. Peterson, F. A.-P., Felix Studt, Jan Rossmeisl and Jens K. Nørskov, *Energy Environ. Sci.* **2010**, 1311–1315.

12. Billy, J. T.; Co, A. C., *ACS Catal.* **2017,** *7*, 8467-8479.

13. Ma, S.; Luo, R.; Moniri, S.; Lan, Y.; Kenis, P. J., *J. Electrochem. Soc.* **2014,** *161*, F1124-F1131.

14. Wu, J.; Risalvato, F. G.; Sharma, P. P.; Pellechia, P. J.; Ke, F.-S.; Zhou, X.-D., *J. Electrochem. Soc.* **2013,** *160*, F953-F957.

15. Lister, T. E.; Dufek, E. J., *Energy & Fuels* **2013,** *27*, 4244-4249.

16. Whipple, D. T.; Finke, E. C.; Kenis, P. J. A., *Electrochem. Solid-State Lett.* **2010,** *13*, B109-B111.

17. Verma, S.; Lu, X.; Ma, S.; Masel, R. I.; Kenis, P. J. A., *Phys. Chem. Chem. Phys.* **2016**.

18. Singh, M. R.; Kwon, Y.; Lum, Y.; Ager, J. W.; Bell, A. T., *J. Am. Chem. Soc.* **2016,** *138*, 13006-13012.

19. Rosen, B. A.; Salehi-Khojin, A.; Thorson, M. R.; Zhu, W.; Whipple, D. T.; Kenis, P. J.; Masel, R. I., *Science* **2011,** *334*, 643-644.

20. Hori, Y., Vayenas, C.; White, R.; Gamboa-Aldeco, M., Eds. Springer New York: 2008; Vol. 42, pp 89-189.

21. Jia, F.; Yu, X.; Zhang, L., *J. Power Sources* **2014,** *252*, 85-89.

22. Ishimaru, S.; Shiratsuchi, R.; Nogami, G., *J. Electrochem. Soc.* **2000,** *147*, 1864-1867.

23. Ren, D.; Ang, B. S.-H.; Yeo, B. S., *ACS Catal.* **2016,** *6*, 8239-8247.

24. Chen, D.; Yao, Q.; Cui, P.; Liu, H.; Xie, J.; Yang, J., *ACS Applied Energy Materials* **2018,** *1*, 883-890.

25. Bi, W.; Li, X.; You, R.; Chen, M.; Yuan, R.; Huang, W.; Wu, X.; Chu, W.; Wu, C.; Xie, Y., *Adv. Mater.* **2018,** *30*, 1706617.

26. Shi, J.; Shao, D.; Zhang, J.; Tan, D.; Tan, X.; Zhang, B.; Han, B.; Zhang, F.; Liu, L.; Cheng, X., *Chem. Commun.* **2018,** *54*, 5450-5453.

27. Zhang, W.; Qin, Q.; Dai, L.; Qin, R.; Zhao, X.; Chen, X.; Ou, D.; Chen, J.; Chuong, T. T.; Wu, B.; Zheng, N., *Angew. Chem. Int. Ed.* **2018,** *57*, 9475-9479.

28. Hori, Y.; Takahashi, I.; Koga, O.; Hoshi, N., *The Journal of Physical Chemistry B* **2002,** *106*, 15-17.

29. Kuhl, K. P.; Cave, E. R.; Abram, D. N.; Jaramillo, T. F., *Energy Environ. Sci.* **2012,** *5*, 7050-7059.

30. Schouten, K.; Kwon, Y.; Van der Ham, C.; Qin, Z.; Koper, M., *Chemical Science* **2011,** *2*, 1902-1909.

31. Hori, Y.; Murata, A.; Takahashi, R.; Suzuki, S., *J. Am. Chem. Soc.* **1987,** *109*, 5022-5023.

32. Kapusta, S.; Hackerman, N., *J. Electrochem. Soc.* **1983,** *130*, 607-613.

33. Hori, Y.; Murata, A.; Tsukamoto, T.; Wakebe, H.; Koga, O.; Yamazaki, H., *Electrochim. Acta* **1994,** *39*, 2495-2500.

34. Hori, Y.; Wakebe, H.; Tsukamoto, T.; Koga, O., *Surf. Sci.* **1995,** *335*, 258-263.

35. Anfuso, C. L.; Ricks, A. M.; Rodríguez-Córdoba, W.; Lian, T., *The Journal of Physical Chemistry C* **2012,** *116*, 26377-26384.

36. Feaster, J. T.; Shi, C.; Cave, E. R.; Hatsukade, T.; Abram, D. N.; Kuhl, K. P.; Hahn, C.; Nørskov, J. K.; Jaramillo, T. F., *ACS Catal.* **2017,** *7*, 4822-4827.

37. Nie, X.; Esopi, M. R.; Janik, M. J.; Asthagiri, A., *Angew. Chem. Int. Ed.* **2013,** *52*, 2459-2462.

38. Peterson, A. A.; Nørskov, J. K., *J. Phys. Chem. Lett.* **2012,** *3*, 251-258.

39. Shi, C.; Hansen, H. A.; Lausche, A. C.; Nørskov, J. K., *Phys. Chem. Chem. Phys.* **2014,** *16*, 4720-4727.

40. Watanabe, M.; Shibata, M.; Kato, A.; Azuma, M.; Sakata, T., *J. Electrochem. Soc.* **1991,** *138*, 3382-3389.

41. Kim, D.; Resasco, J.; Yu, Y.; Asiri, A. M.; Yang, P., *Nature Communications* **2014,** *5*, 4948.

42. Ma, S.; Sadakiyo, M.; Heima, M.; Luo, R.; Haasch, R. T.; Gold, J. I.; Yamauchi, M.; Kenis, P. J. A., *J. Am. Chem. Soc.* **2017,** *139*, 47-50.

43. Kauffman, D. R.; Alfonso, D.; Matranga, C.; Qian, H.; Jin, R., *J. Am. Chem. Soc.* **2012,** *134*, 10237-10243.

44. Zhu, W.; Michalsky, R.; Metin, Ö.; Lv, H.; Guo, S.; Wright, C. J.; Sun, X.; Peterson, A. A.; Sun, S., *J. Am. Chem. Soc.* **2013,** *135*, 16833-16836.

45. Zhu, W.; Zhang, Y.-J.; Zhang, H.; Lv, H.; Li, Q.; Michalsky, R.; Peterson, A. A.; Sun, S., *J. Am. Chem. Soc.* **2014,** *136*, 16132-16135.

46. Yang, Y.; Evans, J.; Rodriguez, J. A.; White, M. G.; Liu, P., *Phys. Chem. Chem. Phys.* **2010,** *12*, 9909-9917.

47. Le, M.; Ren, M.; Zhang, Z.; Sprunger, P. T.; Kurtz, R. L.; Flake, J. C., *J. Electrochem. Soc.* **2011,** *158*, E45-E49.

48. Li, C. W.; Kanan, M. W., *J. Am. Chem. Soc.* **2012,** *134*, 7231-7234.

49. Chen, Y.; Li, C. W.; Kanan, M. W., *J. Am. Chem. Soc.* **2012,** *134*, 19969-19972.

50. Yacoby, I.; Pochekailov, S.; Toporik, H.; Ghirardi, M. L.; King, P. W.; Zhang, S., *Proc. Natl. Acad. Sci. U.S.A* **2011,** *108*, 9396-9401.

51. Gross, E. L., *Photosynth. Res.* **1993,** *37*, 103-116.

52. Hansen, H. A.; Varley, J. B.; Peterson, A. A.; Nørskov, J. K., *J. Phys. Chem. Lett* **2013,** *4*, 388-392.

53. Jhong, H.-R. M.; Ma, S.; Kenis, P. J. A., *Curr. Opin. Chem. Eng.* **2013,** *2*, 191-199.

54. Kauffman, D. R.; Alfonso, D.; Matranga, C.; Qian, H.; Jin, R., *J. Am. Chem. Soc.* **2012,** *134*, 10237-10243.

55. Manthiram, K.; Beberwyck, B. J.; Alivisatos, A. P., *J. Am. Chem. Soc.* **2014,** *136*, 13319-13325.

56. Andrews, E.; Katla, S.; Kumar, C.; Patterson, M.; Sprunger, P.; Flake, J., *J. Electrochem. Soc.* **2015,** *162*, F1373-F1378.

57. Seshadri, G.; Lin, C.; Bocarsly, A. B., *J. Electroanal. Chem.* **1994,** *372*, 145-150.

58. Zhang, Y.-J.; Sethuraman, V.; Michalsky, R.; Peterson, A. A., *ACS Catal.* **2014,** *4*, 3742-3748.

59. Christophe, J.; Doneux, T.; Buess-Herman, C., *Electrocatalysis* **2012,** *3*, 139-146.

60. Wu, Z.; Suhan, J.; Jin, R., *J. Mater. Chem.* **2009,** *19*, 622-626.

61. Zhu, M.; Lanni, E.; Garg, N.; Bier, M. E.; Jin, R., *J. Am. Chem. Soc.* **2008,** *130*, 1138-1139.

62. Younkin, T. R.; Connor, E. F.; Henderson, J. I.; Friedrich, S. K.; Grubbs, R. H.; Bansleben, D. A., *Science* **2000,** *287*, 460-462.

63. Xie, M.; Xia, B. Y.; Li, Y.; Yan, Y.; Yang, Y.; Sun, Q.; Chan, S. H.; Fisher, A. C.; Wang, X., *Energy Environ. Sci.* **2016,** *9*, 1687-1695.

64. Rochelle, G. T., *Science* **2009,** *325*, 1652-1654.

65. Bieri, M.; Burgi, T., *Phys. Chem. Chem. Phys.* **2006,** *8*, 513-520.

66. Socrates, G., John Wiley & Sons: 2004.

67. Bieri, M.; Bürgi, T., *Langmuir* **2005,** *21*, 1354-1363.

68. Badawi, H. M., *Spectrochim. Acta A* **2011,** *82*, 63-68.

69. Farrag, M.; Tschurl, M.; Dass, A.; Heiz, U., *Phys. Chem. Chem. Phys.* **2013,** *15*, 12539-12542.

70. Wang, Q.; Li, N., *Electroanalysis* **2001,** *13*, 1375-1377.

71. Yang, W.-h.; Li, W.-w.; Dou, H.-j.; Sun, K., *Mater. Lett.* **2008,** *62*, 2564-2566.

72. Jacob, J. D. C.; Lee, T. R.; Baldelli, S., *J. Phys. Chem. C* **2014,** *118*, 29126-29134.

73. Yan, Y.; Ge, X.; Liu, Z.; Wang, J.-Y.; Lee, J.-M.; Wang, X., *Nanoscale* **2013,** *5*, 7768-7771.

74. Marshall, G. M.; Bensebaa, F.; Dubowski, J. J., *J. Appl. Phys.* **2009,** *105*, 094310.

75. Gordon, W. O.; Xu, Y.; Mullins, D. R.; Overbury, S. H., *Phys. Chem. Chem. Phys.* **2009,** *11*, 11171-11183.

76. Sim, W. S.; Gardner, P.; King, D. A., *J. Phys. Chem.* **1996,** *100*, 12509-12516.

77. Miller, F. A.; Wilkins, C. H., *Anal. Chem.* **1952,** *24*, 1253-1294.

78. Houtman, C. J.; Brown, N. F.; Barteau, M. A., *J. Catal.* **1994,** *145*, 37-53.

79. Garcia, A. R.; da Silva, J. L.; Ilharco, L. M., *Surf. Sci.* **1998,** *415*, 183-193.

80. Calaza, F. C.; Chen, T.-L.; Mullins, D. R.; Xu, Y.; Overbury, S. H., *Catal. Today* **2015,** *253*, 65-76.

81. Maksymovych, P.; Voznyy, O.; Dougherty, D. B.; Sorescu, D. C.; Yates Jr, J. T., *Prog. Surf. Sci.* **2010,** *85*, 206-240.

82. Yang, G.; Liu, G.-y., *J. Phys. Chem. B* **2003,** *107*, 8746-8759.

83. Marshall, S. T.; O'Brien, M.; Oetter, B.; Corpuz, A.; Richards, R. M.; Schwartz, D. K.; Medlin, J. W., *Nat. Mater* **2010,** *9*, 853-858.

84. Back, S.; Kim, H.; Jung, Y., *ACS Catal.* **2015,** *5*, 965-971.

85. Alfonsoa, D. R., Kauffman,Douglas, Matranga,Christopher, *The Journal of Chemical Physics* **2016,** *144*, 184705.

86. Zhang, J.; Chi; Ulstrup, J., *Langmuir* **2006,** *22*, 6203-6213.

87. Pensa, E.; Carro, P.; Rubert, A. A.; Benítez, G.; Vericat, C.; Salvarezza, R. C., *Langmuir* **2010,** *26*, 17068-17074.

88. Dakkouri, A. S.; Kolb, D. M.; Edelstein-Shima, R.; Mandler, D., *Langmuir* **1996,** *12*, 2849-2852.

89. Tao, Y.-T.; Wu, C.-C.; Eu, J.-Y.; Lin, W.-L.; Wu, K.-C.; Chen, C.-h., *Langmuir* **1997,** *13*, 4018-4023.

90. Whelan, C. M.; Smyth, M. R.; Barnes, C. J., *Langmuir* **1999,** *15*, 116-126.

91. Sawaguchi, T.; Mizutani, F.; Yoshimoto, S.; Taniguchi, I., *Electrochim. Acta* **2000,** *45*, 2861-2867.

92. Uosaki, K., *Chem. Rec.* **2009,** *9*, 199-209.

93. Biener, M. M.; Biener, J.; Friend, C. M., *Surf. Sci.* **2007,** *601*, 1659-1667.

94. Wöll, C.; Chiang, S.; Wilson, R. J.; Lippel, P. H., *Phys. Rev. B* **1989,** *39*, 7988-7991.

95. Barth, J. V.; Brune, H.; Ertl, G.; Behm, R. J., *Phys. Rev. B* **1990,** *42*, 9307-9318.

96. Min, B. K.; Alemozafar, A. R.; Biener, M. M.; Biener, J.; Friend, C. M., *Top. Catal.* **2005,** *36*, 77-90.

97. Schweizer, M.; Hagenström, H.; Kolb, D. M., *Surf. Sci.* **2001,** *490*, L627-L636.

98. Li, F.-S.; Zhou, W.; Guo, Q., *Phys. Rev. B* **2009,** *79*, 113412.

99. Whelan, C. M.; Smyth, M. R.; Barnes, C. J., *J. Electroanal. Chem.* **1998,** *441*, 109-129.

100. Dodero, G.; De Michieli, L.; Cavalleri, O.; Rolandi, R.; Oliveri, L.; Daccà, A.; Parodi, R., *Colloids Surf. A* **2000,** *175*, 121-128.

101. Kühnle, A.; Linderoth, T. R.; Schunack, M.; Besenbacher, F., *Langmuir* **2006,** *22*, 2156-2160.

102. Poirier, G. E., *Chem. Rev.* **1997,** *97*, 1117-1128.

103. Kautz, N. A.; Kandel, S. A., *J. Am. Chem. Soc.* **2008,** *130*, 6908-6909.

104. Sheppard, D. C.; Parkinson, G. S.; Hentz, A.; Window, A. J.; Quinn, P. D.; Woodruff, D. P.; Bailey, P.; Noakes, T. C. Q., *Surf. Sci.* **2011,** *605*, 138-145.

105. Maksymovych, P.; Voznyy, O.; Dougherty, D. B.; Sorescu, D. C.; Yates, J. T., *Prog. Surf. Sci.* **2010,** *85*, 206-240.

106. Sheppard, D. C.; Parkinson, G. S.; Hentz, A.; Window, A. J.; Quinn, P. D.; Woodruff, D. P.; Bailey, P.; Noakes, T. C. Q., *Surf. Sci.* **2011,** *605*, 138-145.

107. Ryu, S.; Kang, J.-W.; Han, Y.-K.; Lee, Y.-S., *Bull. Korean Chem. Soc.* **2011,** *32*, 3614-3617.

108. Hu, G.; Jin, R.; Jiang, D.-e., *Nanoscale* **2016,** *8*, 20103-20110.

109. Zeng, Z.; Greeley, J., *Catal. Commun.* **2014,** *52*, 78-83.

110. Shin, H.; Ha, Y.; Kim, H., *J. Phys. Chem. Lett* **2016,** *7*, 4124-4129.

111. Rosen, J.; Hutchings, G. S.; Lu, Q.; Rivera, S.; Zhou, Y.; Vlachos, D. G.; Jiao, F., *ACS Catal.* **2015,** *5*, 4293-4299.

112. Chen, L. D.; Urushihara, M.; Chan, K.; Nørskov, J. K., *ACS Catal.* **2016,** *6*, 7133-7139.

113. Nørskov, J. K.; Rossmeisl, J.; Logadottir, A.; Lindqvist, L.; Kitchin, J. R.; Bligaard, T.; Jónsson, H., *J. Phys. Chem. B* **2004,** *108*, 17886-17892.

114. Shaikhutdinov, S. K.; Meyer, R.; Naschitzki, M.; Bäumer, M.; Freund, H.-J., *Catal. Lett.* **2003,** *86*, 211-219.

115. McKee, W. C.; Patterson, M. C.; Huang, D.; Frick, J. R.; Kurtz, R. L.; Sprunger, P. T.; Liu, L.; Xu, Y., *J. Phys. Chem. C* **2016,** *120*, 10909-10918.

116. Tang, W.; Sanville, E.; Henkelman, G., *J. Phys.: Condens. Matter* **2009,** *21*, 084204.

117. Barile, C. J.; Tse, E. C. M.; Li, Y.; Sobyra, T. B.; Zimmerman, S. C.; Hosseini, A.; Gewirth, A. A., *Nat. Mater* **2014,** *13*, 619.

118. Zhangquan, P.; Yuhui, C.; G., B. P.; Ye, X., *Angew. Chem. Int. Ed.* **2015,** *54*, 8165-8168.

119. Barton Cole, E.; Lakkaraju, P. S.; Rampulla, D. M.; Morris, A. J.; Abelev, E.; Bocarsly, A. B., *J. Am. Chem. Soc.* **2010,** *132*, 11539-11551.

120. Morris, A. J.; McGibbon, R. T.; Bocarsly, A. B., *ChemSusChem* **2011,** *4*, 191-196.

121. Barton Cole, E.; Baruch, M.; L'Esperance, R.; Kelly, M.; Lakkaraju, P.; Zeitler, E.; Bocarsly, A., *Top. Catal.* **2015,** *58*, 15-22.

122. Xiang, D.; Magana, D.; Dyer, R. B., *J. Am. Chem. Soc.* **2014,** *136*, 14007-14010.

123. Rouhana, L. L.; Moussallem, M. D.; Schlenoff, J. B., *J. Am. Chem. Soc.* **2011,** *133*, 16080-16091.

124. Buck, M.; Grunze, M.; Eisert, F.; Fischer, J.; Träger, F., *Journal of Vacuum Science & Technology A* **1992,** *10*, 926-929.

125. Martínez, L.; Carrascosa, L. G.; Huttel, Y.; Lechuga, L. M.; Román, E., *Phys. Chem. Chem. Phys.* **2010,** *12*, 3301-3308.

126. Liu, J., 2010.

127. Manolova, M.; Ivanova, V.; Kolb, D. M.; Boyen, H. G.; Ziemann, P.; Büttner, M.; Romanyuk, A.; Oelhafen, P., *Surf. Sci.* **2005,** *590*, 146-153.

128. Kim, S. K.; Zhang, Y.-J.; Bergstrom, H.; Michalsky, R.; Peterson, A., *ACS Catal.* **2016,** *6*, 2003-2013.

129. Bard, A. J.; Faulkner, L. R.; Leddy, J.; Zoski, C. G., Wiley New York: 1980; Vol. 2.

130. Davis, M. E.; Davis, R. J., Courier Corporation: 2012.

131. Thorson, M. R.; Siil, K. I.; Kenis, P. J. A., *J. Electrochem. Soc.* **2013,** *160*, F69-F74.

132. Cannan, R. K.; Knight, B. C. J. G., *Biochem. J* **1927,** *21*, 1384-1390.

133. Pure, I. U. o.; Data, A. C. C. o. E.; Serjeant, E. P.; Dempsey, B.; Pure, I. U. o.; Data, A. C. C. o. E., Pergamon Press: 1979.

134. Ngunjiri, J. N.; Vegunta, S. S.; Flake, J. C., *J. Electrochem. Soc.* **2009,** *156*, H516-H521.

135. Widrig, C. A.; Chung, C.; Porter, M. D., *Journal of Electroanalytical Chemistry and Interfacial Electrochemistry* **1991,** *310*, 335-359.

136. Byloos, M.; Al-Maznai, H.; Morin, M., *The Journal of Physical Chemistry B* **2001,** *105*, 5900-5905.

137. Muglali, M. I.; Erbe, A.; Chen, Y.; Barth, C.; Koelsch, P.; Rohwerder, M., *Electrochim. Acta* **2013,** *90*, 10.1016/j.electacta.2012.11.116.

138. Srisombat, L.; Jamison, A. C.; Lee, T. R., *Colloids Surf. A* **2011,** *390*, 1-19.

139. Swoboda, A.; Kunze, G., *Clays Clay Miner.* **1966**, 277-88.

140. Cukier, R. I.; Nocera, D. G., *Annu. Rev. Phys. Chem.* **1998,** *49*, 337-369.

141. Weinberg, D. R.; Gagliardi, C. J.; Hull, J. F.; Murphy, C. F.; Kent, C. A.; Westlake, B. C.; Paul, A.; Ess, D. H.; McCafferty, D. G.; Meyer, T. J., *Chem. Rev.* **2012,** *112*, 4016-4093.

142. Reece, S. Y.; Hodgkiss, J. M.; Stubbe, J.; Nocera, D. G., *Philosophical Transactions of the Royal Society B: Biological Sciences* **2006,** *361*, 1351-1364.

143. Xiao, Y.; Patolsky, F.; Katz, E.; Hainfeld, J. F.; Willner, I., *Science* **2003,** *299*, 1877-1881.

144. Mano, N.; Fernandez, J. L.; Kim, Y.; Shin, W.; Bard, A. J.; Heller, A., *J. Am. Chem. Soc.* **2003,** *125*, 15290-15291.

145. Heller, A., *The Journal of Physical Chemistry* **1992,** *96*, 3579-3587.

146. Sirés, I.; Delucchi, M.; Panizza, M.; Ricotti, R.; Cerisola, G., *J. Appl. Electrochem.* **2009,** *39*, 2275.

147. Fernández, J. L.; Mano, N.; Heller, A.; Bard, A. J., *Angew. Chem. Int. Ed.* **2004,** *43*, 6355-6357.

148. Keith, J. A.; Carter, E. A., *J. Am. Chem. Soc.* **2012,** *134*, 7580-7583.

149. Keith, J. A.; Carter, E. A., *Chemical Science* **2013,** *4*, 1490-1496.

150. Keith, J. A.; Carter, E. A., *J. Phys. Chem. Lett.* **2013,** *4*, 4058-4063.

151. Ertem, M. Z.; Konezny, S. J.; Araujo, C. M.; Batista, V. S., *J. Phys. Chem. Lett.* **2013,** *4*, 745-748.

152. Li, T. T. T.; Weaver, M. J., *J. Am. Chem. Soc.* **1984,** *106*, 6107-6108.

153. Feaster, J. In *Understanding Selectivity of Carbon Dioxide Reduction to Carbon Monoxide and Formic Acid on Sn Electrodes*, PRiME 2016/230th ECS Meeting (October 2-7, 2016), Ecs: 2016.

154. Vaidhyanathan, R.; Iremonger, S. S.; Shimizu, G. K. H.; Boyd, P. G.; Alavi, S.; Woo, T. K., *Science* **2010,** *330*, 650-653.

155. Wagner, N.; Gülzow, E., *J. Power Sources* **2004,** *127*, 341-347.

156. Collman, J. P.; Brauman, J. I.; Halbert, T. R.; Suslick, K. S., *Proc. Natl. Acad. Sci. U.S.A* **1976,** *73*, 3333.

157. Falconer, J. L.; Zağli, A. E., *J. Catal.* **1980,** *62*, 280-285.

158. Hori, Y.; Wakebe, H.; Tsukamoto, T.; Koga, O., *Electrochim. Acta* **1994,** *39*, 1833-1839.

159. Min, X.; Kanan, M. W., *J. Am. Chem. Soc.* **2015,** *137*, 4701-4708.

160. Gao, D.; Zhou, H.; Wang, J.; Miao, S.; Yang, F.; Wang, G.; Wang, J.; Bao, X., *J. Am. Chem. Soc.* **2015,** *137*, 4288-4291.

161. Cai, F.; Gao, D.; Zhou, H.; Wang, G.; He, T.; Gong, H.; Miao, S.; Yang, F.; Wang, J.; Bao, X., *Chemical Science* **2017,** *8*, 2569-2573.

162. Culler, S. R.; Ishida, H.; Koenig, J. L., *J. Colloid Interface Sci.* **1985,** *106*, 334-346.

163. Trasatti, S.; Petrii, O., *Pure Appl. Chem.* **1991,** *63*, 711-734.

164. Mitchell, M. B., American Chemical Society: 1993; Vol. 236, pp 351-375.

165. Falk, M.; Smith, D. G.; McLachlan, J.; McInnes, A. G., *Can. J. Chem.* **1966,** *44*, 2269-2281.

166. Shibata, M.; Horie, R.; Yoneta, W., *Polymer* **2010,** *51*, 5764-5770.

167. Palimi, M. J.; Rostami, M.; Mahdavian, M.; Ramezanzadeh, B., *Appl. Surf. Sci.* **2014,** *320*, 60-72.

168. Arstad, B.; Blom, R.; Swang, O., *The Journal of Physical Chemistry A* **2007,** *111*, 1222-1228.

169. Sartori, G.; Savage, D. W., *Industrial & Engineering Chemistry Fundamentals* **1983,** *22*, 239-249.

APPENDIX. LETTERS OF PERMISSION

様式 2

COPYRIGHT PERMISSION REQUEST FORM

Date: 08-16-2018

To: The Chemical Society of Japan
1-5,Kanda-Surugadai,Chiyoda-ku,
Tokyo 101-8307, Japan
Fax: +81-3-3292-6318
E-mail: info@chemistry.or.jp

From: Yuxin Fang
Phone: (573)-823-3179
Fax:
E-mail: yfang16@lsu.edu

I am preparing a paper entitled: Engineering Metal-ligand interface for selective electrochemical CO2 reduction

to appear in
my dissertation

which is published by
Louisiana State University

Expected publication date: December 2018

I request your permission to include the following material in this and in all subsequent editions of this work to be published by Louisiana State University or its licensees for distribution throughout the world, in all media including electronic/online and microfilm.

CL Title of Publication: PRODUCTION OF CO AND CH4 IN ELECTROCHEMICAL REDUCTION OF CO2 AT METAL ELECTRODES IN AQUEOUS HYDROGENCARBONATE SOLUTION

Author(s)/Editor(s): Yoshio HORI,* Katsuhei KIKUCHI, and Shin SUZUKI

Title of Selection:

Year: 1985 Vol.: 14 No.:

Figure(s)/Table(s): Table 1 Page(s): 1697

We hereby grant permission for the use of the material requested above.

Shinichi Suzuki

Shin-ichi Suzuki
Secretary-general
The Chemical Society of Japan

Date: August 17, 2018

Our Ref. No. CY-RT 18-133

SPRINGER NATURE LICENSE
TERMS AND CONDITIONS

Aug 02, 2018

This Agreement between Louisiana State University -- Yuxin Fang ("You") and Springer Nature ("Springer Nature") consists of your license details and the terms and conditions provided by Springer Nature and Copyright Clearance Center.

License Number	4400860681184
License date	Aug 02, 2018
Licensed Content Publisher	Springer Nature
Licensed Content Publication	Springer eBook
Licensed Content Title	Electrochemical CO2 Reduction on Metal Electrodes
Licensed Content Author	Y. Hori
Licensed Content Date	Jan 1, 2008
Type of Use	Thesis/Dissertation
Requestor type	academic/university or research institute
Format	print and electronic
Portion	figures/tables/illustrations
Number of figures/tables/illustrations	1
Will you be translating?	no
Circulation/distribution	<501
Author of this Springer Nature content	no
Title	Research Assistant
Instructor name	John C. Flake
Institution name	Louisiana State University
Expected presentation date	Sep 2018
Portions	Table 4
Requestor Location	Louisiana State University S. Stadium Dr. BATON ROUGE, LA 70803 United States Attn: Yuxin Fang
Billing Type	Invoice
Billing Address	Louisiana State University

JOHN WILEY AND SONS LICENSE TERMS AND CONDITIONS

Aug 02, 2018

This Agreement between Louisiana State University -- Yuxin Fang ("You") and John Wiley and Sons ("John Wiley and Sons") consists of your license details and the terms and conditions provided by John Wiley and Sons and Copyright Clearance Center.

License Number	4400860202163
License date	Aug 02, 2018
Licensed Content Publisher	John Wiley and Sons
Licensed Content Publication	Angewandte Chemie
Licensed Content Title	Selectivity of CO2 Reduction on Copper Electrodes: The Role of the Kinetics of Elementary Steps
Licensed Content Author	Xiaowa Nie, Monica R. Esopi, Michael J. Janik, et al
Licensed Content Date	Jan 23, 2013
Licensed Content Volume	125
Licensed Content Issue	9
Licensed Content Pages	4
Type of use	Dissertation/Thesis
Requestor type	University/Academic
Format	Print and electronic
Portion	Figure/table
Number of figures/tables	1
Original Wiley figure/table number(s)	Scheme 1
Will you be translating?	No
Title of your thesis / dissertation	Research Assistant
Expected completion date	Sep 2018
Expected size (number of pages)	1
Requestor Location	Louisiana State University S. Stadium Dr. BATON ROUGE, LA 70803 United States Attn: Yuxin Fang
Publisher Tax ID	EU826007151

Copyright Clearance Center

Confirmation Number: 11739743
Order Date: 08/15/2018

Customer Information

Customer: Yuxin Fang
Account Number: 3001316899
Organization: Louisiana State University
Email: yfang16@lsu.edu
Phone: +1 (573) 823-3179
Payment Method: Invoice

This is not an invoice

Order Details

Physical chemistry chemical physics

Billing Status: **N/A**

Order detail ID:	71443965
ISSN:	1463-9084
Publication Type:	e-Journal
Volume:	
Issue:	
Start page:	
Publisher:	ROYAL SOCIETY OF CHEMISTRY
Author/Editor:	Royal Society of Chemistry (Great Britain)

Permission Status: **Granted**

Permission type: Republish or display content
Type of use: Thesis/Dissertation
Order License Id: 4410490830505

Requestor type	Academic institution
Format	Print, Electronic
Portion	chart/graph/table/figure
Number of charts/graphs/tables/figures	2
The requesting person/organization	Yuxin Fang/Louisiana State University
Title or numeric reference of the portion(s)	Fig 4, Fig 5
Title of the article or chapter the portion is from	Trends in electrochemical CO2 reduction activity for open and close-packed metal surfaces
Editor of portion(s)	N/A
Author of portion(s)	Chuan Shi, Heine A. Hansen,a Adam C. Lauscheb and Jens K. Nørskov
Volume of serial or monograph	N/A
Page range of portion	4725-4726
Publication date of portion	16th January 2014

SPRINGER NATURE LICENSE
TERMS AND CONDITIONS

Aug 02, 2018

This Agreement between Louisiana State University -- Yuxin Fang ("You") and Springer Nature ("Springer Nature") consists of your license details and the terms and conditions provided by Springer Nature and Copyright Clearance Center.

License Number	4400850535105
License date	Aug 02, 2018
Licensed Content Publisher	Springer Nature
Licensed Content Publication	Journal of Applied Electrochemistry
Licensed Content Title	Electrochemical reduction of CO2 at CuAu nanoparticles: size and alloy effects
Licensed Content Author	Evan Andrews, Yuxin Fang, John Flake
Licensed Content Date	Jan 1, 2018
Licensed Content Volume	48
Licensed Content Issue	4
Type of Use	Thesis/Dissertation
Requestor type	non-commercial (non-profit)
Format	print and electronic
Portion	full article/chapter
Will you be translating?	no
Circulation/distribution	<501
Author of this Springer Nature content	yes
Title	Research Assistant
Instructor name	John C. Flake
Institution name	Louisiana State University
Expected presentation date	Sep 2018
Requestor Location	Louisiana State University S. Stadium Dr. BATON ROUGE, LA 70803 United States Attn: Yuxin Fang
Billing Type	Invoice
Billing Address	Louisiana State University

S. Stadium Dr.

BATON ROUGE, LA 70803
United States
Attn: Yuxin Fang

Total 0.00 USD

Terms and Conditions

Springer Nature Terms and Conditions for RightsLink Permissions

Springer Customer Service Centre GmbH (the Licensor) hereby grants you a non-exclusive, world-wide licence to reproduce the material and for the purpose and requirements specified in the attached copy of your order form, and for no other use, subject to the conditions below:

1. The Licensor warrants that it has, to the best of its knowledge, the rights to license reuse of this material. However, you should ensure that the material you are requesting is original to the Licensor and does not carry the copyright of another entity (as credited in the published version).

   If the credit line on any part of the material you have requested indicates that it was reprinted or adapted with permission from another source, then you should also seek permission from that source to reuse the material.

2. Where **print only** permission has been granted for a fee, separate permission must be obtained for any additional electronic re-use.

3. Permission granted **free of charge** for material in print is also usually granted for any electronic version of that work, provided that the material is incidental to your work as a whole and that the electronic version is essentially equivalent to, or substitutes for, the print version.

4. A licence for 'post on a website' is valid for 12 months from the licence date. This licence does not cover use of full text articles on websites.

5. Where **'reuse in a dissertation/thesis'** has been selected the following terms apply: Print rights for up to 100 copies, electronic rights for use only on a personal website or institutional repository as defined by the Sherpa guideline (www.sherpa.ac.uk/romeo/).

6. Permission granted for books and journals is granted for the lifetime of the first edition and does not apply to second and subsequent editions (except where the first edition permission was granted free of charge or for signatories to the STM Permissions Guidelines http://www.stm-assoc.org/copyright-legal-affairs/permissions/permissions-guidelines/), and does not apply for editions in other languages unless additional translation rights have been granted separately in the licence.

7. Rights for additional components such as custom editions and derivatives require additional permission and may be subject to an additional fee. Please apply to Journalpermissions@springernature.com/bookpermissions@springernature.com for these rights.

8. The Licensor's permission must be acknowledged next to the licensed material in print. In electronic form, this acknowledgement must be visible at the same time as the figures/tables/illustrations or abstract, and must be hyperlinked to the journal/book's homepage. Our required acknowledgement format is in the Appendix below.

Title: Electrochemical Reduction of CO2 at Functionalized Au Electrodes

Author: Yuxin Fang, John C. Flake

Publication: Journal of the American Chemical Society

Publisher: American Chemical Society

Date: Mar 1, 2017

PERMISSION/LICENSE IS GRANTED FOR YOUR ORDER AT NO CHARGE

This type of permission/license, instead of the standard Terms & Conditions, is sent to you because no fee is being charged for your order. Please note the following:

- Permission is granted for your request in both print and electronic formats, and translations.
- If figures and/or tables were requested, they may be adapted or used in part.
- Please print this page for your records and send a copy of it to your publisher/graduate school.
- Appropriate credit for the requested material should be given as follows: "Reprinted (adapted) with permission from (COMPLETE REFERENCE CITATION). Copyright (YEAR) American Chemical Society." Insert appropriate information in place of the capitalized words.
- One-time permission is granted only for the use specified in your request. No additional uses are granted (such as derivative works or other editions). For any other uses, please submit a new request.

BACK CLOSE WINDOW

VITA

Yuxin Fang was born in Shanghai, China on April 15, 1990. She went to FuXin Senior High School in 2005, and continued on for undergraduate study in Material Science at East China University Science and Technology in 2008. Two years later, she transferred to University of Missouri in Columbia and received Bachelor of Science degrees from both institutions in Material Science and Chemical Engineering, respectively, in 2013. In August 2013, she came to the Department of Chemical Engineering of Louisiana State University in Baton Rouge to pursue Doctor of Philosophy in Chemical Engineering supervised by Professor John C. Flake.